5-2018

Objective Identification and Tracking of ZDR Columns in X-band Radar Observations

Patrick Evan Saunders
Purdue University

OBJECTIVE IDENTIFICATION AND TRACKING OF Z_{DR} COLUMNS IN X-BAND RADAR OBSERVATIONS

by

Patrick Evan Saunders

A Thesis

Submitted to the Faculty of Purdue University

In Partial Fulfillment of the Requirements for the degree of

Master of Science

Department of Earth, Atmospheric, & Planetary Sciences

West Lafayette, Indiana

May 2018

THE PURDUE UNIVERSITY GRADUATE SCHOOL
STATEMENT OF COMMITTEE APPROVAL

Dr. Robin Tanamachi, Chair

Department of Earth, Atmospheric, & Planetary Sciences

Dr. Daniel Dawson II

Department of Earth, Atmospheric, & Planetary Sciences

Dr. Michael Baldwin

Department of Earth, Atmospheric, & Planetary Sciences

Approved by:

Dr. Darryl Granger

Head of the Graduate Program

ACKNOWLEDGMENTS

This research would not be possible without the funding support of a Ross Fellowship from Purdue University, National Oceanic and Atmospheric Administration grants NA15)AR4590231 and NA16OAR4590208, and the National Science Foundation grant AGS-1741003.

I want to especially thank my primary advisor, Robin Tanamachi. She has helped guide me through my years as a graduate student and I have learned a lot about what it means to be a great scientist through her example. I also what to thank my committee members, Dan Dawson and Michael Baldwin, for their valuable input on my thesis. Their suggestions helped provide different perspectives that helped to make this research more thorough.

I am grateful to those who I have had the pleasure of working with during the course of this research. Dan Dietz provided an extraordinary amount of help with the coding aspects of this project. Members of the Argonne National Laboratory, particularly Scott Collis, helped with the implementation of Py-ART. This work would have significantly more difficult without their expertise. Members of the University of Massachusetts-Amherst Microwave Remote Sensing Laboratory (Stephen Frasier, Joe Waldinger, Will Hemerling) were responsible for the maintenance of UMass X-Pol and the data collected with UMass X-Pol during VORTEX-SE. Many people also aided in the collection of the radar data used in this research, which is very much appreciated. I also wanted to thank Kevin Knupp and Tony Lyza for pre-scouting deployment sites during VORTEX-SE. Lastly (but not least), I wanted to thank my office mates, Kevin Burress, Allison Lafleur, and Milind Sharma, for our various discussions that have helped with the progress of this work.

TABLE OF CONTENTS

LIST OF TABLES

LIST OF FIGURES

ABSTRACT

Author: Saunders, Patrick, E. MS
Institution: Purdue University
Degree Received: May 2018
Title: Objective Identification and Tracking of Z_{DR} Columns in X-band Radar Observations
Major Professor: Robin Tanamachi

With the advent of rapidly scanning radar systems, it is imperative to automate the detection of features in radar images. We discuss efforts to objectively identify Z_{DR} columns in X-band radar observations using the enhanced watershed algorithm (EWA; Lakshmanan et al. 2009), a method for identifying features in geospatial images. We discuss our choices for EWA parameters, including thresholds. The EWA is applied to Z_{DR} observations of convective storms obtained during the 2016 and 2017 VORTEX-SE field campaign by the University of Massachusetts X-band, polarimetric, mobile Doppler radar (UMass X-Pol). During several intensive observing periods (IOPs), a variety of convective storm modes, including multicellular clusters, supercells and quasi-linear convective systems, were observed. Use of the EWA facilitates fast and objective tracking of the progression and behavior of each individual Z_{DR} column, which is done using the Lakshmanan and Smith algorithm (LSA; Lakshmanan and Smith 2010).

1. INTRODUCTION

The United States is one of the more prominent locations in the world for severe thunderstorms, which cause widespread economical and societal impacts every year. From 2004 to 2013 extreme events related to severe storms (e.g. tornadoes, winds, hail, and lightning) have caused almost 2000 fatalities (http://www.nws.noaa.gov/om/hazstats.shtml) and $46 billion in estimated economic damages from severe weather-related events exceeding $1 billion (Smith and Katz 2013). Even though there have been decades of research focused on thunderstorms and the severe weather they can produce, it is still somewhat unclear precisely what dynamical and kinematical features modulate severe weather occurrences. Increasing our knowledge can lead to improved forecasts, which can reduce the number of weather-related fatalities and economic costs.

One of the defining characteristics of a thunderstorm is its updraft. Typically, a faster updraft speed (w) will result in a stronger thunderstorm, which can produce severe weather, barring other environmental characteristics. Owing to the correlation between the updraft speed and thunderstorm strength, measuring the characteristics of the updraft is important. Many instruments have been used in the past to measure the updraft speed: radiosondes (e.g. Davies-Jones 1974; Marshall et al. 1995), aircraft (e.g. Auer and Sand 1966; Lemone and Zipser 1980; Stith et al. 2002), lidar, and radar (e.g. Battan and Theiss 1966). Relative updraft strength can be inferred from satellite data as well (e.g. Rosenfield et al. 2008; Donovan and Williams 2008). Radars have the distinct advantage of obtaining three-dimensional, high temporal observations of storms. In the past though, there were only a few radar signatures that could be used to identify the location of an updraft. For example, the updraft could be identified as a bounded weak echo region (BWER, Crisholm 1973), but usually only when the updraft was strong enough to

suspend precipitation aloft. Additionally, BWER is defined as a negative region or absence of an echo, which makes it difficult to objectively identify (Lakshmanan 2000). Dual Doppler analysis could also identify regions of high vertical velocity (e.g. Brandes 1977; Kosiba and Wurman 2013), although is not usually available in real time to operational forecasters. With the implementation of polarimetric radar, the location of the updraft could be identified with a polarimetric feature called the differential reflectivity (Z_{DR}) column (e.g. Hall et al. 1984; Illingworth 1987; Bringi et al. 1991; Kumjian et al. 2014). Various characteristics of the Z_{DR} column have also been theorized in literature to be related to the strength of the updraft, hail production and possibly low-level rotation (Scharfenberg et al. 2005a; Kumjian and Ryzhkov 2008; Picca et al. 2010; Kumjian et al. 2012; 2014; Snyder et al. 2015; 2017). Z_{DR} columns can be relatively small features (sometimes with areal extent < 5 km^2) and can rapidly change in a matter of minutes (Tanamachi and Heinselman 2016). Therefore, it is important to obtain high temporal and spatial resolution observations of these features. When higher temporal resolution observations are captured, a copious amount of data will be produced, and it becomes difficult to analyze. For this reason, it is beneficial to use computer algorithms to objectively identify and track Z_{DR} columns, as well as use those tracks to analyze the characteristics and evolution of observed Z_{DR} columns. We show herein that Z_{DR} columns can be automatically identified and tracked, while also being able to extract valuable information about these Z_{DR} columns such as their areal extent, height above the 0 °C level, and peak Z_{DR} intensity.

In Chapter 2, a background of conventional weather radars is given along with a description of dual-polarimetric radar capabilities and variables. A thorough literature review of Z_{DR} columns is also given. Chapter 3 describes the computer algorithms and techniques that are used to automatically identify and track Z_{DR} columns in radar observations. Chapter 4 discusses

the VORTEX-SE field campaigns, UMass X-Pol observations during those field campaigns, and the case studies that will be analyzed. This thesis will end with a discussion of the applications and results in Chapter 5 and additional work that could be done to build upon this research in Chapter 6.

2. BACKGROUND

Conventional pulsed weather radars have been used in research and operations since the 1940s (Whiton et al. 1998), so the knowledge base on radars and their applications to weather is extensive. Given that radar is the primary instrument utilized in this research, it seems appropriate to begin with a discussion of how radars work, and the main variables used. Most of the content reviewing conventional weather radars in this chapter is based on the descriptions given in Rinehart (1997), Doviak and Zrnić (2006), and Fukao and Hamazu (2014) unless otherwise noted. Conventional weather radars have four main components: a transmitter, an antenna, a receiver and a display system. The typical configuration of a weather radar is displayed in Fig. 1. The transmitter generates a high frequency signal, which is emitted through the antenna and focused towards a specific direction by a reflector. Focusing the energy in a particular direction is what allows a radar to detect targets in space. This energy travels as an electromagnetic (EM) wave, which will be partially absorbed and scattered into all directions by its target (e.g. rain, snow, hail, etc.). After transmitting for an amount of time, usually on the order of microseconds (μs), a duplexer then switches the antenna's connection to the receiver during a significantly longer period called the "listening period". During its listening period, the antenna will receive the backscattered energy. Since the received signal is significantly weaker than what is emitted, receivers are required to detect and amplify the received signal. The signal processing and display systems can then generate a geospatial image of the observed radar variables. The most common geospatial image used is the plan position indicator (PPI), which is a map-like presentation of the radar data in radar coordinates of range and angle centered around the radar.

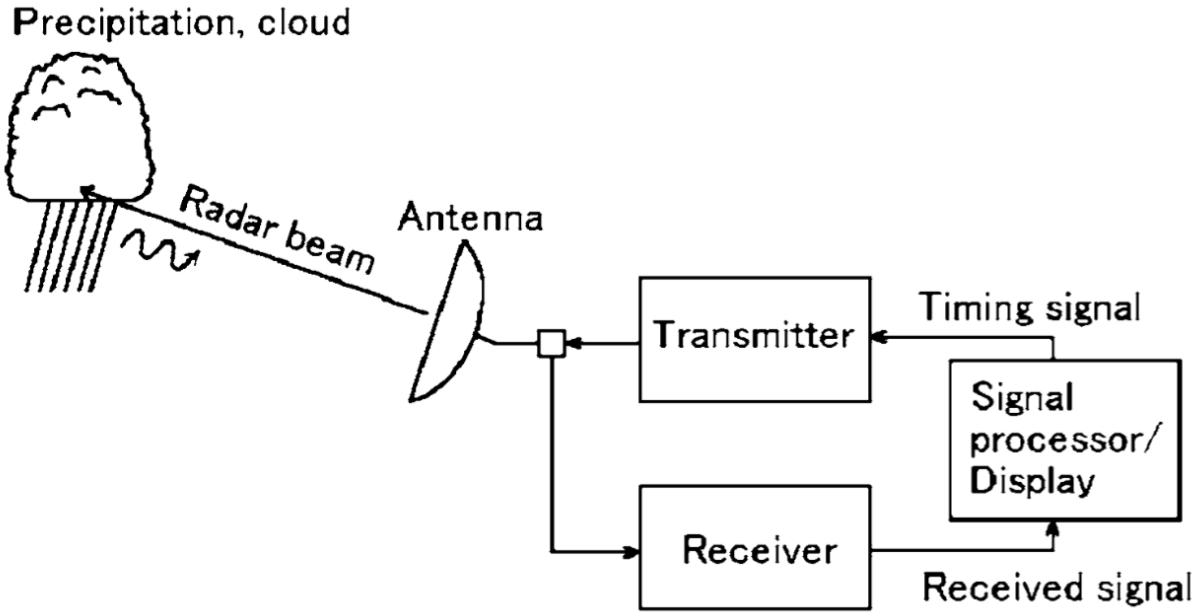

Fig. 1. This figure from Fukao and Hamazu (2014) displays some of the main components found in a pulsed weather radar.

Conventional radars, or single polarized radars, refer to radars that transmit EM waves in a single polarization. Most single polarized weather radars transmit EM waves at horizontal polarization, which means the electric field of the EM waves oscillates parallel to the Earth's surface as the waves propagate in space. Several radar products can be derived from the backscattered energy that is received by the receiver. For single polarized radars, this includes radar reflectivity factor (z), radial Doppler velocity (V_R), and spectrum width (W). Radar reflectivity factor is proportional to the amount of received power detected by the receiver, Doppler velocity is a measure of the velocity component pointed to and/or away from the radar, and the spectrum width is the variability of the Doppler velocities within a sample volume. Radar reflectivity factor (in $mm^6\,m^{-3}$) is defined by the following equation:

$$z = \int_0^\infty D^6\, N(D) dD \tag{1}$$

where N(D) is the drop size distribution, and D is the drop diameter. Equation 1 shows that *z* is heavily dependent on the number of hydrometeors in a sample volume and the sizes of those hydrometeors. Since *z* can have a huge range of values of several orders of magnitudes, it is typically expressed in a logarithmic format:

$$Z = 10 \log_{10} \frac{z}{1\ mm^6\ m^{-3}} \tag{2}$$

where *Z* can just be referred to as radar reflectivity, or reflectivity for short, and now has units of dBZ. *Z* for hydrometeors can range from 0 dBZ for cloud droplets to 70 dBZ for very large hail. *Z* is dependent on the characteristics of the radar being used, and of the hydrometeors being measured.

2.1 Polarimetric Radar

As mentioned in section 2, conventional radars only emit horizontally polarized EM waves. Polarimetric radars emit two EM waves orthogonal to each other, which can be done simultaneously or in alternating series of transmissions. Though this can be done in a variety of ways, weather radars typically employ a horizontal-vertical transmission (Fig. 2). Thus, polarimetric radars are often referred to as dual polarized in the field of meteorology. In the Rayleigh scattering regime, particles that are illuminated by a horizontally polarized EM wave become excited and scatter that energy in all directions, with some of the backscattered radiation retaining horizontal polarization. The same can be done for vertically polarized EM waves. Useful information can be obtained by comparing the backscattered EM waves received by the radar at each polarization. This gives polarimetric radars a distinct advantage over single polarized radars by providing information on size, shape, orientation, and other details of the particles being measured.

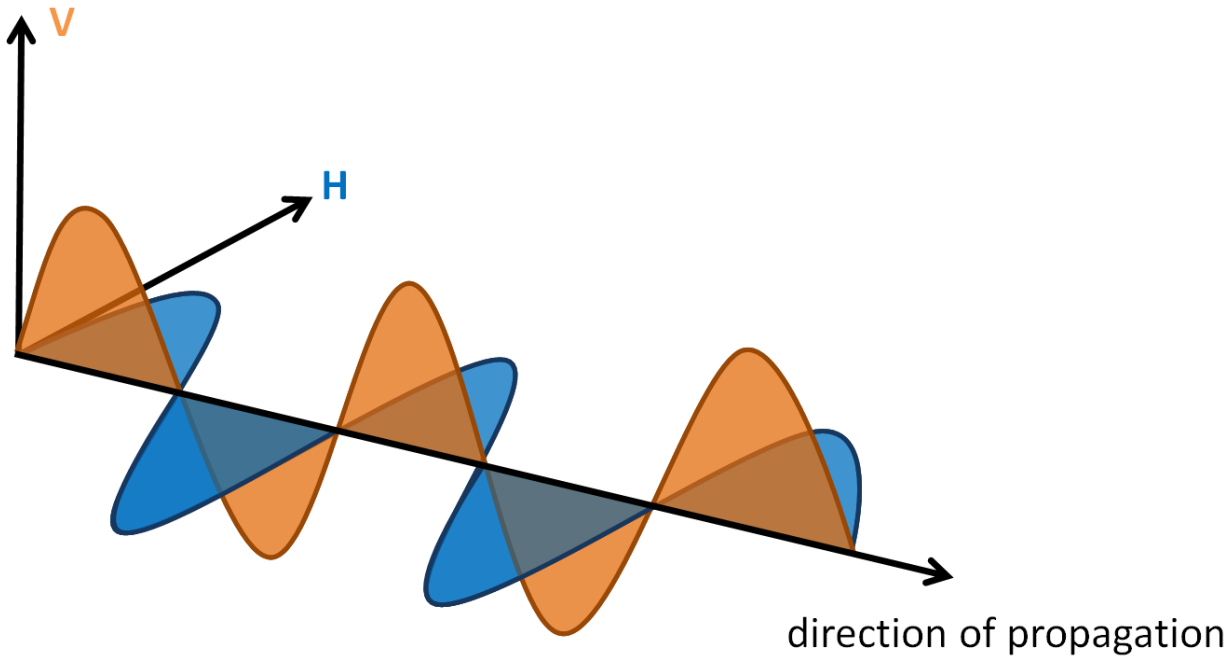

Fig. 2. This figure from Kumjian (2013a) illustrates the propagation of two linearly orthogonal electromagnetic waves.

2.2 Polarimetric Variables

As mentioned in earlier in section 2, three primary products, logarithmic radar reflectivity factor (Z), Doppler velocity (V_R), and spectrum width (W), are produced by single polarized radars but only with horizontal polarization. Polarimetric radar can measure these as well at both horizontal (H) and vertical (V) polarizations, which will hereafter be denoted as Z_H, Z_V, V_H, V_V, W_H, and W_V, respectively. In addition to these variables, a variety of new polarimetric variables can be measured by polarimetric radars. A few of these relevant variables will be introduced in this section, with discussion based on Kumjian (2013a) and Doviak and Zrnić (2006), unless otherwise noted.

2.2.1 Differential reflectivity (Z_{DR})

Since this study focuses on observations of Z_{DR} columns, which will be further discussed in section 2.3, Z_{DR} will be the primary polarimetric variable of interest. Z_{DR} was first introduced by Seliga and Bringi (1976) and is defined as:

$$Z_{DR} = 10 \log \frac{Z_H}{Z_V} \tag{3}$$

where Z_H and Z_V are the horizontal and vertical radar reflectivity factors respectively. Z_{DR} also has units of decibels (dB). Z_{DR} is the ratio between the mean horizontal and vertical backscattered powers from the hydrometeors within a sample volume, providing details on the orientation and shape of those hydrometeors. For example, a perfectly spherical particle will yield a Z_{DR} of 0 dB because Z_H equals Z_V.

Aerodynamic drag forces cause raindrops larger than 1—2 mm in diameter to deform into oblate spheroids with horizontally-aligned major axes (Pruppacher and Beard 1970). The ratio of the length of the minor (*a*) to the major (*b*) axis of the drop, which can be referred to as *a*/*b*, decreases with increasing drop diameter. Larger drops are more deformed than smaller drops (Fig. 3), with a rather linear relationship between *a*/*b* and drop size. Because of this behavior, Z_{DR} can be used to estimate the mean drop diameter in a sample volume. Since Z_{DR} is a ratio, it is not dependent on raindrop concentration, like its components, Z_H and Z_V. Thus, given a value of Z_H, there is a wide range of possible Z_{DR} values that could be observed, depending on the drop size distribution (DSD). Using Z_H and Z_{DR} together can give useful information on the concentration of raindrops and the size of those drops as well, which is important in the identification of Z_{DR} columns.

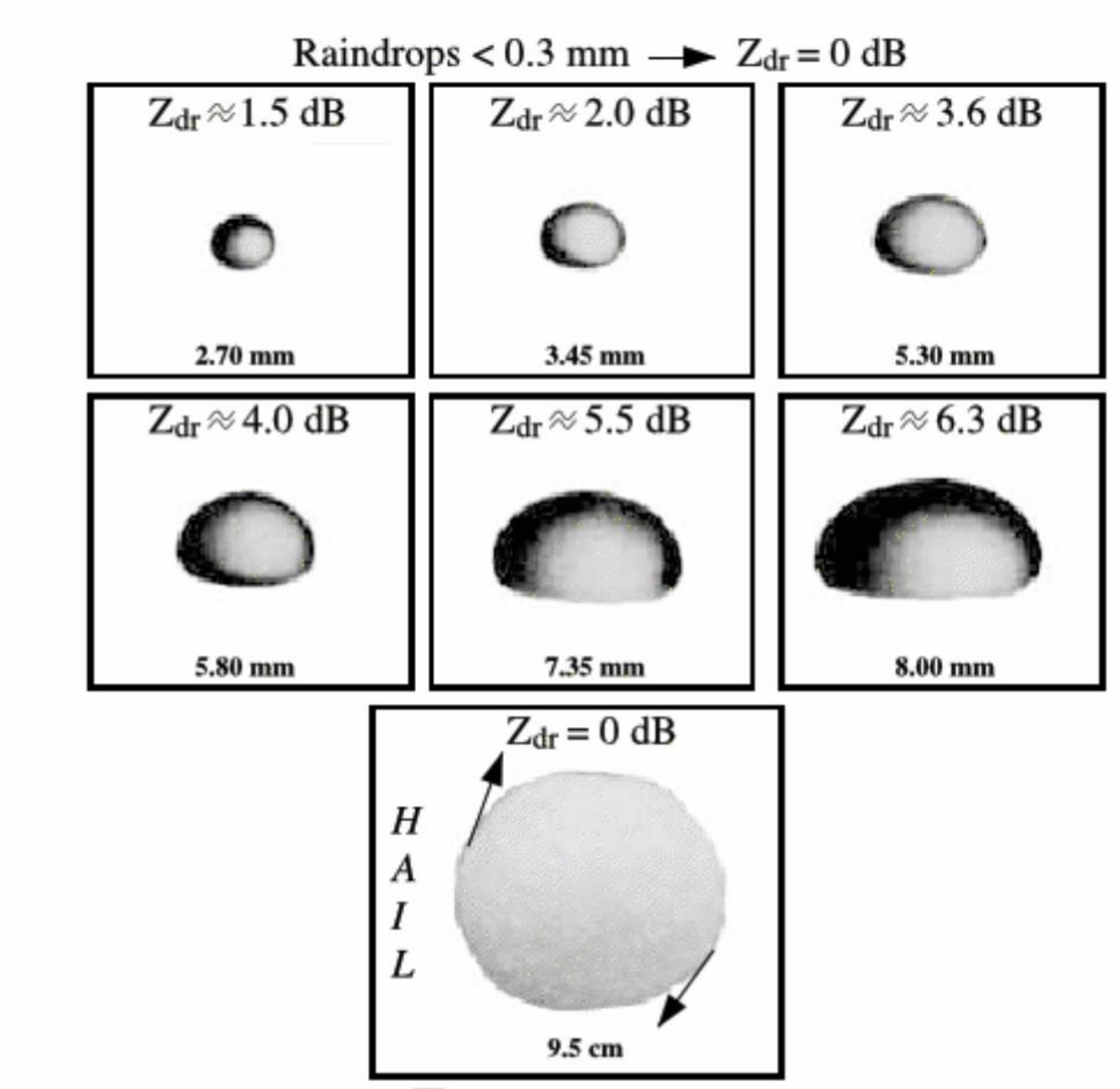

Fig. 3. This figure from Bringi and Chandrasekar (2001) shows that larger raindrops are more horizontally oblate and have larger Z_{DR} values. Hailstones have variable Z_{DR} measurements but tend to 0 dB. This is a very generalized example for the most common weather radar wavelengths (e.g. X-band, C-band, S-band).

When dealing with Z_{DR} observations of frozen precipitation, the values can be quite different, and the interpretation is not necessarily as simple. Hail can vary in shape, size, orientation, and liquid content from case to case. This results in a broad range of Z_{DR} values for hail observations. However, there have been some consistent observations. Since hail falls in a

chaotic and tumbling fashion, Z_{DR} is close to zero (e.g., Aydin et al. 1986; Bringi et al. 1986; Wakimoto and Bringi 1988). However, if hailstones are large enough they can produce negative values of Z_{DR} (e.g. Aydin et al. 1990; Balakrishnan and Zrnic 1990; Kumjian et al. 2010; Picca and Ryzhkov 2012), because of resonance scattering effects. Melting small hailstones can produce a torus of liquid water (e.g. Rasmussen et al. 1984; Rasmussen and Heymsfield 1987). This increases its Z_{DR} to values similar to rain by reducing its wobbling and creating a horizontally oblate shape.

Large aggregate snowflakes have very low density, which results in low observed Z_{DR} (Hall et al. 1984). Because of their low density, their shape is less influential on Z_{DR} than other hydrometeor types with higher densities, making their observed Z_{DR} consistently less than 0.5 dB. This makes it easy to differentiate between snow and rain, especially in elevated parts of thunderstorms, where updrafts can loft raindrops well above the freezing level.

2.2.2 Co-polar correlation coefficient (ρ_{HV})

The co-polar cross-correlation coefficient, which is referred to as ρ_{HV} or sometimes CC, was first introduced in the 1980s by Sachidananda and Zrnić (1985) and Jameson and Mueller (1985). ρ_{HV} is represented by the following equation:

$$\rho_{HV} = \frac{\langle s_{vv} s_{hh}^{*} \rangle}{\langle |s_{hh}|^2 \rangle^{1/2} \langle |s_{vv}|^2 \rangle^{1/2}} \tag{4}$$

where s_{ij} is the backscattering matrix element of a hydrometeor (McCormick and Hendry 1985) at horizontal polarization for h subscript and vertical polarization for v subscript. The brackets denote expectations of the values inside. ρ_{HV} is a measure of the similarity among the particles in a radar sample volume. A large variation of type, shape, and/or orientation in the particles being

measured will reduce ρ_{HV}. Most meteorological targets exhibit $\rho_{HV} > 0.80$ while most non-meteorological targets will have $\rho_{HV} < 0.80$.

ρ_{HV} is also especially useful for identifying nonmeteorological targets since they exhibit very low ρ_{HV} (<0.80). This is because they typically have larger variations in size, shape, and orientations as compared to precipitation, which is more uniform. Nonmeteorological targets that are often observed by weather radars include military chaff (Zrnić and Ryzhkov 2004), smoke from fires (Melnikov et al. 2008), ash from volcanoes, biological objects such as insects, birds, or bats (Zrnić and Ryzhkov 1998), sea clutter, dust, and tornado debris (Ryzhkov et al. 2005). Because ρ_{HV} is a strong discriminator between meteorological targets and non-meteorological targets, its primary use in this study is to filter out non-meteorological data. For other ways to interpret ρ_{HV} see Kumjian et al. (2013a).

2.2.3 Differential propagation phase shift (ϕ_{DP}) and specific differential phase (K_{DP})

As EM waves propagate through hydrometeors, they obtain a phase shift. Since most hydrometeors are not perfectly spherical, there will be a cumulative difference between the shifts in the horizontal and vertical polarizations. That difference is known as the differential propagation phase shift (ϕ_{DP}), where a larger phase shift in the horizontal polarization is positive and vice versa. Specific differential phase (K_{DP}) is half of the range derivative of ϕ_{DP}, which is easier to interpret since it provides a measure of the amount of differential phase shift per unit distance. Horizontally oblate particles, like raindrops, will yield positive K_{DP} values since H-polarization waves acquire more of a phase shift than the V-polarization wave.

2.3 Z_{DR} Columns

Strong updrafts can loft hydrometeors high into the atmosphere, resulting in an area of low Z_H values called the weak echo region (WER). This can create a local minimum in Z_H extending upward into and surrounded by higher Z_H, which is referred to as a bounded weak echo region (BWER; Chisholm et al. 1973) or the vault (Browning and Donaldson 1963). The air in updrafts is rising so fast that it overcomes hydrometeor terminal velocities, lofting the hydrometeors. This signature is typically only seen in the most intense updrafts, often associated with severe weather-producing thunderstorms. Thus, the formation of this signature indicates that the thunderstorm is almost certainly intensifying, and that severe weather is imminent. There have been attempts at automated BWER detection, though with limited success (Lakshmanan 2000). Because a BWER is defined as a minimum, or the absence of an echo, it is rather difficult to identify automatically. Even so, prior to polarimetric observations, this was the best way to detect updrafts with radar observations.

Vertical advection and latent heating effects perturb the 0 °C level upward inside of the updraft (Snyder et al. 2015). This allows supercooled raindrops to exist well above the environmental 0 °C level within the updraft. Additionally, raindrops do not freeze instantly upon entering an environment of freezing temperatures (e.g., Bigg 1953; Johnson and Hallett 1968; Smith et al. 1999; Kumjian et al. 2012). In fact, depending on the air temperature and drop size, it can take several minutes upon entering a subfreezing environment before raindrops completely freeze. This causes raindrops to exist above the locally perturbed freezing level. Since these raindrops have higher Z_{DR} relative to the surrounding frozen hydrometeors, they create a polarimetric signature found in observations of deep convection called the Z_{DR} column.

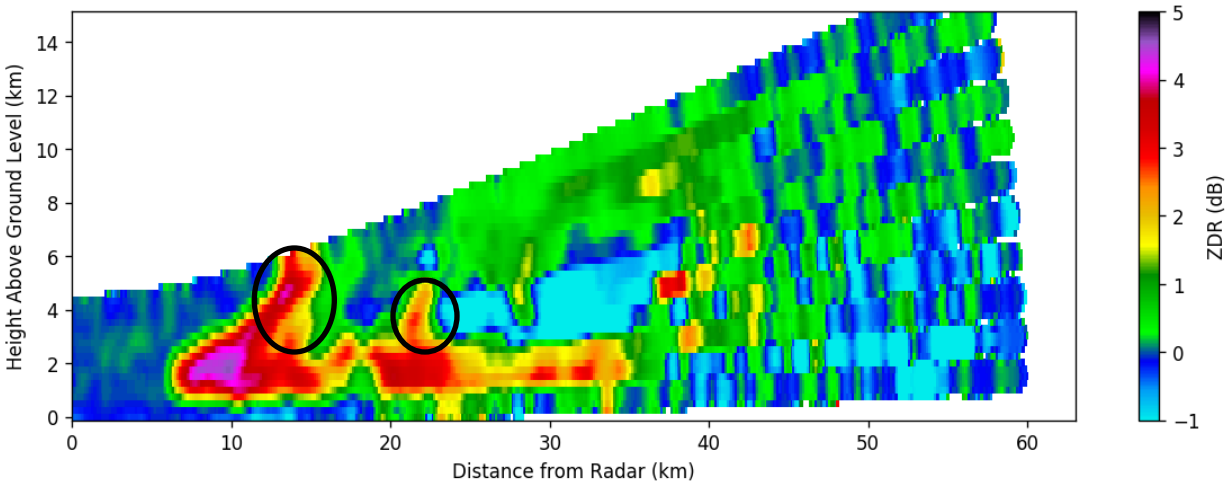

Fig. 4. A vertical cross section through two Z_{DR} columns (circled). Data collected by UMass X-Pol at 06 April 2017 0006 UTC.

The Z_{DR} column is a polarimetric radar signature consisting of a columnar region of enhanced Z_{DR} (up to 4 – 6 dB) that extends 1 – 4 km above the environmental freezing level (e.g. Fig. 4). The first observations of Z_{DR} columns were reported in the 1980s (Hall et al. 1984; Illingworth et al. 1987; Caylor and Illingworth 1987; Tuttle et al. 1989), though Z_{DR} columns were not necessarily the focus of these studies. Caylor and Illingworth (1987) first speculated that the Z_{DR} column consisted primarily of large raindrops. Aircraft measurements would later observe the presence of very large super-cooled raindrops, as well as small water-coated hailstones inside of Z_{DR} columns (e.g., Bringi et al. 1991, Brandes et al. 1995; Loney et al. 2002). These large raindrops occurred in regions of relatively low reflectivity, suggesting that that the drops existed in low concentrations. Additionally, these in situ observational studies supported the notion that Z_{DR} columns are nearly collocated with the updraft. Caylor and Illingworth (1987) and Tuttle et al. (1989) suggested that collision and coalescence could be the cause of the large raindrops in the Z_{DR} column, though this could not be confirmed. Conway and Zrnić (1993) and Höller et al. (1994) suggested that the raindrops in Z_{DR} columns originate from

a region of melting graupel and hail in the upper levels of the leading edge and are recirculated into the updraft. Bringi et al. (1991) pointed out the importance of drop size sorting in Z_{DR} columns. The terminal velocity of a liquid raindrop is proportional to its size, such that a larger drop falls faster to the ground than smaller drops. This resulted in the updraft becoming a size sorting mechanism for hydrometeors. Larger drops are suspended, while small drops are advected upward by the updraft. This causes Z_{DR} values within the Z_{DR} column to decrease with height. These earlier studies laid the foundation for understanding the microphysical processes occurring within the Z_{DR} column. Kumjian et al. (2014) further investigated the anatomy and microphysics of Z_{DR} columns by coupling a polarimetric radar forward operator with Hebrew University Cloud Model (HUCM), a 2D nonhydrostatic spectral bin microphysical model, to simulate the life cycle of the Z_{DR} column. The HUCM parameterizes the particle size distributions of a variety of hydrometeor types (e.g. liquid drops, cloud droplets, hail, graupel, snow, pristine ice crystals, others) by predicting the concentrations in discrete diameter bins. From these discrete size distributions, Z_{DR} can be calculated. The simulations were able to display the life cycle of a typical Z_{DR} column (Fig. 5) as well as the microphysical composition at each stage. In the earliest stages, small drops are developed by vapor diffusion and coalescence. These small drops would fall out of the weak updraft, extending the young Z_{DR} column downward. As the updraft strengthens and matures, large drops form rapidly and eventually fall out through the updraft, while smaller drops are advected upward. As those smaller drops are advected into the subfreezing portion of the Z_{DR} column, they begin to freeze, eventually forming mixed-phase particles towards the top of the Z_{DR} column. Z_{DR} values eventually decrease to near 0 dB when the particles freeze completely near and above the top of the Z_{DR} column. The HUCM simulations also capture the death of the Z_{DR} column. This is

caused by the descent of hailstones that have grown too large for the updraft to support. Since hailstones often have significantly reduced Z_{DR}, the Z_{DR} column will diminish as hail descends through it.

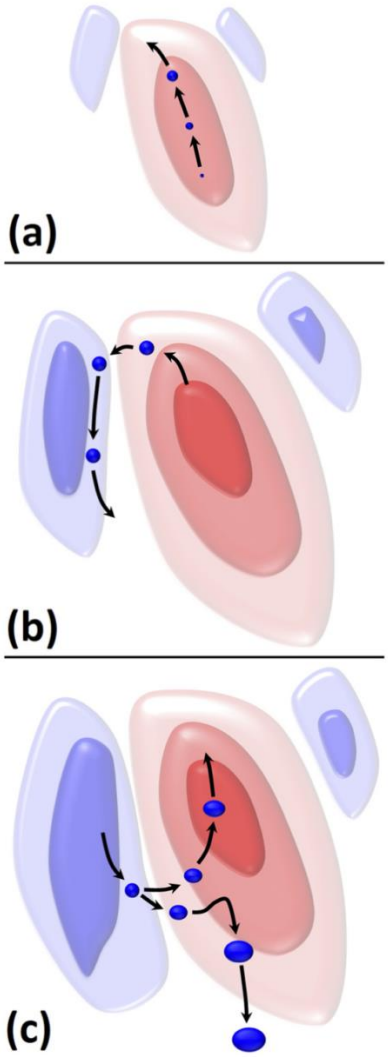

Fig. 5. This figure from Kumjian et al. (2014) illustrates the typical life cycle of a Z_{DR} column where red represents areas of updraft and blue represent areas of downdraft. The blue circular objects are raindrops and the black arrows indicate their motion.

Various characteristics of the Z_{DR} column have been theorized and observed to have correlations with updraft intensity, hail production, and/or possibly low-level rotation. The most strongly supported connection is between the updraft speed and the height of its associated Z_{DR}

column. In early studies, a correlation was observed between Z_{DR} column height and updraft intensity (e.g. Tuttle et al. 1989; Bringi et al. 1991; Bringi 1997). Positive correlation between Z_{DR} column height and updraft intensity was also found in recent modeling studies (Kumjian et al. 2012; Kumjian et al. 2014; Snyder et al. 2015; Snyder et al. 2017).

Z_{DR} columns have the potential to have other forecasting applications. Scharfenberg et al. (2005a) discusses some of the practical applications of Z_{DR} columns in operational forecasting. On 10 May 2003, early model guidance and observations indicated that significant severe weather would develop later that afternoon in Central Oklahoma, with the possibility of long-tracked tornadoes. With this in mind, forecasters might issue warnings earlier at lower criteria because of this expectation. However, as the event progressed, forecasters noticed that the Z_{DR} columns were not as intense as what is expected from an extreme event. Because of this, forecasters were able to change their forecast philosophy to one more representative of a lower-end severe weather event. Picca et al. (2010) demonstrated that increases in Z_{DR} column height and/or areal extent are positively correlated with increases in low-level Z_H at 10—30-minute lag times. This correlation with surface Z_H, as well as surface hail mass content, is also seen in the Kumjian et al. (2014) microphysical modeling study, with maximum correlation coefficient of ~.80 at a time lag of 13—15 minutes. Van Den Broeke (2017) looked at a number of polarimetric signatures, including the Z_{DR} column, in WSR-88D observations and analyzed the variability of those polarimetric signatures over a tornado's life cycles and intensity in supercells. There was no significant difference between Z_{DR} column metrics during tornado and nontornado times, meaning that Z_{DR} columns observed in WSR-88D observations could not be used to discriminate between tornadic and nontornadic supercells. However, there generally was an increase in Z_{DR} column areal extent and height in storms with stronger tornadoes (EF-3+).

Though there have been many observations of Z_{DR} columns over the past several decades (e.g., Meischner et al. 1991; Herzegh and Jameson 1992; Conway and Zrnić 1993; Höller et al. 1994; Jameson et al. 1996; Bringi et al. 1996, 1997; Hubbert et al. 1998; Smith et al. 1999; Kennedy et al. 2001; Scharfenberg et al. 2005a; Kumjian and Ryzhkov 2008, Romine et al. 2008, Payne et al. 2010; Kumjian et al. 2010; Rowe et al. 2011; Tanamachi et al. 2012; Snyder et al. 2013; Houser et al. 2015; Van den Broeke and Van Den Broeke 2015; Homeyer and Kumjian 2015; Tanamachi and Heinselman 2016; among others), many of these studies are limited by coarse temporal/geospatial resolution, poor data quality, and sparse volume coverage patterns. Since the evolution of Z_{DR} columns and associated severe weather phenomena occur on short time scales, high temporal resolution observations are desired, especially in the mid-levels (4—8 km AGL). Coarse vertical resolution from commonly used volume coverage patterns, coupled with beam spread can degrade the analysis of Z_{DR} column height (Picca et al. 2015). Increasing the number and frequency of scans in the mid-levels would greatly increase the quality of Z_{DR} column height analysis. Additionally, since Z_{DR} is especially noisy (Scharfenberg et al. 2015b; Tanamachi and Heinselman 2016), increasing the number of radar pulses used to calculate the Z_H and Z_V moments would greatly improve Z_{DR} data quality and increase confidence in Z_{DR} column identification (Tanamachi and Heinselman 2016).

3. METHODOLOGY

3.1 Description of Z_{DR} Column Identification Algorithm

To analyze the evolution of Z_{DR} columns, it is necessary to obtain more rapid radar observations than what is currently implemented by the Next Generation Weather Radar (NEXRAD) system, especially at the midlevels (3—8 km) in convective storms. With higher temporal resolution data, it becomes more difficult to quickly and subjectively analyze data. For this reason, it is beneficial to create computer algorithms that can objectively identify signatures in radar data. Snyder et al. (2015), hereafter S15, used an algorithm that calculates the depth of Z_{DR} columns in radar data. In their algorithm, filtered Z_{DR} is mapped to a three-dimensional latitude-longitude-height grid. At each horizontal grid point, the number of vertically consecutive grid points with $Z_{DR} \geq 1$ dB above the 0 °C level is counted to determine the vertical depth of the Z_{DR} column. The 0 °C level is provided by 13 km Rapid Refresh (RAP; Brown et al. 2011) analyses. A similar Z_{DR} column detection technique to what is devised in S15 is also used by Starzec et al. (2017) in combination with K_{DP} columns and BWER for updraft detection, and by Carlin et al. (2017) for assimilation of Z_{DR} columns into storm-scale models.

The technique described in S15 is a calculation of the depth of enhanced Z_{DR} at each grid point rather than an actual Z_{DR} column identification algorithm. It was shown that this technique does provide meteorologists with an efficient way to evaluate updraft strength in an operational setting. The identification technique that we present here is performed a little differently. Instead, we used an object-oriented mindset, which involves the objective identification of Z_{DR} column objects. This has the added benefit of allowing the user to objectively calculate Z_{DR} column

characteristics such as height, areal extent and peak value, while also having the ability to track them across time.

Table 1. Specifications of the gridded radar data.

Minimum Height	0 °C level + 500m
Maximum Height	8.5 km
Horizontal resolution	250 m
Vertical resolution	250 m
Horizontal dimension	63 km x 63 km
Radius of Influence	750 m

As in S15, radar data is mapped to a three-dimensional Cartesian grid. This was done using Py-ART (Helmus and Collis 2016), a Python package designed for those working with radar data. The specifications of this grid are given in Table 1. The map_gates_to_grid function in Py-ART is used, with a Cressman weighting function and a constant radius of influence (ROI). The ROI needs to be chosen so that it is larger than at least half of the vertical spacing at the radar's maximum unambiguous range. This removes any vertical discontinuities that would appear with a smaller ROI. Vertical spacing of the radar data is dependent on the number of scans are done in a volume coverage pattern and the range from the radar. This is because the vertical spacing tends to increase with increasing distance from the radar, which is illustrated in Fig. 6.

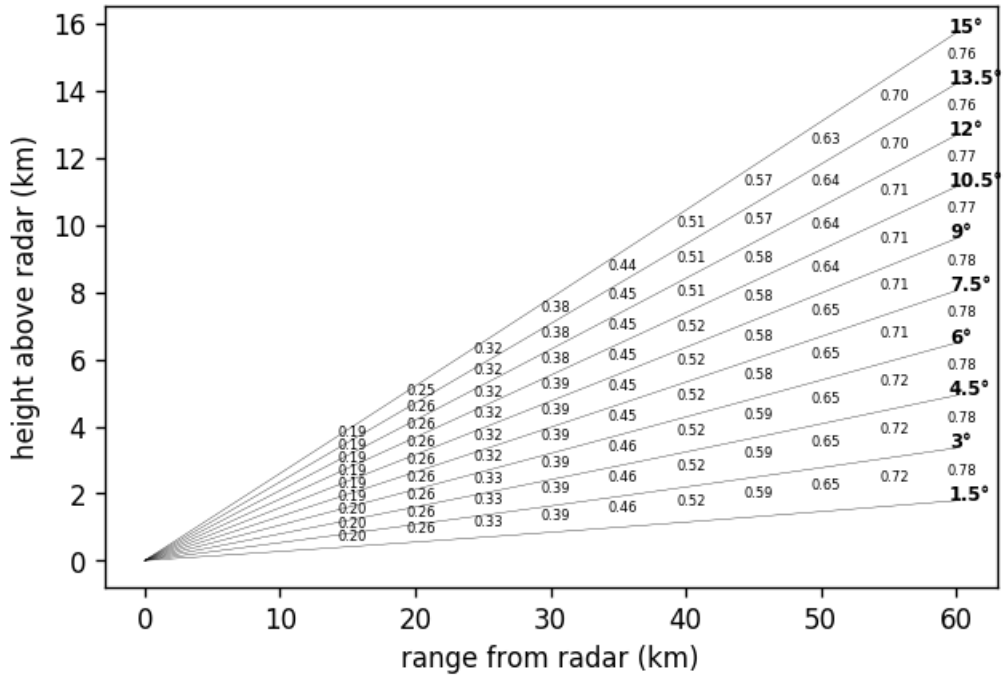

Fig. 6. An example volume coverage pattern, where the solid lines represent the center of each radar beam, the bold numbers represent the elevation of each radar beam, and the unbold numbers are half of the vertical spacing between the radar beams.

The algorithm that we use to objectively identify columns is the enhanced watershed algorithm (EWA; Lakshmanan et al. 2009). For the cases evaluated in this study, which will be discussed in chapter 4, the EWA is applied to a horizontal level 500 m above the 0 °C level, which is taken from the nearest sounding. We chose a level slightly above the 0 °C level to account for errors and local variations in the 0 °C level.

The idea of the EWA comes from the concept of water flowing into a drainage basin, or watershed (hence the name enhanced *watershed* algorithm), and filling that drainage basin starting from minima and gradually rising. This idea can be applied to a horizontally two-dimensional field of a single variable, which in this study is Z_{DR}. Since Z_{DR} columns are areas of enhanced values, the flooding starts at a maximum rather than a minimum, and gradually filling the surface of Z_{DR} at progressively lower values. The flooding proceeds on a pixel-by-pixel basis

based on the value of the neighboring pixel. The flooding level is slowly decreased so that flooding can start from progressively lower maxima. Various thresholds are used to determine when the flooding stops, and which objects are kept. The exact details on how the EWA is implemented are elaborated on in the following paragraphs.

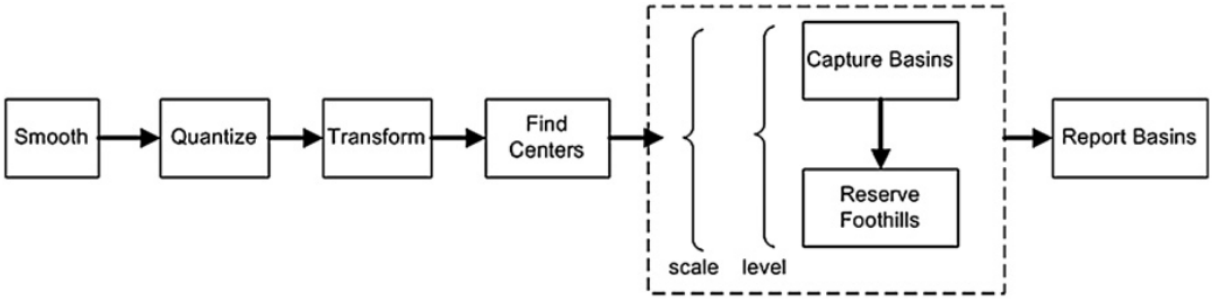

Fig. 7. The stages of the EWA, from Lakshmanan et al. (2009).

The stages of the EWA are shown in Fig. 7, which is implemented using the Python programming language. First, the image is smoothed using a Gaussian filter with $\sigma = 1$ (e.g. Fig. 8b). Smoothing helps to remove spurious maxima with extreme depths, which can change the definition of a basin as shown in Fig. 9. Smoothing also reduces the number of centers that the algorithm iterates through, increasing the efficiency of the algorithm. Smoothing should be done so that the algorithm maintains basins of expected sizes. Since Z_{DR} columns can be a relatively small feature (<10 km^2 areal extent) it is possible that a more aggressive smoothing technique can filter out small Z_{DR} columns.

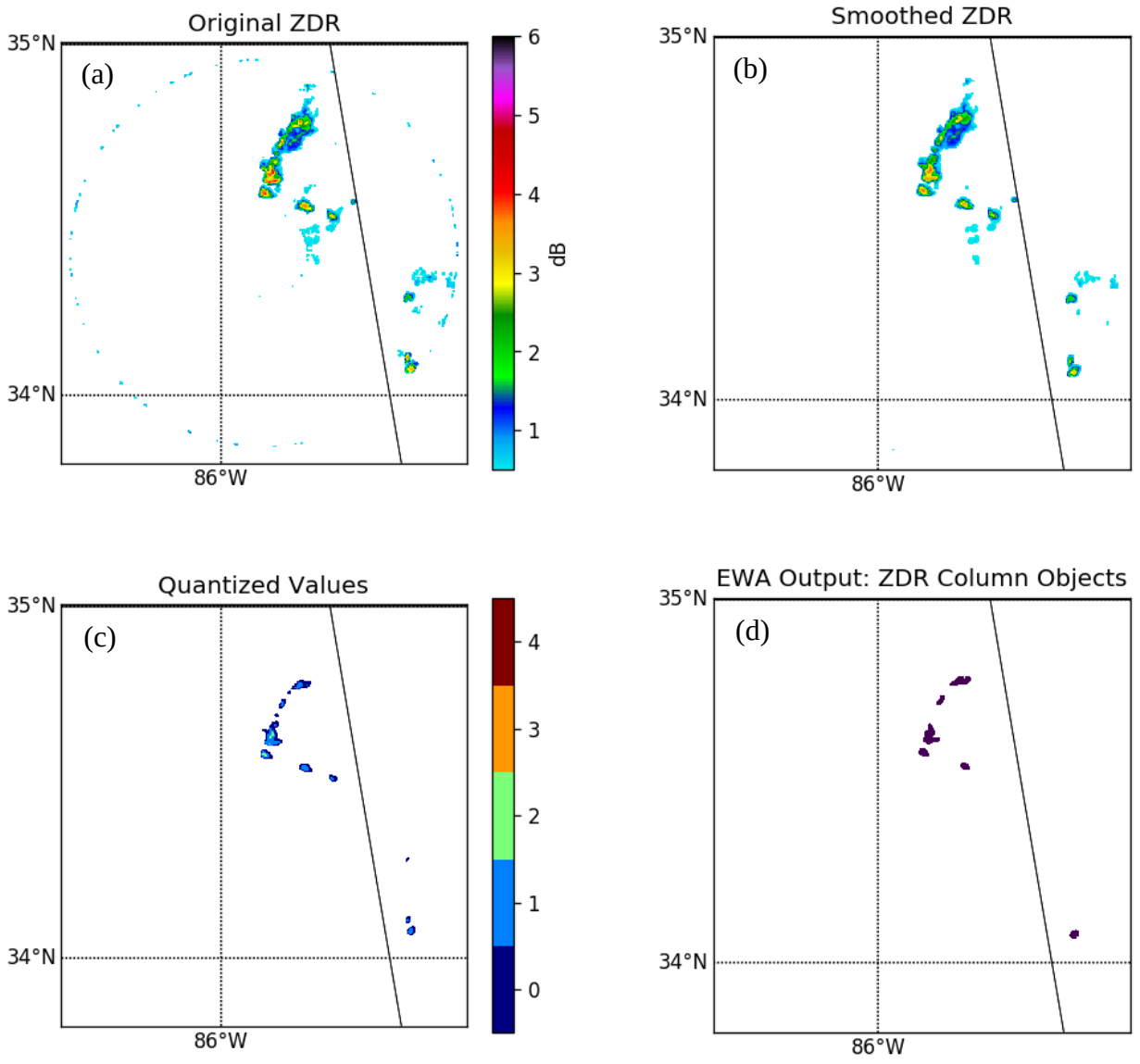

Fig. 8. An example of the implementation of the EWA on Z_{DR} data from UMass X-Pol observations on 05 April 2017. A CAPPI of (a) the original Z_{DR}, (b) smoothed Z_{DR} with a Gaussian filter, (c) quantized Z_{DR} values using a=2 dB, b=7 dB, and δ=1, and (d) identified Z_{DR} column objects using a saliency of 3 km^2.

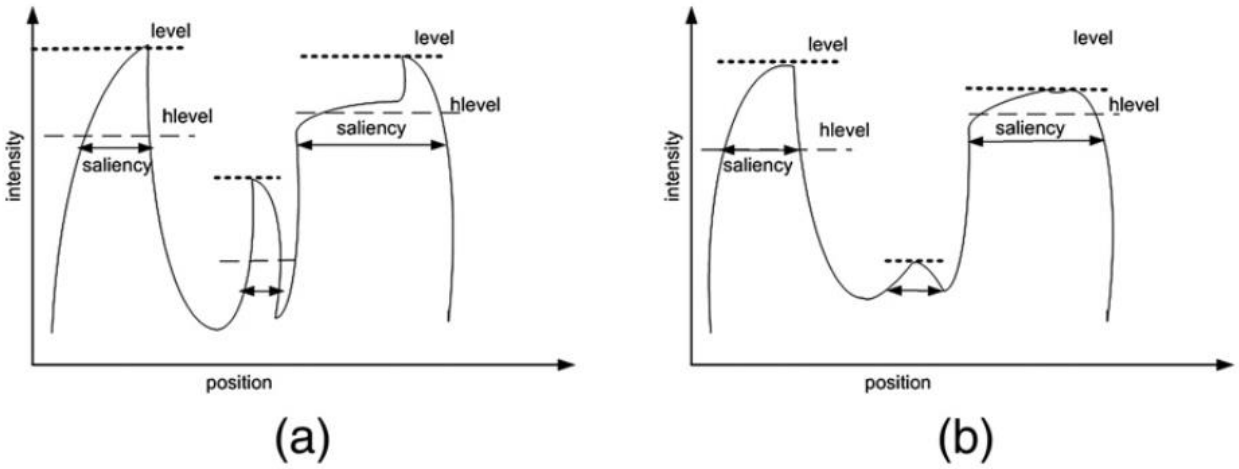

Fig. 9. (a) Narrow peaks can prevent Z_{DR} column objects from being identified. (b) Smoothing removes these spurious peaks, making them cleaner.

The next step is to quantize the data (e.g. Fig. 8c). Image values are linearly scaled using:

$$Q_{x,y} = \text{round}\left(\frac{Z_{DR\,(x,y)} - a}{\delta}\right) \tag{5}$$

where $Q_{x,y}$ is the final quantized value, $Z_{DR\,(x,y)}$ is the intensity value of Z_{DR}, a is the lower bound on the intensity, and δ is a variable that is typically used to reduce the dynamic range in data with spatial resolution too coarse to be smoothed. The round function is used to round each value in equation (5) to the nearest integer. The process for deciding the various adjustable variables used in this section, including a and δ, will be discussed in Chapter 5. To limit the size of the data structure, upper and lower bounds are put on the data structure:

$$\left.\begin{array}{rl} \text{When } Z_{DR\,(x,y)} \le a, & Q_{x,y} = 0 \\ \text{When } a < Z_{DR\,(x,y)} \le b, & Q_{x,y} = \text{round}\left(\dfrac{Z_{DR\,(x,y)} - a}{\delta}\right) \\ \text{When } Z_{DR\,(x,y)} > b, & Q_{x,y} = \text{round}\left(\dfrac{b-a}{\delta}\right) \end{array}\right\} \tag{6}$$

where b is an upper bound on the data. Equation (6) is showing that all values below the lower bound are converted to zero (first line) and all values above the upper bound are capped at the same value (third line). Other values in between each bound are rounded to the nearest integer

(second line). The $Q_{x,y}$ array is then transformed into a data structure that is organized by each pixel's intensity. For example, all pixels (i.e. that pixel's *x*, *y* location) with a value of 2 dB will be put into a list, all pixels with a value of 3 dB into a separate list, etc. The rest of the EWA iterates through this data structure instead, though the quantized image is still used for capturing the basin. Next, candidate Z_{DR} column centers are determined by iterating through this data structure in reverse order of intensity and removing from the list neighbors of those pixels that are candidate centers. Once this is completed, the immersion process is performed by iterating through the list of centers and flooding the area, starting at each center. This is the process used to identify Z_{DR} column objects. Output of the EWA is a labeled imaged, where the values indicate the Z_{DR} column object that each pixel belongs to (e.g. Fig. 8d). Pixels that are not a part of a Z_{DR} column object are assigned a value of -1 (e.g. pixels below *a*). Pseudocode for this process is provided in Procedure 2 and Procedure 3 in Lakshmanan et al. (2009). A threshold called "saliency" is used to determine if Z_{DR} column objects are retained. Saliency is a criterion defined based on the areal extent of the Z_{DR} column object. If the area of the Z_{DR} column object is below the saliency (too small) then the values of those pixels are reverted to -1. Since Z_{DR} columns can be small in areal extent (Tanamachi and Heinselman 2015; Van Den Broeke 2016), a small saliency is used. The process that is used to determine what saliency is used is described in Chapter 5. For each Z_{DR} column object, the EWA immersion process continues until it reaches the intensity value at which it becomes salient (reaches the saliency check).

The saliency check is used to determine the desired scale of identified Z_{DR} column objects. Increasing the saliency will result in smaller Z_{DR} column objects not being identified while reducing the saliency could result in the identification of spurious Z_{DR} column objects. Changing the *a* can also impact how the EWA identifies objects. Decreasing *a* allows smaller

storms to combine and create larger objects, especially when there are intermediate intensities between small columns. These values are completely dependent on the desired scale of identified Z_{DR} column objects. This is especially a challenge in identifying Z_{DR} columns because different storm modes produce different Z_{DR} column shapes and sizes. The decision-making for parameter selection for our dataset is further discussed in Chapter 5. For additional detail regarding the EWA, see Lakshmanan et al. (2009) and Lakshmanan (2012).

3.2 Description of Z_{DR} Column Tracking Algorithm

The EWA produces Z_{DR} column objects from UMass X-Pol radar observations but does not provide any information relating them across time. For this reason, a tracking algorithm must be used to associate Z_{DR} column objects in time. The tracking algorithm described in Lakshmanan and Smith (2010) is used in this study and the algorithm is hereafter referred to as the Lakshmanan and Smith algorithm (LSA). All Z_{DR} column objects produced by the EWA for a given case are used by the LSA. The LSA begins by projecting Z_{DR} column objects identified at t_n to their expected locations at t_{n+1} (e.g. Fig. 10a). This is done by taking the average vector of the storm track containing the Z_{DR} column object. If the Z_{DR} column object is not a part of an established track, the Bunkers et al (2000) storm motion, estimated from a nearby NWS sounding, is used to project the Z_{DR} column object from t_n to t_{n+1}. Storm cells identified at t_n are also sorted by track length so that longer-lived Z_{DR} column objects are given priority in the object matching process. Next, for each unassociated projected Z_{DR} column object, all centroids within the search radius (defined as $\sqrt{A/\pi}, A = area$) at t_{n+1} are identified (e.g. Fig. 10b). Lakshmanan and Smith (2010) mention that this search radius can be changed to the user's preference. If there is only one centroid within the search radius, the two Z_{DR} column objects are

associated with each other and a track is drawn between them (e.g. Fig. 10c). These steps are performed for all unassociated projected centroids. For the remaining unassociated centroids at t_{n+1}, a cost function is defined:

$$c_{i,j} = (x_i - x_j)^2 + (y_i - y_j)^2 + \frac{A_j}{\pi}\left(\frac{|A_i - A_j|}{A_i \wedge A_j} + \frac{|d_i - d_j|}{d_i \wedge d_j}\right) \quad (7)$$

where x_i, y_i are the location coordinates, A_i is the area, d_i is the maximum pixel value within the cell, $|a|$ is the magnitude of a, and $a \wedge b$ is the maximum of a and b. For each unassociated centroid at t_{n+1}, all projected centroids within the search radius are identified (e.g. Fig. 11). Of those projected centroids, the projected centroid with the lowest calculated cost function ($c_{i,j}$) is matched to the unassociated centroid. Centroids at t_{n+1} that have no projected centroids within the search radius are defined as a new Z_{DR} column object.

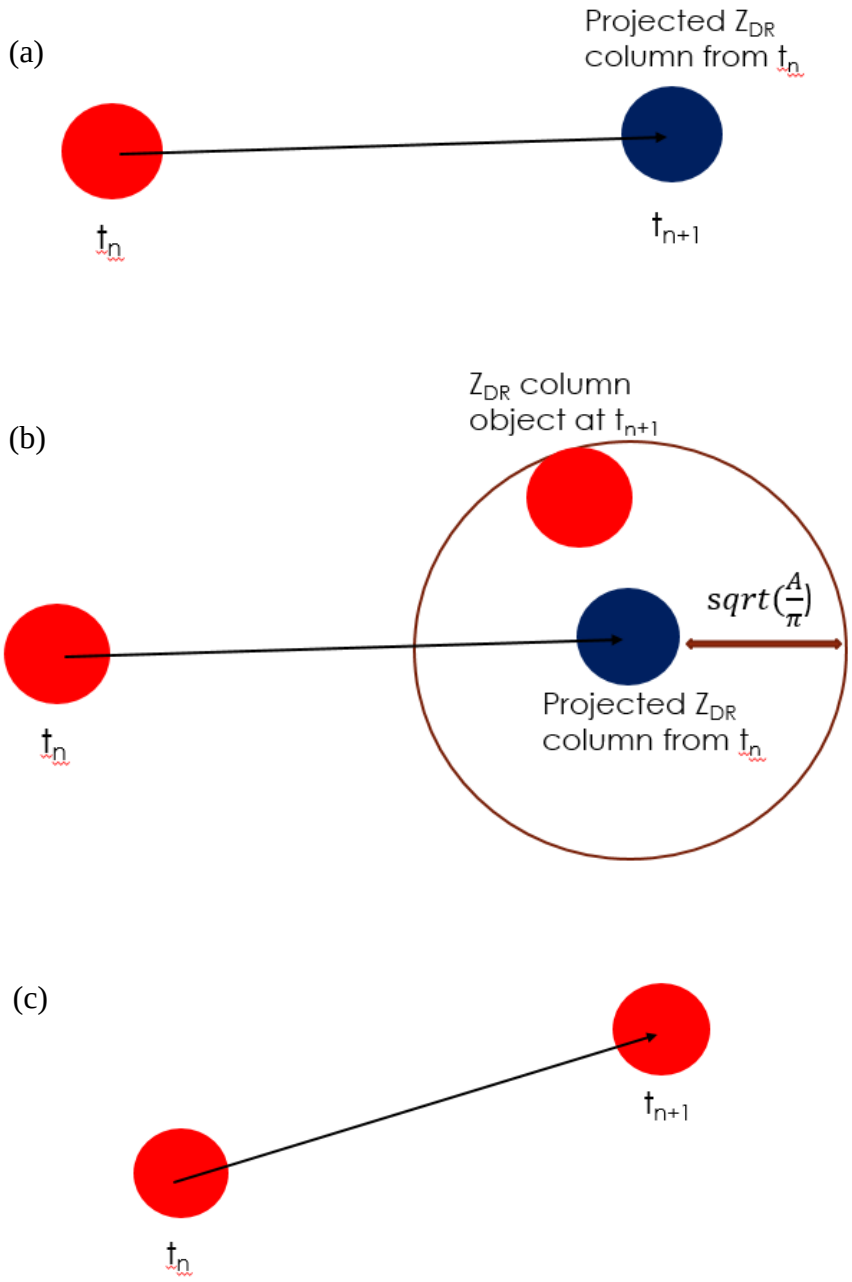

Fig. 10. An example to illustrate how the LSA is implemented. In general, Z_{DR} column objects are represented by red circled and projected Z_{DR} columns by blue circles. (a) Z_{DR} column object at t_n is projected forward by the LSA to the next time interval t_{n+1}. (b) Z_{DR} column objects at t_{n+1} within the search radius are identified. (c) If there is only one Z_{DR} column object within the search radius, then the two objects are associated.

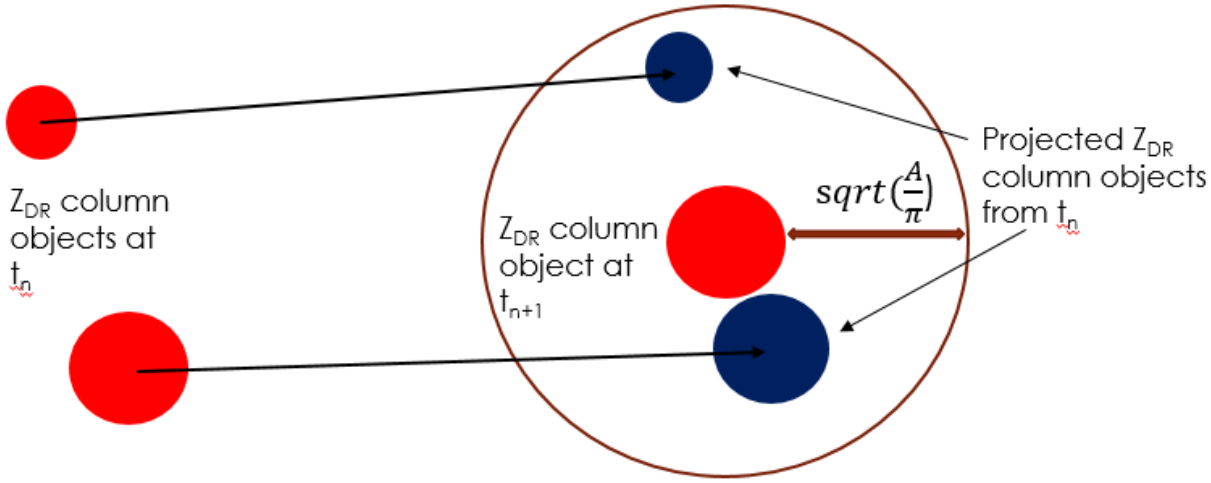

Fig. 11. A continuation of Fig. 10. For all unassociated Z_{DR} column objects tn+1, the same search radius is used to identify projected Z_{DR} columns. The cost function in equation (7) is used to determine which projected Z_{DR} column is matched. In this case, the bottom projected Z_{DR} column would be matched (assuming constant peak value among all presents objects) because it is separated by a smaller distance and is similar in size.

The LSA is a partial combination of the tracking algorithms developed in Johnson et al. (1998), Dixon and Wiener (1993), Lakshmanan et al. (2009), and Han et al. (2009) with some small unique additions. Traditional methods of track evaluation used a single skill score (e.g. percent correct) to evaluate tracks. However, this method is very vague and makes it difficult to adjust parameters in tracking algorithms. Lakshmanan et al. (2010) discusses a way to evaluate tracks and tracking algorithms. Instead of using a single skill score to evaluate tracking algorithms, three criteria are evaluated: duration of tracks, number of mismatches and number of jumps. The duration of a track is used to evaluate the number of dropped associations in a given track (Fig. 12a, b). An increase in dropped association will lead to shorter tracks, which is undesirable. Other undesirable track qualities include mismatches (Fig. 12c) and jumps (Fig. 12d), which do not decrease track durations but are incorrect associations. This new technique

was used to compare the LSA and five other tracking algorithms, using four cases that included isolated cells, a squall line, a mini-supercell, stratiform precipitation, and a mesoscale convective system (MCS). The LSA had good-to-moderate performance for every metric in each case, something that could not be said for the other tracking algorithms that were being evaluated. The LSA's consistency in a variety of convective modes and for all metrics is important since the LSA is applied to many different situations. The case studies that we applied these algorithms to will be discussed in Chapter 4.

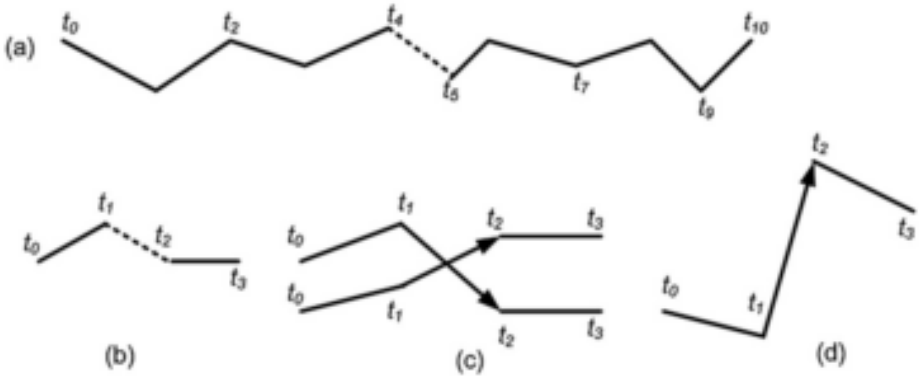

Fig. 12. (a) and (b) are indicative of dropped association as marked by the dashed lines. (c) depicts a mismatch and (d) illustrates a jump. This image is from Fig. 1 in Lakshmanan and Smith (2010).

One important aspect of this research is to show that valuable information can be retrieved from tracks of Z_{DR} columns. By calculating various characteristics, such as height above the 0 °C level, areal extent and maximum intensity, of all identified Z_{DR} column objects and then relating them across time with tracks, we can observe the evolution of each Z_{DR} column characteristics. Areal extent and maximum intensity are calculated at 500 m above the 0 °C level, which is the level at which the EWA is applied to. Maximum intensity is calculated using the values from the EWA, meaning that each value is rounded to the nearest integer. The depth that each Z_{DR} column object extends above the 0 °C level is calculated individually and after all Z_{DR}

column objects are identified. This is done by taking the collection of pixels located at in its respective Z_{DR} column object and is analyzed in increasing vertical increments of 250 m. The number of pixels (and thus the area) that exceed 1 dB is recorded. The height at which this area first decreases below 1 km^2 is recorded as the Z_{DR} column height above the 0 °C level.

3.3 Z_{DR} Artifacts and Artifact Mitigation

S15 discusses some challenges of automated Z_{DR} column detection, which are relevant to the identification algorithm that is used in this research. First, there are other processes that can create enhanced regions of Z_{DR} in convective storms above the freezing level, which would increase the number of false Z_{DR} column detections. The three-body scatter signature (TBSS; Zrnić 1987; Hubbert and Bringi 2000) is a radar signature that is described as low, radially decreasing Z_H, high Z_{DR} (in higher elevations) and low ρ_{HV} down radial of hail cores. Transmitted energy from a radar is scattered by hailstones to the ground, then scattered back to the hydrometeors, then again partially scattered back to the radar. Hubbert and Bringi (2000) showed with model simulations that TBSS enhances Z_{DR} radially at high elevations (>3km AGL), which is typically where Z_{DR} columns are observed. The Z_{DR} enhancement does decrease monotonically down-radial, similar to that Z_H. TBSS are not uncommon artifacts, especially in strong convective storms where large hail is present aloft. A simple attempt was made to remove TBSS signatures. This was done by masking out radar gates where $Z_{DR} > 1$ dB and $\rho_{HV} < 0.8$, since ρ_{HV} is relatively lower in TBSS than what is typically observed in observations of hydrometeors. Masking out all radar data where $\rho_{HV} < 0.8$ altered the data too much when mapping to a Cartesian grid, so data were only removed where $Z_{DR} > 1$ dB to minimize false identifications.

Other radial streaks of enhanced Z_{DR} can appear in the ice regions of convective storms if the polarimetric radar simultaneously transmits and receives horizontally and vertically polarized waves (STSR) as UMass X-Pol does. This artifact is caused by cross-coupling between orthogonally polarized waves, which is caused by depolarization from canted ice crystals, which are usually aligned due to a strong electrostatic field (Ryzhkov and Zrnić 2007). Because the author, after subjective examination, did not identify any instances of this artifact that affected the outcome, no effort was made to remove this artifact in the UMass X-Pol VORTEX-SE dataset.

3.4 Limitations

This study has limitations related to the collection of radar data. Vertical resolution of radar data can be very coarse, depending on the volume coverage pattern and the range from the radar. Not only does beam spread increase with range, but vertical spacing between beams also increases as well (e.g. Fig. 6). This means that it can be difficult to capture shallower Z_{DR} columns that are far away from the radar and calculations of Z_{DR} column height will have larger errors at greater distances. This can be mitigated by adding additional elevation scans in the midlevels but at the expense a longer volume update time.

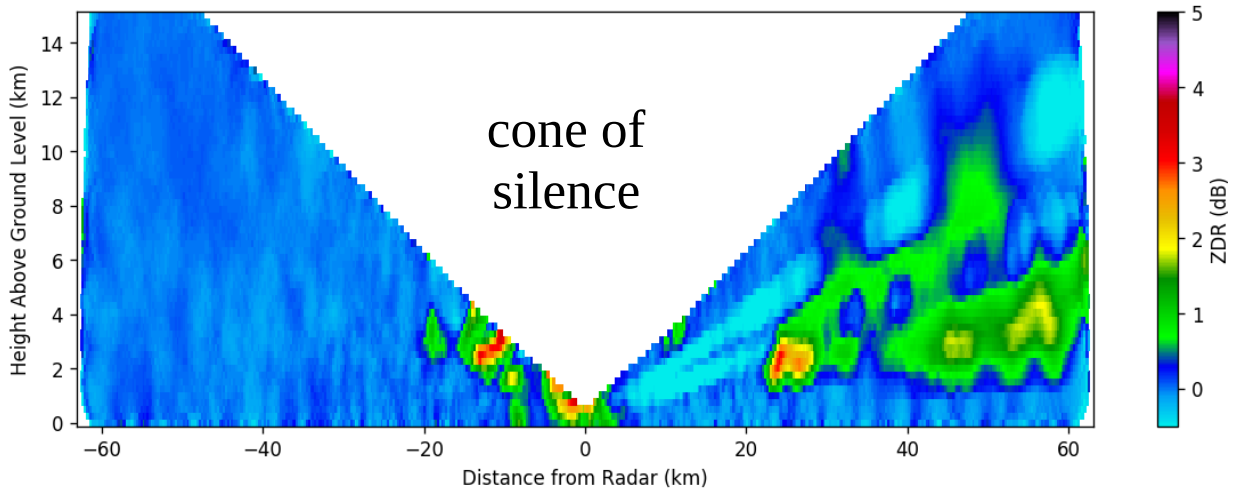

Fig. 13. An example of a cross section through a volume of data mapped to a Cartesian grid. Radar data from UMass X-Pol on 05 April 2017 in northeastern Alabama.

The cone of silence can be problematic, especially since Z_{DR} columns are a mid-level signature. The cone of silence is defined as an inverted, cone-shaped area that is not observed by the radar, as illustrated in Fig. 4 and Fig. 13. In Fig. 13, the maximum elevation is 15°. Having a higher (lower) elevation angle would decrease (increase) the extent of the cone of silence. Depending on the 0 °C level, Z_{DR} columns have to be a certain distance away from the radar before even being detected. In Fig. 13, for a 0 °C level of 4 km, Z_{DR} columns would have to be at least 15 km away from the radar to be detected. The cone of silence can also introduce discontinuity in tracks if Z_{DR} columns move through it. This can result in significantly shorter tracks and makes it harder to evaluate the tracking algorithm. Additionally, the full extent may not be observed due to the cone of silence capping the Z_{DR} column. For example, in Fig. 13, the Z_{DR} column at approximately -18 km from the radar is capped off at about 4.5 km AGL.

If storms are moving quickly, a vertical tilt can be introduced into the Z_{DR} columns owing to storm movement during data collection (Snyder et al. 2015). Since the height of the Z_{DR} column is calculated by observing the pixels directly above where the EWA identifies Z_{DR}

column objects, a vertical tilt in the data can be problematic in the calculation of Z_{DR} column height. The amount of vertical tilt introduced is dependent on the storm propagation speed, the scan rate of the radar and the number of elevation angles that sample the Z_{DR} column. If a Z_{DR} column is sampled by four elevation angles and is being observed by a radar with a scan rate of $24^{o}s^{-1}$, it would take 60 seconds for four full 360º PPIs. This means that with a typical storm motion of $15ms^{-1}$, the Z_{DR} column would have propagated 900 m during this time. Though, this is a nontrivial amount, it is not corrected for in this study.

4. DATA COLLECTION

4.1 Verification of the Origins of Rotation in Tornadoes Experiment-Southeast (VORTEX-SE) Overview

The Verification of the Origins of Rotation in Tornadoes EXperiment (VORTEX) are a series of field projects that are focused on the study of tornadogenesis. VORTEX1 (1994—95; Rasmussen et al. 1994) was the first of these projects with some smaller spinoff projects in 1997—98 (SUB-VORTEX) and 1999 (VORTEX-99). These led to one of the largest tornado studies ever in VORTEX2 (2009—2010; Wurman et al. 2012). The current VORTEX project is VORTEX-Southeast (VORTEX-SE; Rasmussen et al. 2015; Laws et al. 2018), which is a project focused on studying processes related to tornadogenesis specific to the Southeast United States. Since observations used in this research were collected during the 2016—17 VORTEX-SE field campaigns, a general overview of the experiment and its intensive observation periods (IOPs), including forecasting, and observation activities are given in this section.

VORTEX-SE is a research project mandated by Congress to understand how environmental and geographical characteristics of the southeastern United States affect various characteristics of tornadoes that occur in this region. The southeast United States experiences a disproportionate number of killer tornadoes (Ashley 2007). This is hypothesized to be due to a combination of factors including tornadoes occurring at nighttime, in forested areas, prior to the peak tornado season in tornado alley, and in storms with relatively high propagation speeds. Because of this, a variety of research focused on historical data sets, mesoscale and stormscale observations, and societal impacts were supported during VORTEX-SE. One of goals for the

Purdue and University of Massachusetts-Amherst (UMass) research teams was to obtain high temporal polarimetric radar observations of severe thunderstorms.

There are some considerations when determining location and timeframe of the project. The climatological maximum for tornado probability over the southeastern U.S. is during March and April (SPC 2018). Because of this, the time period for observations occurred from early March to early May. During this period, there is a subtle geographical maximum for tornado probability over northern Alabama (SPC 2018). Because of this, and the number of existing stationary observing systems already in place, Huntsville, AL was chosen for the primary headquarters for VORTEX-SE, with the observing domain within approximately 150 km of this fixed location. Due to time and resource constraints, this was the only region picked for the observing period.

There were variety of instruments that were used by many groups in VORTEX-SE, including radiosondes, aircraft, lidar, radar, lightning mapping array, disdrometers, and many others. Of these, the most relevant to this work are the mobile radars, including the University of Massachusetts-Amherst X-Band Polarimetric Mobile Doppler Radar (UMass X-Pol), which will be discussed in the next section. Previous VORTEX projects allowed for fully mobile approach for radar observations of storms. However, this mobility was very difficult to implement in the U.S. Southeast due to complex terrain and existing vegetation. The terrain in northern Alabama is complex, especially around Sand Mountain or southern Cumberland range in northeastern Alabama (Lyza and Knupp 2016; Fig. 14, Fig. 15). In addition, northern Alabama is densely forested, resulting in few locations with open area for good radar coverage. Because of this combination, pre-scouted, fixed observing sites were selected as radar deployment locations. Each site was ranked based on percentage of azimuth sector available and minimum attainable

elevation angle. These sites were split into two radar observing domains: the “eastern domain” in northeastern Alabama (Fig. 14) and the “western domain” in northwestern Alabama (Fig. 15).

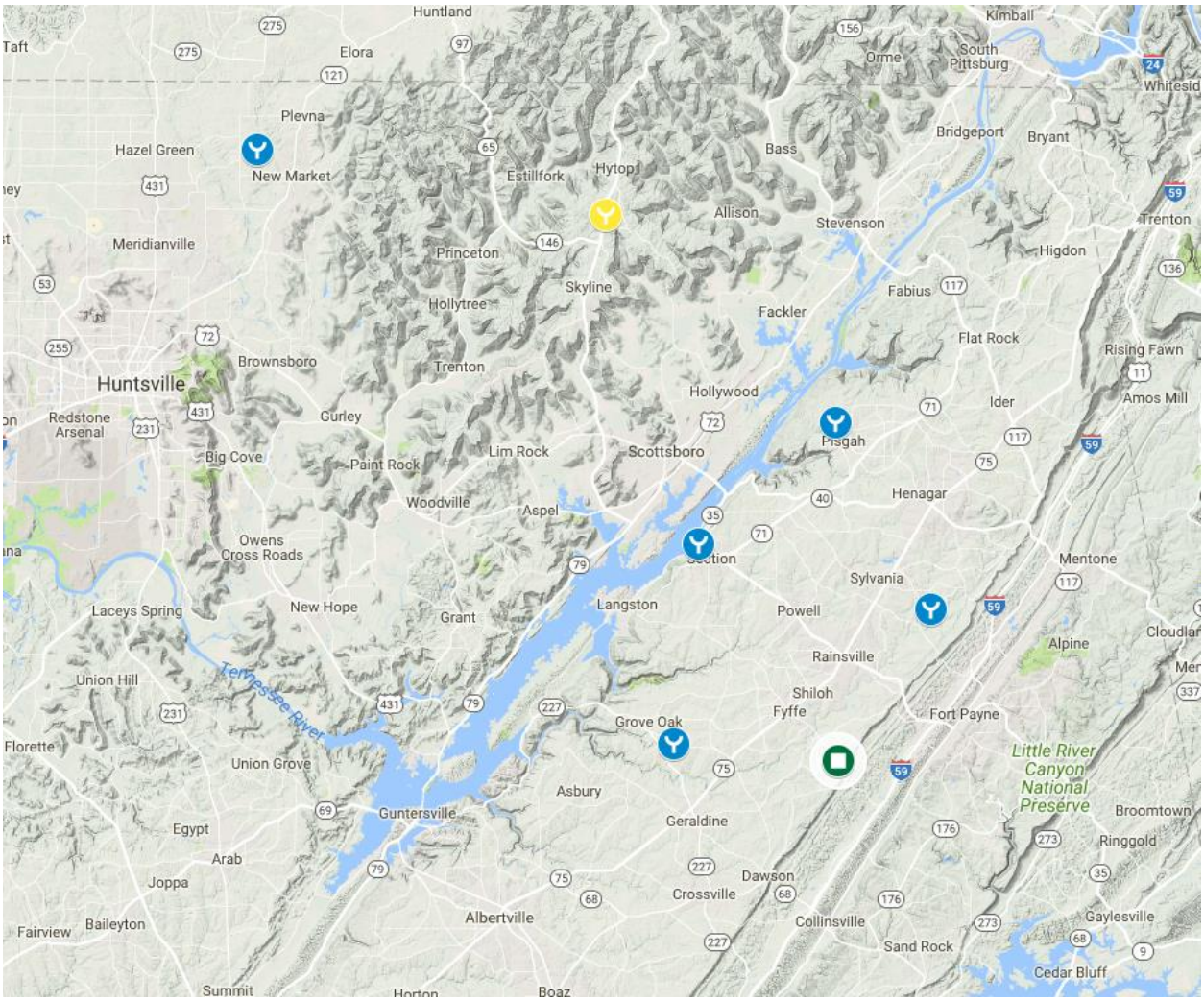

Fig. 14. Depiction of a deployment in the eastern VORTEX-SE domain. Possible mobile radar deployment sites (blue), UMass X-Pol deployment sites (green), and fixed radar sites (yellow). The fixed site here is the WSR-88D at the Huntsville, Alabama NWS (KHTX). UMass X-Pol was deployed at the annotated location for IOP3b in 2017. Map courtesy of Google Maps.

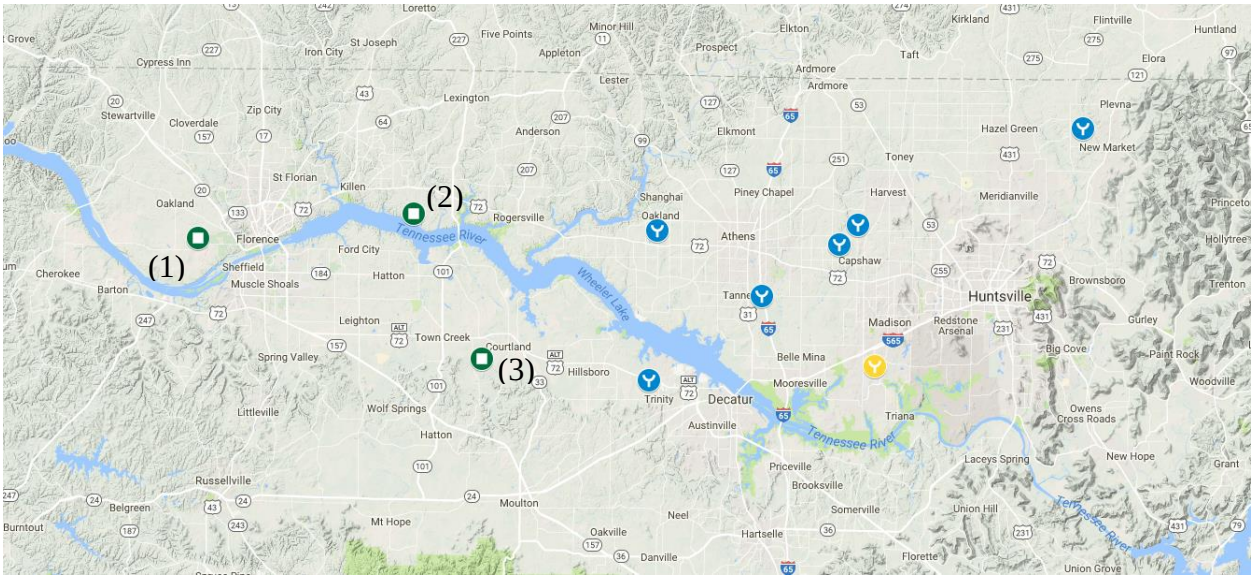

Fig. 15. As in Fig. 14, but for the western domain. The numbers are various location at which UMass X-Pol deployed where (1) was for IOP3 in 2016, (2) for IOP1b in 2017, and (3) for IOP4c in 2016.

For many institutional participants, including our team, it was not practical to be present in northern Alabama for the duration of the field campaign (March—May). For this reason, forecasting of synoptic disturbances was required to determine when there would be an IOP. Daily briefings were emailed to VORTEX-SE participants. When there was a synoptic disturbance forecast to impact the domain, a daily video conference would be held. During these video conferences, the weather forecast was led by Alabama-Huntsville student forecasters and afterwards a discussion was held between the VORTEX-SE principal investigators (PIs) regarding the forecast, science objectives, and logistics. About 3—5 days in advance, an "IOP Watch" could be issued if the signals for a severe weather event were strong enough. A go/no-go decision based on severe weather parameters (e.g. CAPE/shear combination) was usually made 1—3 days before expected severe weather, to give researchers ample time to implement their travel plans. An IOP typically consisted of one full day of travel, followed by observations of the severe weather event, and then another full day of travel back to the home institution (3 days).

An IOP could span multiple days if several severe weather events occurred in close time proximity. In this case, each event is denoted with sequentially-ordered lettering (e.g. IOP1a, IOP1b, etc.) corresponding to the chronological order of events. This lettering system is restarted for each year of operations. During the spring 2016 and spring 2017 field projects, several IOPs were observed each year, with some IOPs having a series of events observed over a brief period.

4.2 UMass X-Pol

The observational radar data used in this study was collected by the UMass X-Pol (descriptions in Junyent, F. 2003; Tanamachi et al. 2012; Snyder et al. 2013). The UMass X-Pol is a mobile, dual-polarized X-band Doppler radar that is mounted onto a customized 2003 Ford F350 truck (Fig. 16). It was built in the early 2000s and is maintained by the Microwave Remote Sensing Laboratory (MIRSL) at the University of Massachusetts-Amherst (UMass). UMass X-Pol is equipped with a magnetron transmitter, and its H- and V-polarizations are transmitted and received simultaneously (STSR). A portable generator, which can power the radar and the computer equipment for several hours, is secured to the truck bed. The UMass X-Pol has a long history of successful observations of tornadoes and severe storms (e.g. Junyent, F. 2003; Bluestein et al. 2007; Tanamachi et al. 2012; Snyder et al. 2013; among many others). Because the specifications of the UMass X-Pol (Table 2) are desirable for observations of Z_{DR} columns and it has a proven track record, the UMass X-Pol was chosen to collect observations during VORTEX-SE (Frasier et al. 2017 and Frasier et al. 2018).

Fig. 16. UMass X-Pol next to a white car with the leading edge of a thunderstorm in the background. Photo captured by the author on 27 March 2017 1903 UTC in Killen, Alabam.

Table 2. Selected specifications of UMass X-Pol.

Attribute	**UMass X-Pol**
Pulse Repetition Frequencies	2.4/1.6/0.51 kHz (triple PRT)
Transmitted Power	5 kW (per polarization)
Antenna Gain	41 dB
Half-power beam width	1.2°
Range resolution	60 m
Max/min unambiguous velocity	+/- 38.2 ms^{-1} (dual PRT)
Wavelength	3 cm
Max unambiguous range	60 km
Max azimuthal scan rate	24° s^{-1}

During a typical deployment, two or three people accompanied the UMass X-Pol, one of these people being a student engineer from UMass. The radar operators would commute from the SWIRLL building at the University of Alabama-Huntsville and arrive at designated radar deployment site usually a few hours prior to the expected occurrence of convection. Prior to

convection, a boundary layer scanning strategy was employed. This consisted of shallow PPIs, from 0—8° elevation with 1° steps. As convection initiated or propagated into UMass X-Pol's range, a different scanning strategy would be employed. When possible, narrow sector PPI scans were used to maximize temporal resolution. Maximum elevation of PPI scans depended on how close the target was; the ideal PPI scan strategy would observe the maximum height of storms when possible. If storms were persistent in a wide range of directions, full 360° volume scans were used. The scanning strategy often changed during each IOP as the event evolved and different scan strategies were needed. These details were recorded in a log.

One of the biggest advantages of using a mobile radar is the ability to bring the radar close to storms of interest to maximize spatial resolution. However, this was limited by terrain and forestry issues discussed in section 3.1. This means that storms were not always in the ideal location relative to UMass X-Pol. Several tornado-warned storms and tornadoes occurred just outside the range of the UMass X-Pol. However, since the UMass X-Pol remained stationary for the entirety of most IOPs, it allowed for the propagation of storms across the entire UMass X-Pol domain over extended periods of time. This allows for many long Z_{DR} column tracks to be observed in the UMass X-Pol domain.

4.2.1 UMass X-Pol data quality

In the post-processing of the radar data, some corrections were required before doing analysis. Calibration of Z_{DR} is essential, especially since Z_H and Z_V can drift quite substantially. This is done by taking a "birdbath" scan: the radar is vertically tilted under light rain and is rotated 360° in azimuth for several minutes (Gorgucci et al. 1999). The assumption is that the cross section of light rain is perfectly circular from below and thus Z_{DR}=0. Rotating the radar

reduces the influences from other sources, such as antenna sidelobes interacting with ground clutter, or backlobes interacting with the precipitation (Bechini et al. 2008).

Attenuation is the reduction in power of the radar transmission as it propagates through precipitation. This causes an artificial reduction in Z_H. Attenuation is dependent on the characteristics of the particle (especially size) and the particle size distribution. The effects of attenuation are most apparent in heavy rainfall and hail. It is also inversely proportional to radar wavelength, meaning it can be detrimental to X-band observations of convective storms, often resulting in complete loss of the signal through heavy precipitation cores. Differential attenuation (A_{DP}) is the difference in attenuation between the horizontally and vertically polarized transmissions. Similar to attenuation and Z_H, A_{DP} causes a reduction in Z_{DR}. Nevertheless, since ϕ_{DP} is unaffected by attenuation, it can be used to correct for A_{DP}. A simple equation is used to compute the A_{DP} factor after some smoothing to the ϕ_{DP} field:

$$A_{DP} = 0.04 * \varphi_{DP} \tag{8}$$

This equation was first proposed by Kabeche et al. (2010) and the coefficient is essentially an average of the values proposed in Bringi and Chadresekar (2001) and Snyder et al. (2010). A_{DP} is simply added to the Z_{DR} field.

4.3 Overview of Analyzed IOPs

Eight IOPs were observed in total during the 2016—17 spring VORTEX-SE campaigns, many of which had several events. Due to the nature of the VORTEX-SE project, which was described in section 3.1, the number of applicable cases were limited. Since it was not feasible for many researchers to stay in the observing domain for the duration of the project, forecasts were required to make a go/no-go decision several days prior to the observing period. Often

times, these forecasts significantly changed and were vastly different than what actually occurred. This resulted in many events being missed, and several null cases observed. However, there were still many convective events observed. Events were chosen based on quality of data, severity of event, uniqueness of event, and convective storm type. In order to test the strengths, weaknesses, and limitations of the automated identification and tracking algorithms, it is desirable to have a wide variety in the dataset. Each IOP posed its unique challenges and characteristics. A brief synopsis of each event as well as the general situation of the observations are described in the following subsections.

4.3.1 5 April 2017: IOP3b (2017)

The overall synoptic pattern was very supportive of a severe weather outbreak. A deep 500 mb trough was located over the southern Great Plains at 1200 UTC with a 300 mb 100 knot jet streak across northeastern Texas, southeastern Oklahoma, and Arkansas (Fig. 17; Fig. 18). A surface low was in Missouri with a cold front extended through Arkansas and Louisiana. The cold front was projected to propagate through Alabama later that evening (Fig. 19). A weak warm front developed the previous night, producing a warm sector in the southern half of Alabama containing dewpoints in the upper 60s to lower 70s. Widespread convection initiated in the warm sector late overnight and persisted well into the morning. The strongest storms occurred south of the VORTEX-SE domain with numerous reports of large hail, damaging winds and a couple of tornadoes in the early morning hours in central Alabama (Fig. 20). This convection had largely moved out of Alabama by the afternoon, leaving a more stable atmosphere with a significant capping inversion. Instability gradually increased during the afternoon with strong southerly flow increasing dew points into the low-mid 60s. The combination of radiative heating and warm air advection allowed instability to build over the

area, with surface based convective available potential energy (SBCAPE) reaching as high as 3500 J/kg by 2100 UTC in central Alabama (Fig. 21). Vertical wind shear was exceptionally high, with peak 0—6 km shear over 80 kts over northeastern Alabama and northwestern Georgia. As the cold front moved eastward, it initiated convection over central Alabama around 2000 UTC. Storm mode was mostly isolated, with many supercells moving through the domain. However, these storms did not quite reach their expected strength in northwestern Alabama, with only severe hail being produced. There are a few theories as to why these storms under-produced, though that subject is beyond the scope of this research.

Because of the synoptic setup and the expected maximum severe weather potential, operations took place in the eastern half of the VORTX-SE domain. UMass X-Pol was deployed in a spot just west of Fort Payne, in northeastern Alabama (Fig. 14). Though the UMass X-Pol deployed around 1130 UTC to observe the morning convection, the radar was blocked to the south, which is where the convection was occurring. Around 2030 UTC, at the invitation of a property owner, the UMass X-Pol was relocated to a neighboring driveway, improving the azimuthal sectors to the southwest and east. This move which ended up being essential to observing a left moving supercell to the east. Scanning continued to almost 0100 UTC before VORTEX-SE operations ended. Additional details regarding UMass X-Pol's deployment for this IOP can be viewed on the VORTEX-SE 2017 Field Catalog page (Lafleur and Saunders 2018).

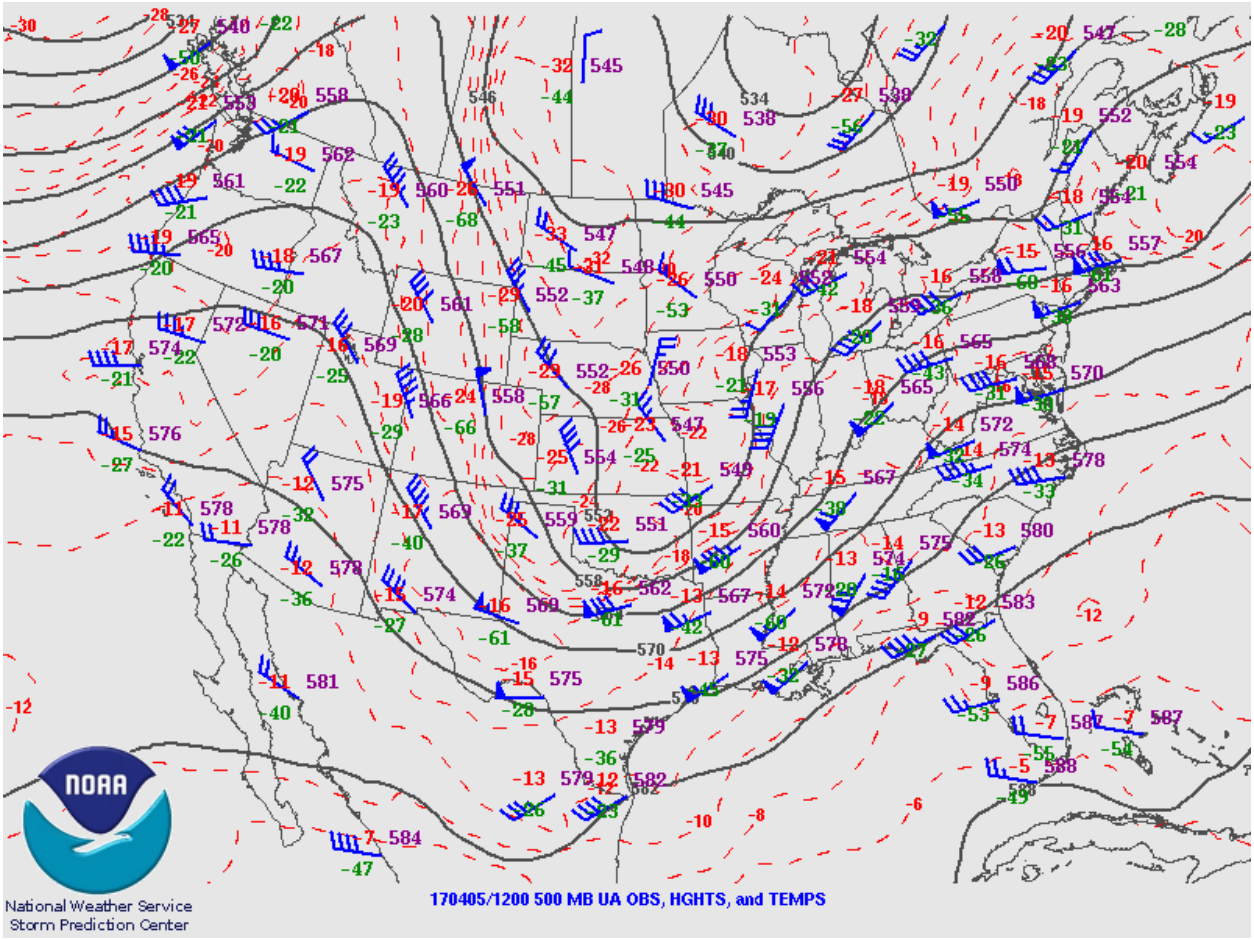

Fig. 17. A map of 500 hPa observations at 1200 UTC 05 April 2017, which is provided by SPC. Plotted on a 500 hPa surface are geopotential heights (black solid contours), temperature (red dashed contours), and observations from each NWS office with upper air observations.

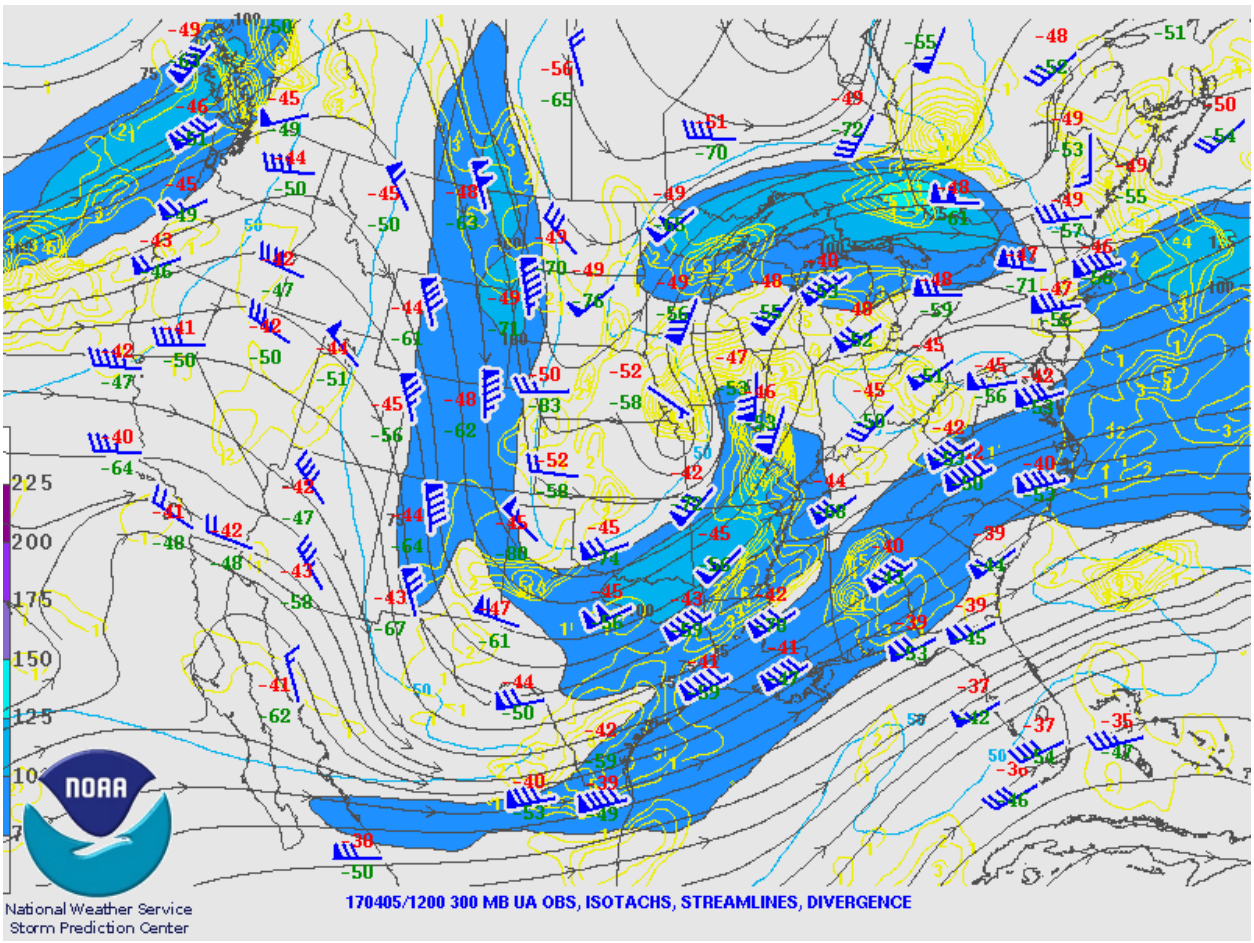

Fig. 18. A map of 300 hPa observations at 1200 UTC 05 April 2017, which is provided by SPC. Plotted are wind speed (color filled; 50 kts is solid light blue contours), streamlines (black solid lines with arrows), divergence (yellow solid contours) and observations from each NWS office with upper air observations.

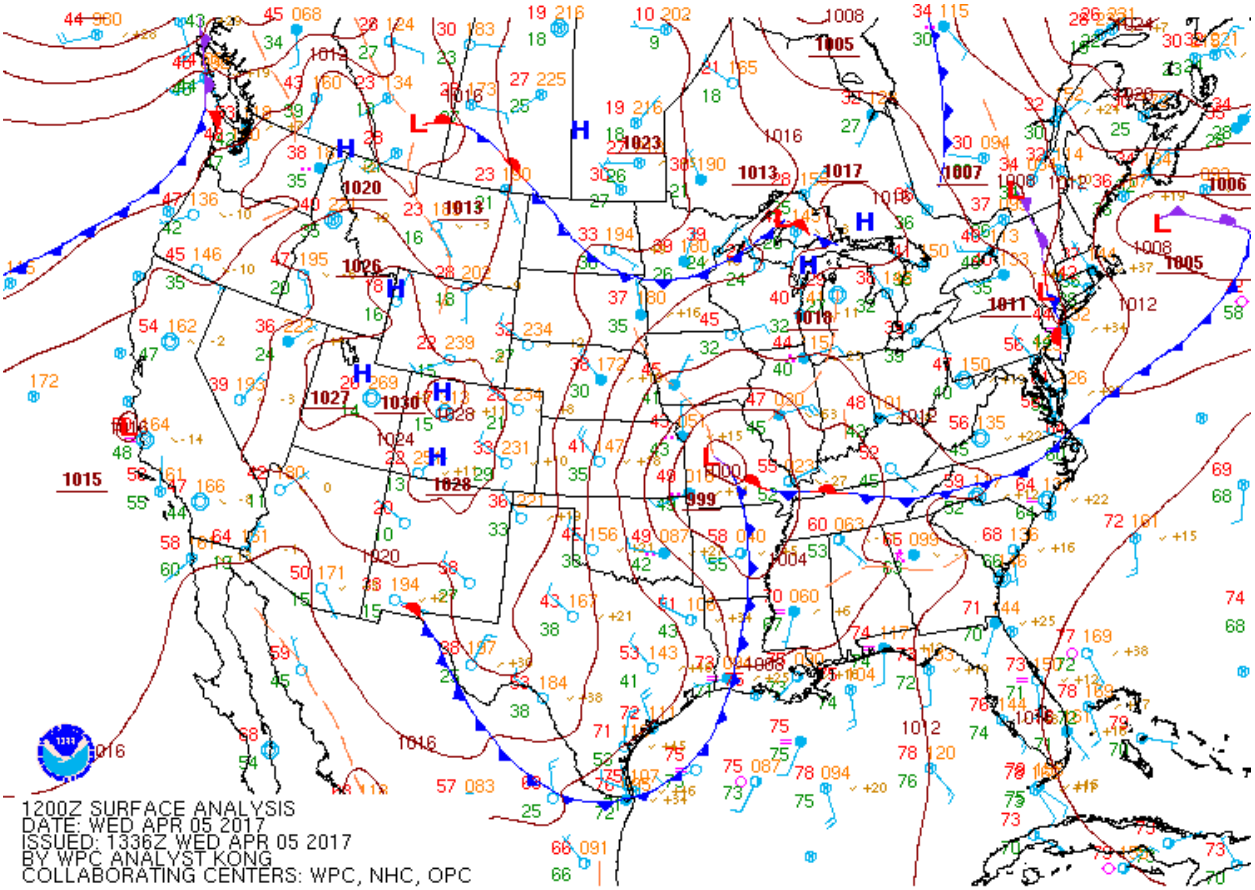

Fig. 19. A surface analysis map at 1200 UTC 05 April 2017, provided by the Weather Prediction Center (WPC). Plotted are surface observations (temperatures and dewpoints are in °F), mean sea level pressure (MSLP, in hPa; dark-red solid contours), frontal boundaries and high/low pressure extrema, with pressure values printed next to them (in hPa, dark-red, underlined).

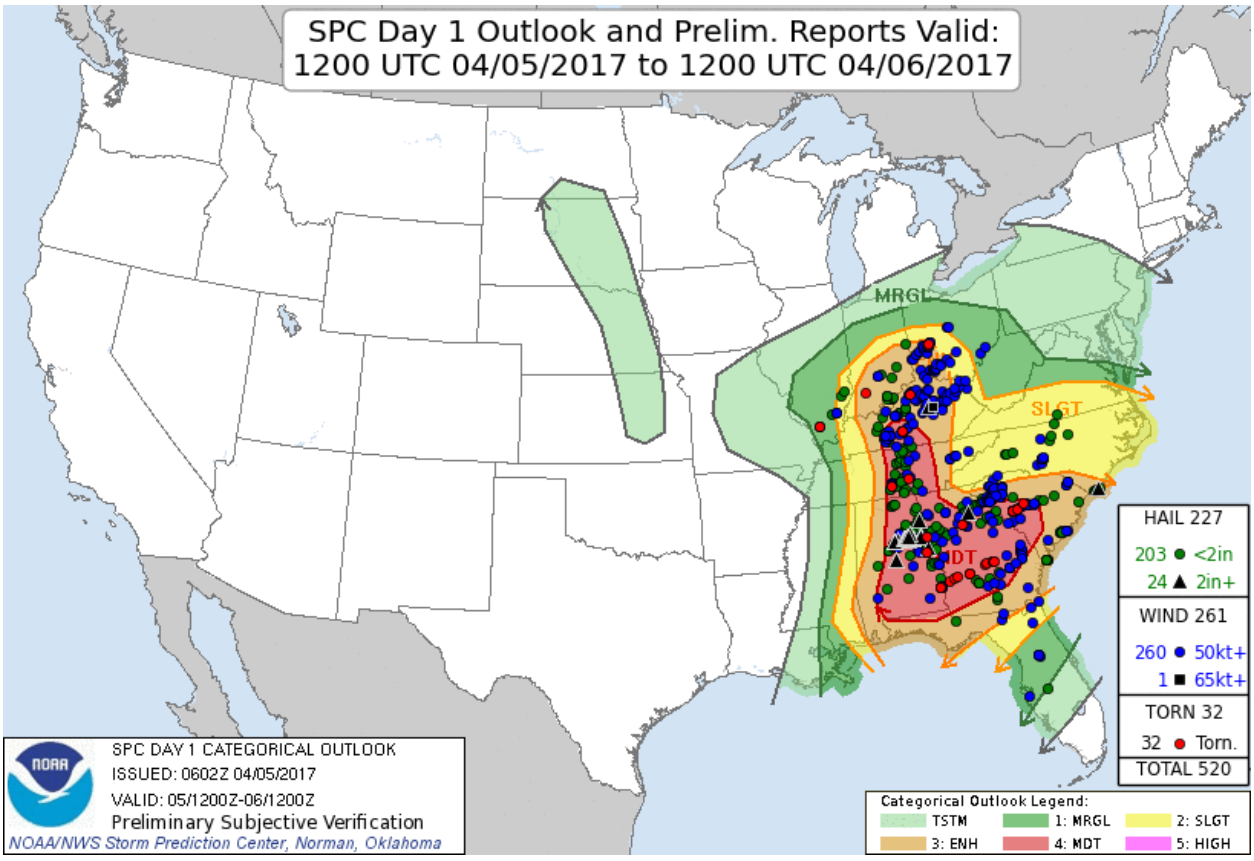

Fig. 20. The day 1 outlook issued by the SPC for 1200 UTC 05 April 2017 to 1200 UTC 06 April 2017. Each color fill represents a different category of risk for severe weather: light green=general thunderstorms, dark green=marginal risk, yellow=slight risk, orange=enhanced risk, red=moderate risk. In addition to this, reported severe weather is also plotted. Severe hail (1 in+) are green, severe winds (50+ kt) are blue, and tornadoes are red. Significant severe weather (wind=65kt+, hail=2+ in). are black.

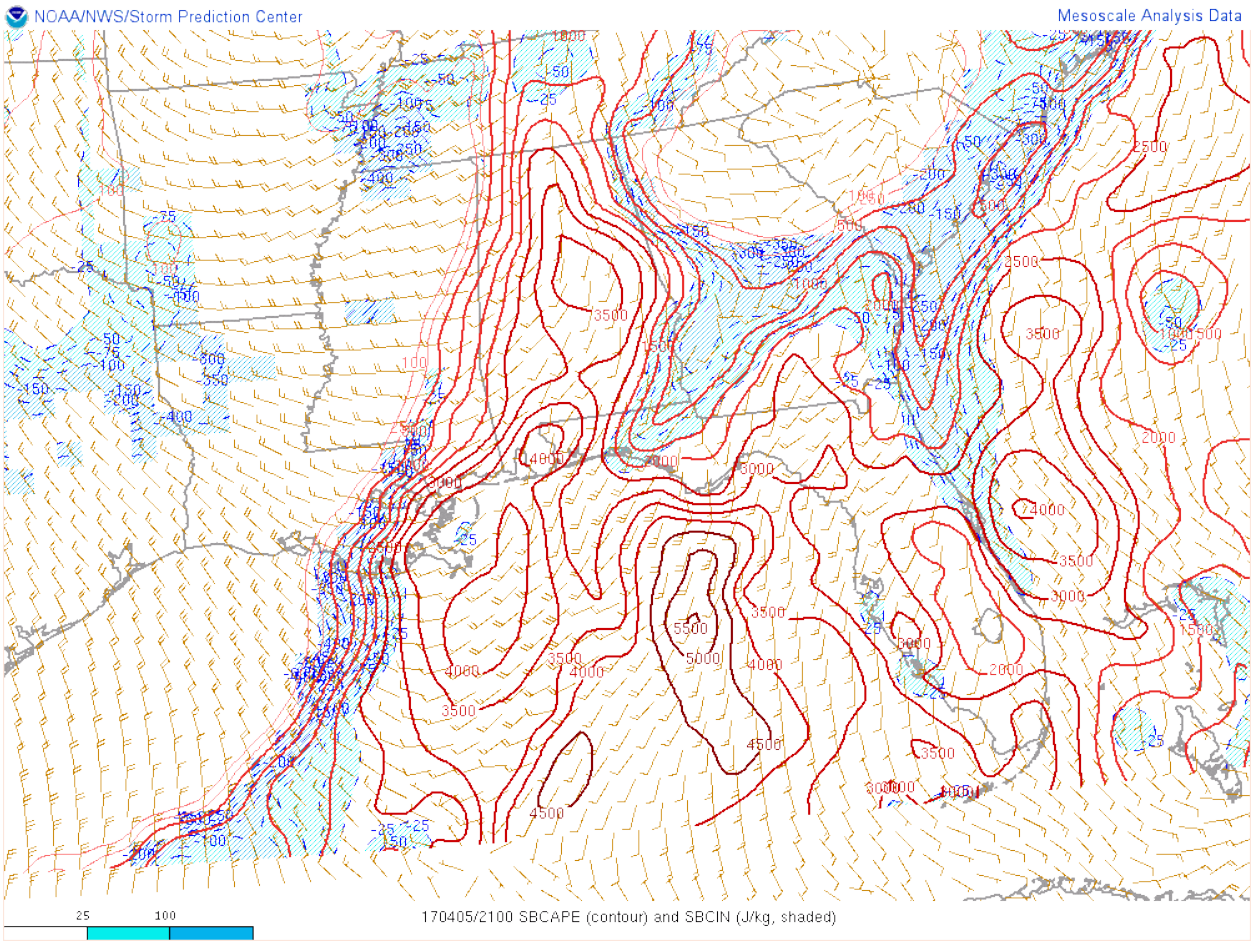

Fig. 21. A map of analyzed SBCAPE (in J kg^{-1}, red solid contours), surface based convective inhibition (SBCIN; in J kg^{-1} blue color fill), and surface wind barbs (in kt) for 2100 UTC 05 April 2017. Map provided by SPC.

4.3.2 27 March 2017: IOP1b (2017)

A slightly negatively tilted 500 mb trough was located over the southern Great Plains at 1200 UTC on 27 March 2017 (Fig. 22). The associated surface low was positioned in northwestern Arkansas just downstream of the upper level low (Fig. 23). As expected, the near surface southerly flow and radiative heating allowed instability to build during the day with moderate SBCAPE increasing to more than 2000 J kg^{-1} across the warm sector (Fig. 24). Storms initiated in Mississippi and western Tennessee in the late morning hours, propagating into the western VORTEX-SE domain by 1900 UTC (Fig. 25). Initially, these storms were discrete, but

they quickly grew upscale into several clusters of storms. Several cells had rotating updrafts and produced severe weather across the area, including a few tornadoes just outside of the VORTEX-SE domain. The second round of storms originated in Tennessee as a southward-propagating MCS, entering northwestern Alabama just after sunset around 0100 UTC. This round of storms produced several tornadoes in Tennessee and a few reports of large hail in Alabama and Tennessee.

Forecasts had continuously highlighted areas north and west of the VORTEX-SE domain as having the highest chance for severe weather, which is where the SPC issued a day 1 enhanced risk for convective storms (Fig. 26). Within the constrained VORTEX-SE domain, locations farthest north and west presented the greatest chance for observing severe weather. For this reason, principal investigators (PIs) chose the western domain for observations during IOP1b. UMass X-Pol deployed approximately 15 miles east of Florence, AL (Fig. 15). Radar scans began at 1600 UTC, several hours prior to convection entering the domain. The initial scan strategy was more conducive for boundary layer observations. As convection entered the domain, a different scan strategy involving deeper elevations was employed. Scanning continued through both rounds of convection until about 0400 UTC, though was not perfectly continuous. Additional details regarding UMass X-Pol's deployment for this IOP can be viewed on the VORTEX-SE 2017 Field Catalog page (Saunders and Lafleur 2018).

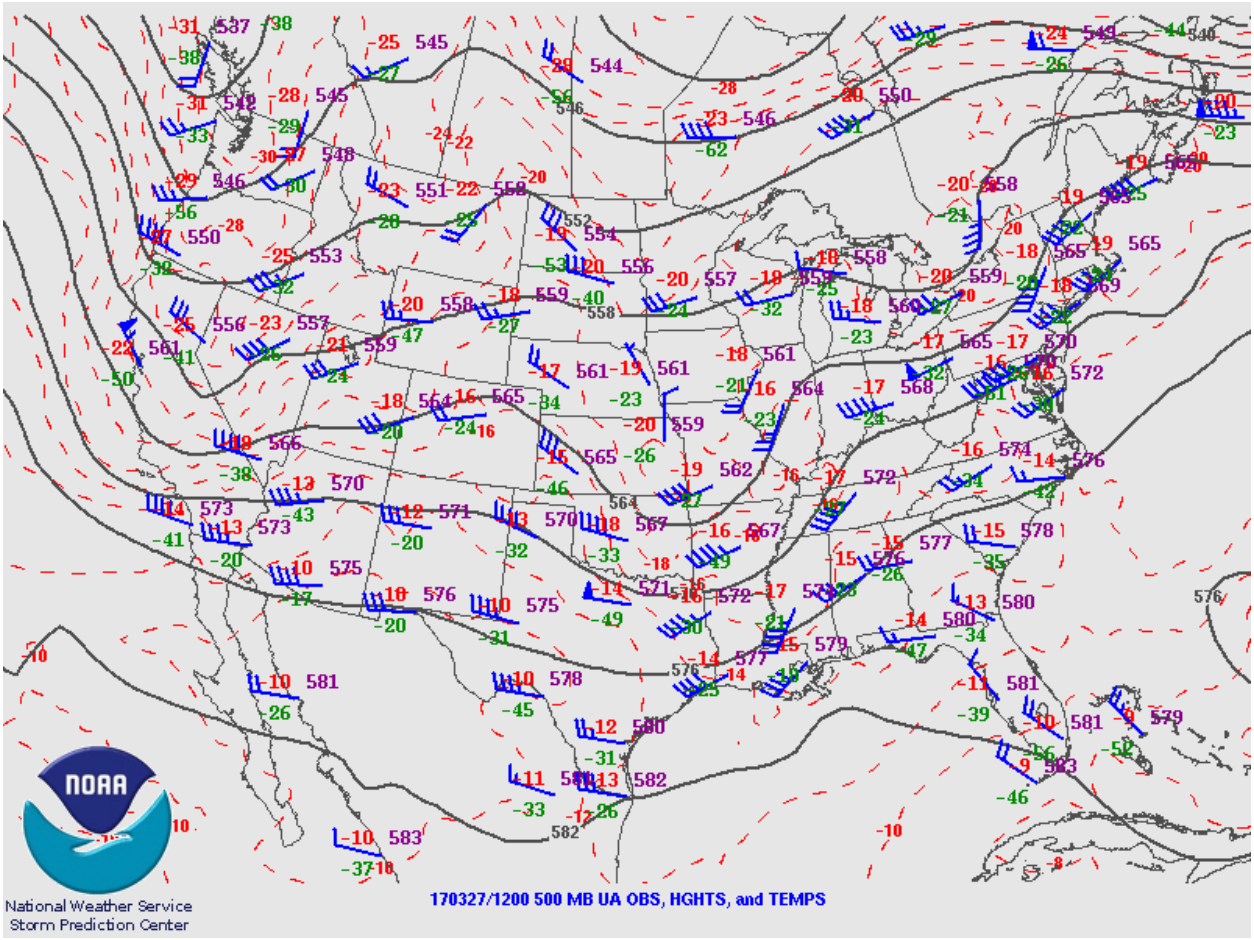

Fig. 22. As in Fig. 17 for 1200 UTC 27 March 2017.

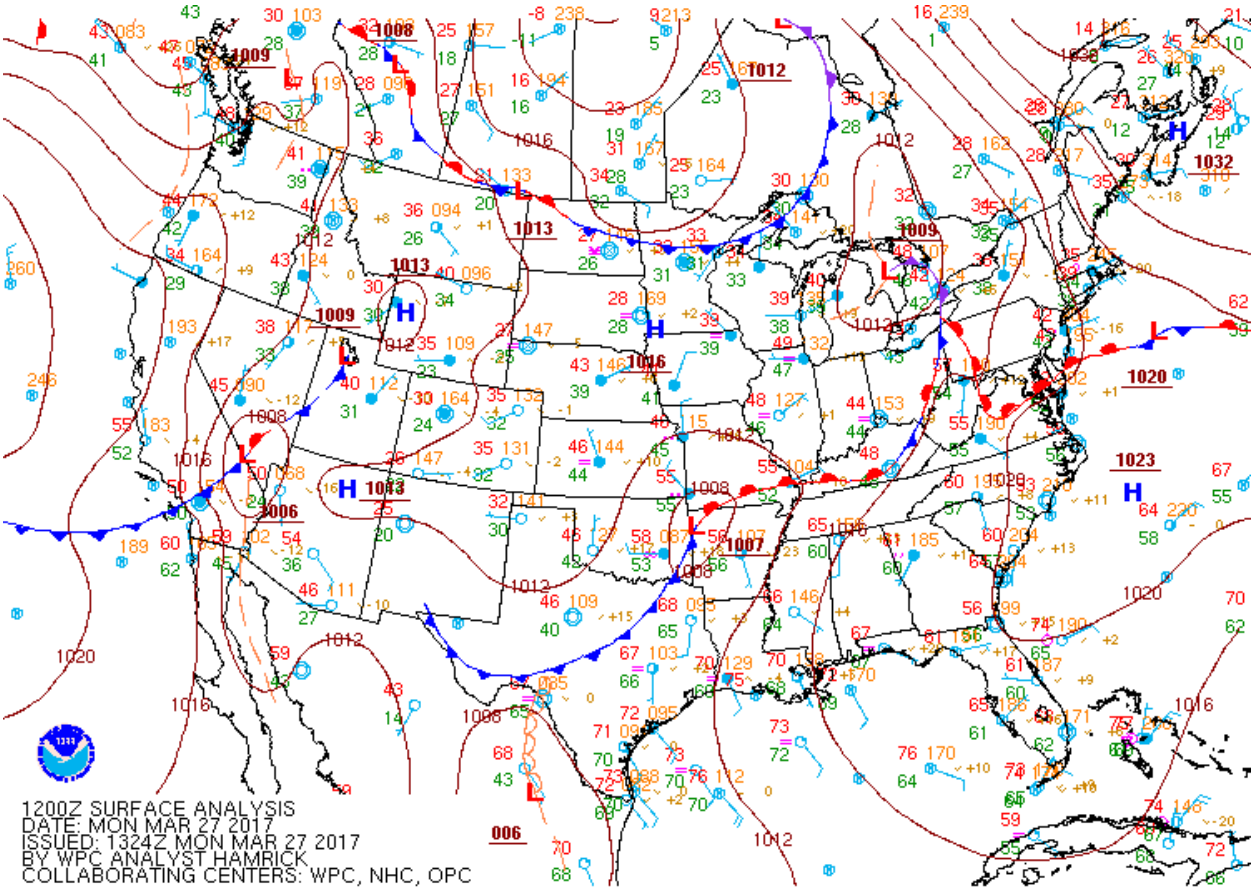

Fig. 23. As in Fig. 19 for 1200 UTC 27 March 2017.

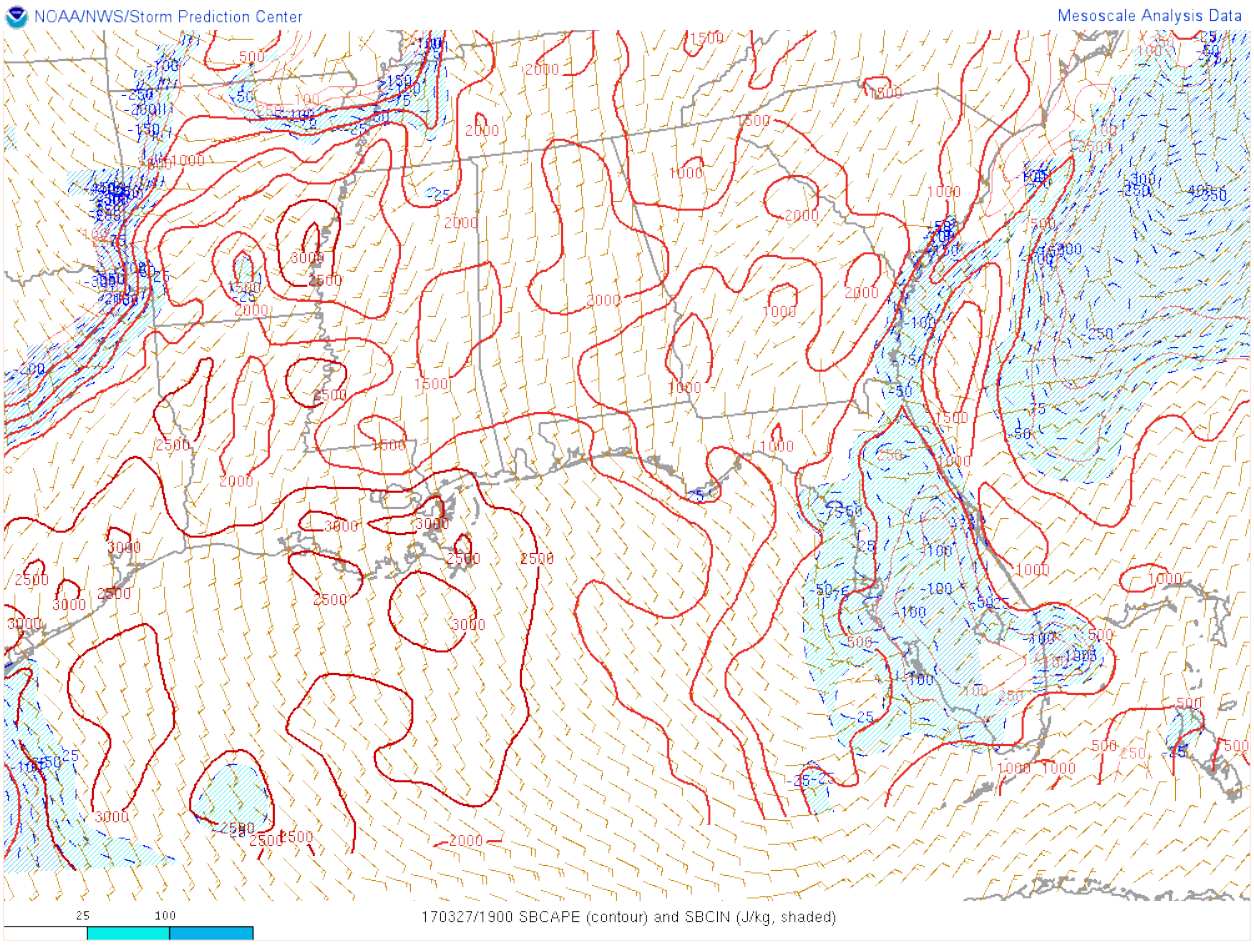

Fig. 24. As in Fig. 21 for 1900 UTC 27 March 2017.

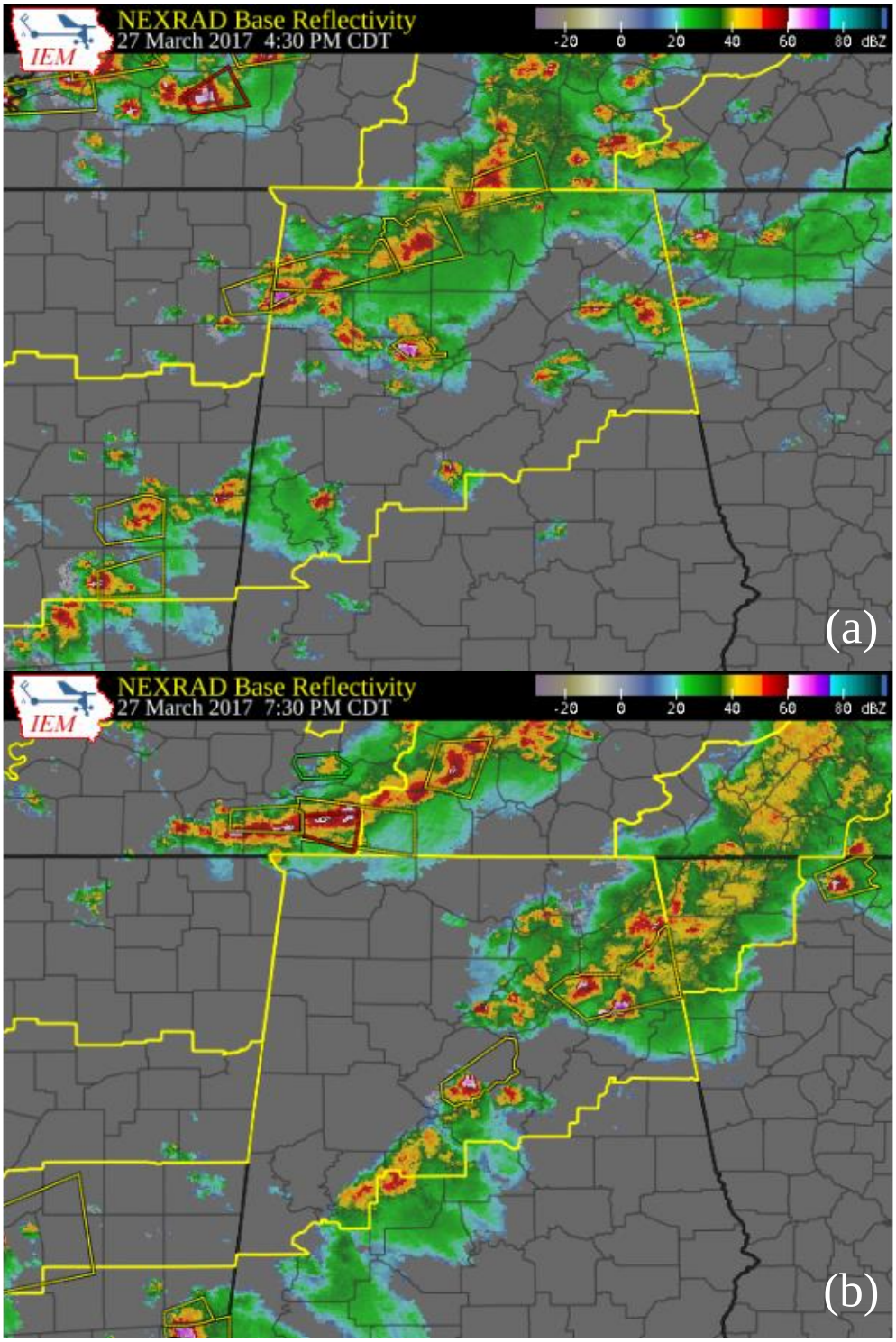

Fig. 25. Mosaic of NEXRAD base reflectivity (in dBZ) for 2110 UTC 27 March 2017 (a) and 0010 UTC 28 March 2017 (b) over the VORTEX-Southeast domain. Thick yellow lines enclose SPC-issued severe thunderstorm watches. Smaller yellow, red, and green polygons enclose NWS-issued severe thunderstorm, tornado, and flood warnings, respectively. Images obtained from the Iowa State University Iowa Environment Mesonet (ISU IEM) website.

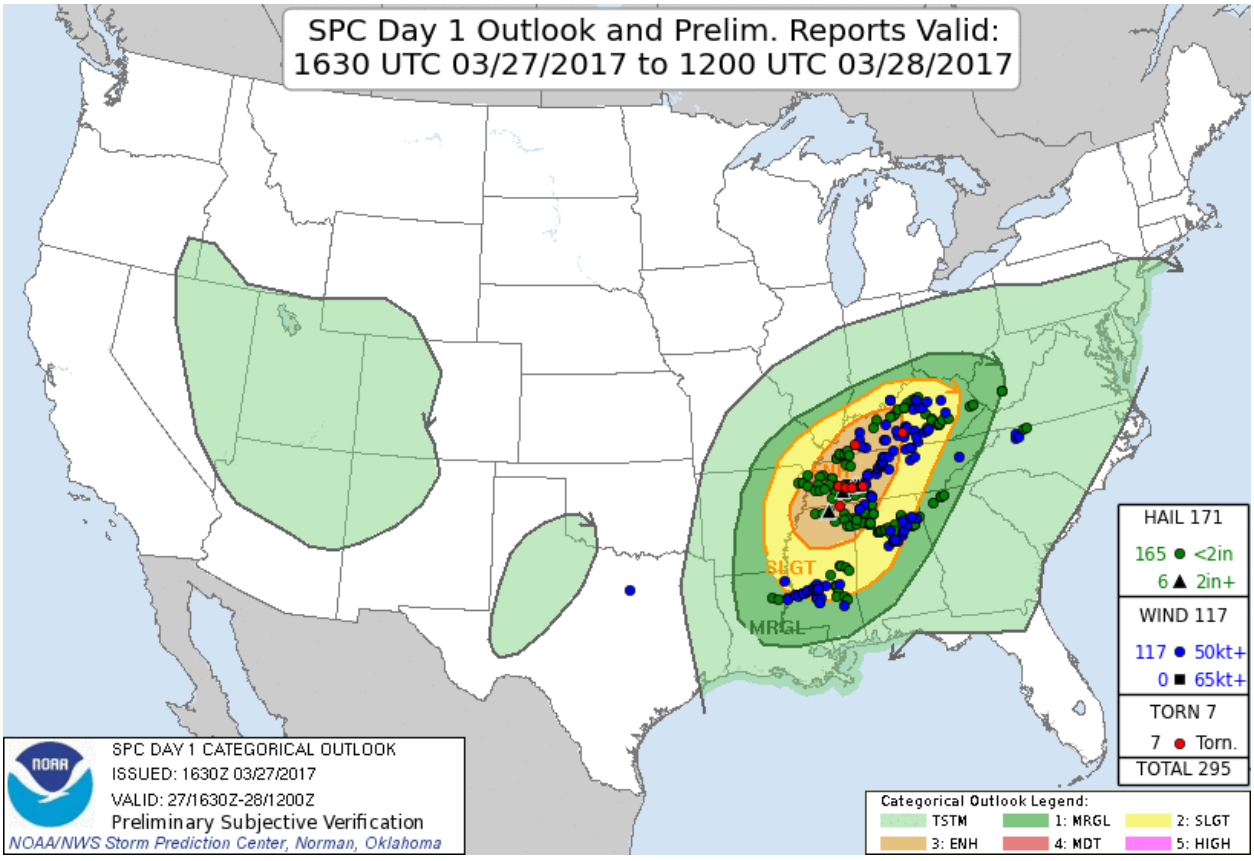

Fig. 26. As in Fig. 19 for 1630 UTC 27 March 2017 to 1200 UTC 28 March 2017.

4.3.3 31 March 2016: IOP3 (2016)

A slowly moving upper level disturbance (Fig. 27) and strong 850 mb low level jet (Fig. 28) helped fuel moderate-to-heavy precipitation overnight into the morning of 31 March 2016. Precipitation exited Alabama by the early-to-midafternoon hours, leaving behind a very moist but rather stable atmosphere. In fact, it was so stable that the 1200 UTC sounding at BMX yielded 0 Jkg^{-1} of SBCAPE (Fig. 29). At 1500 UTC, a 992 hPa surface low was located over eastern Iowa, with a cold front extending down to Mexico (Fig. 30). A very warm and moist airmass was in place over the southern Gulf States. As the cold front advanced eastward, it initiated severe storms in Louisiana. These storms grew upscale quickly and reached the VORTEX-SE domain in northern Alabama by 0000 UTC on 1 April 2016 (Fig. 31). Strong,

moist southerly low-level flow and insolation through clear skies destabilized the airmass in Mississippi and Alabama following the morning precipitation, allowing these storms to stay severe as they propagated eastward (Fig. 31). Additionally, vertical wind shear was strong, with 0—6 km bulk shear as high as 65 knots. A wide variety of storm types were observed, including multicellular, supercellular and MCS (Fig. 31a, b). Several tornadoes were reported with these storms from central Alabama to southern Tennessee, along with wind and hail (Fig. 32).

Due to the synoptic scale setup, severe weather was favorable for a rather large area, for which marginal and slight risks for severe weather were issued by the SPC (Fig. 32). The highest chance for severe weather was confined to the Tennessee Valley and portions of the southern Gulf States, for which the SPC issued an enhanced risk with the highest concern being tornadoes and severe winds. Though, probabilities for severe weather between the two VORTEX-SE domains were very close, decision makers felt that the western domain yielded the greatest opportunities for the VORTEX-SE science objectives. UMass X-Pol deployed in a location just west of Florence, AL (Fig. 15). Scanning started at 2000 UTC, about two hours prior to convection entering the maximum range of UMass X-Pol. Observations were near continuous until about 0400 UTC when the IOP ended. Additional details regarding UMass X-Pol's deployment for this IOP can be viewed on the VORTEX-SE 2016 Field Catalog page (Seedorf and Heberling 2018).

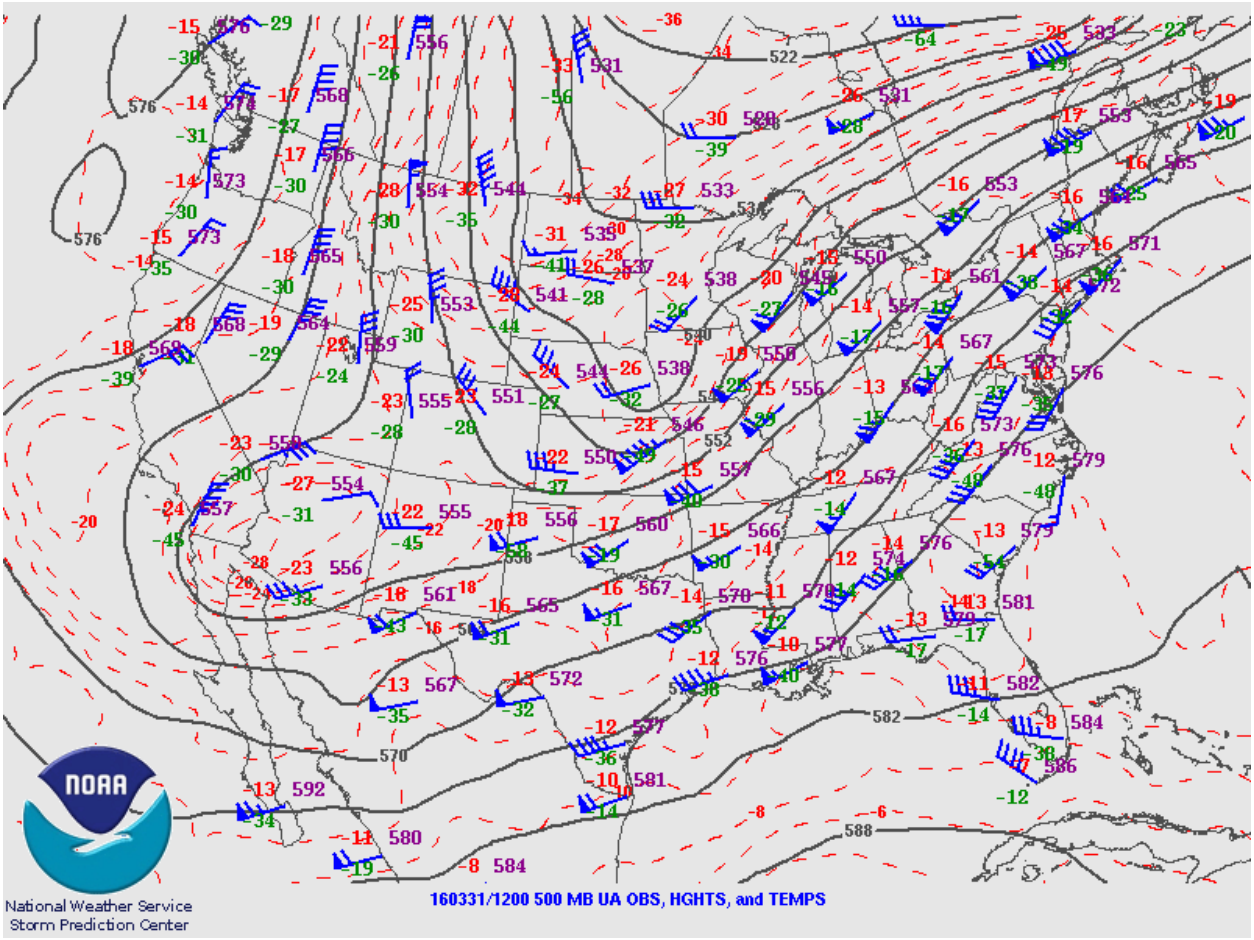

Fig. 27. As in Fig. 17 for 1200 UTC 31 March 2016.

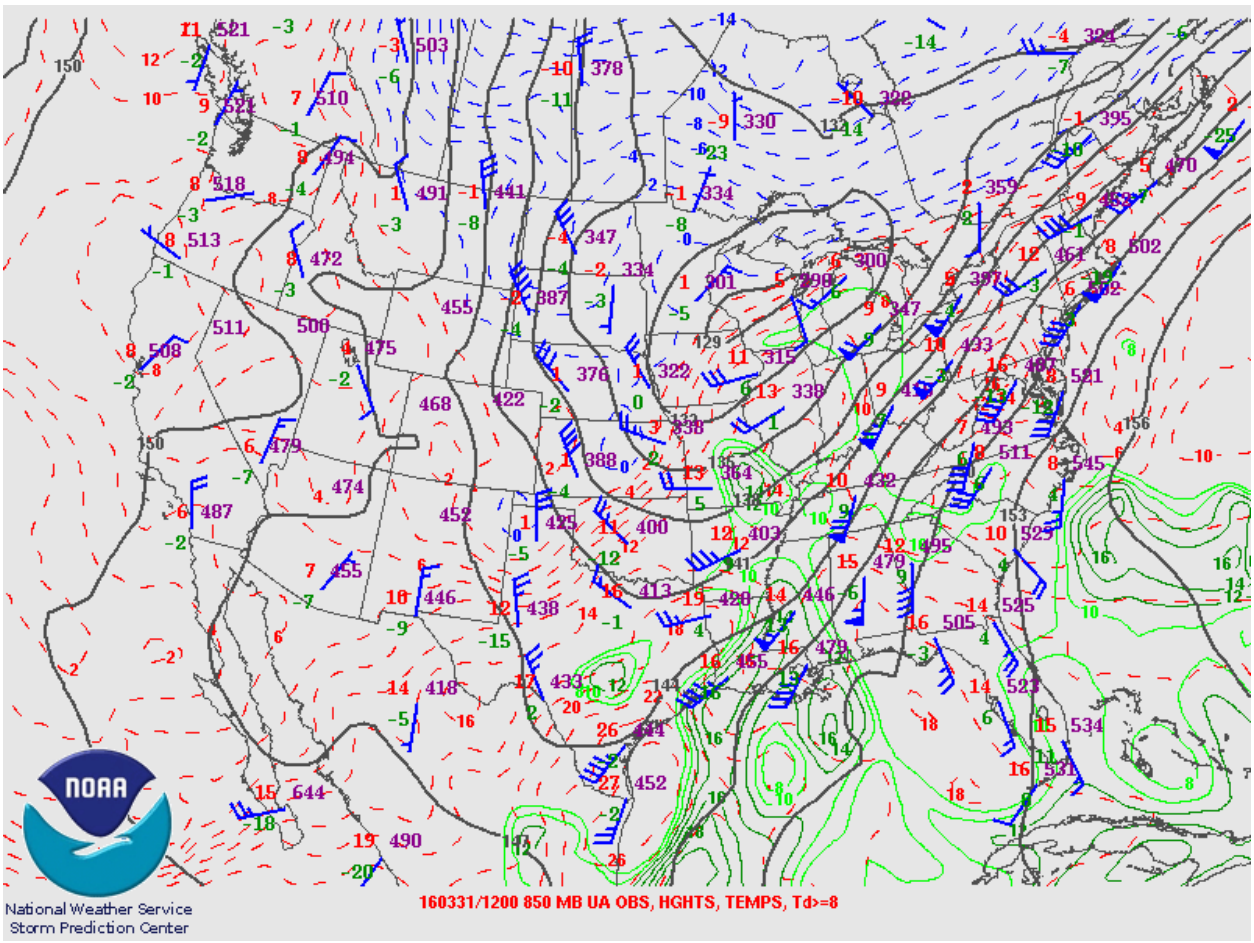

Fig. 28. An 850 hPa map with geopotential heights (black solid contours), temperature (red dashed contours), dewpoint greater than eight (green solid contours), and observations. Map is provided by SPC.

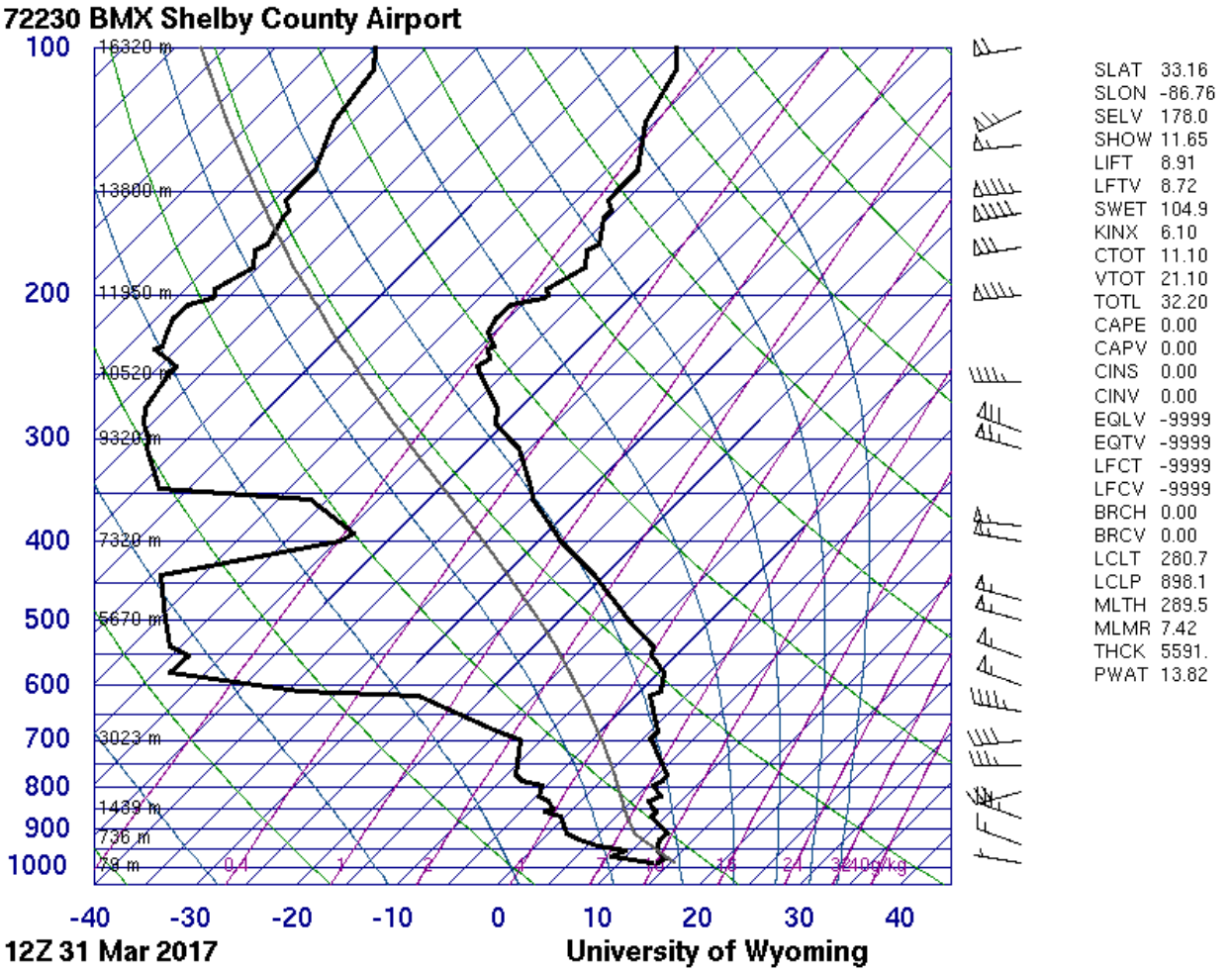

Fig. 29. Skew-T diagram off the sounding at BMX Shelby County, Calera, Alabama Airport at 1200 UTC on 31 March 2017. To interpret a skew-t diagram, see Air Weather Service (1979). The sounding indices are further described at University of Wyoming (2018). Image courtesy of the University of Wyoming.

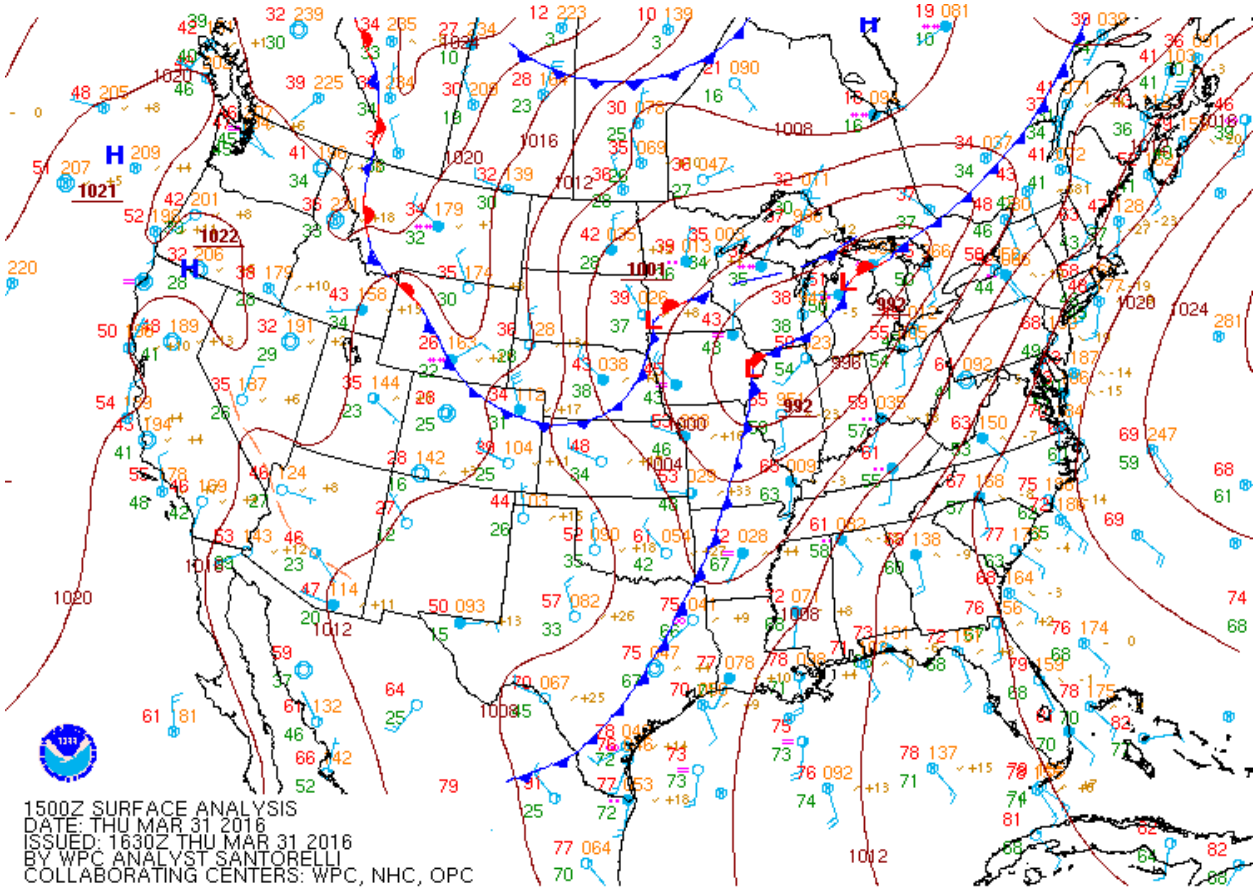

Fig. 30. As in Fig. 19 for 1500 UTC 31 March 2016

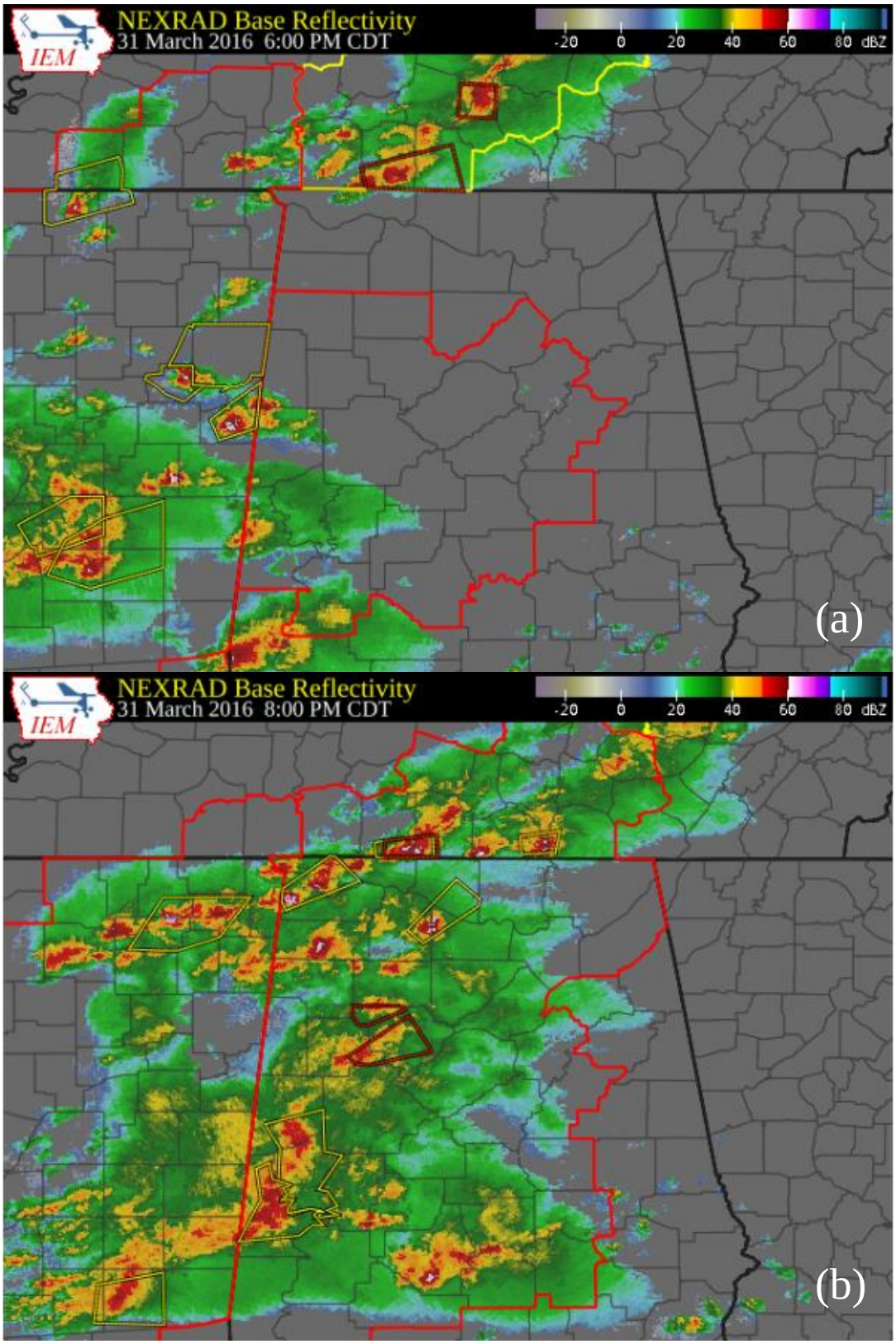

Fig. 31. As in Fig. 25 for 2300 UTC 31 March 2016 and 0100 UTC 1 April 2016.

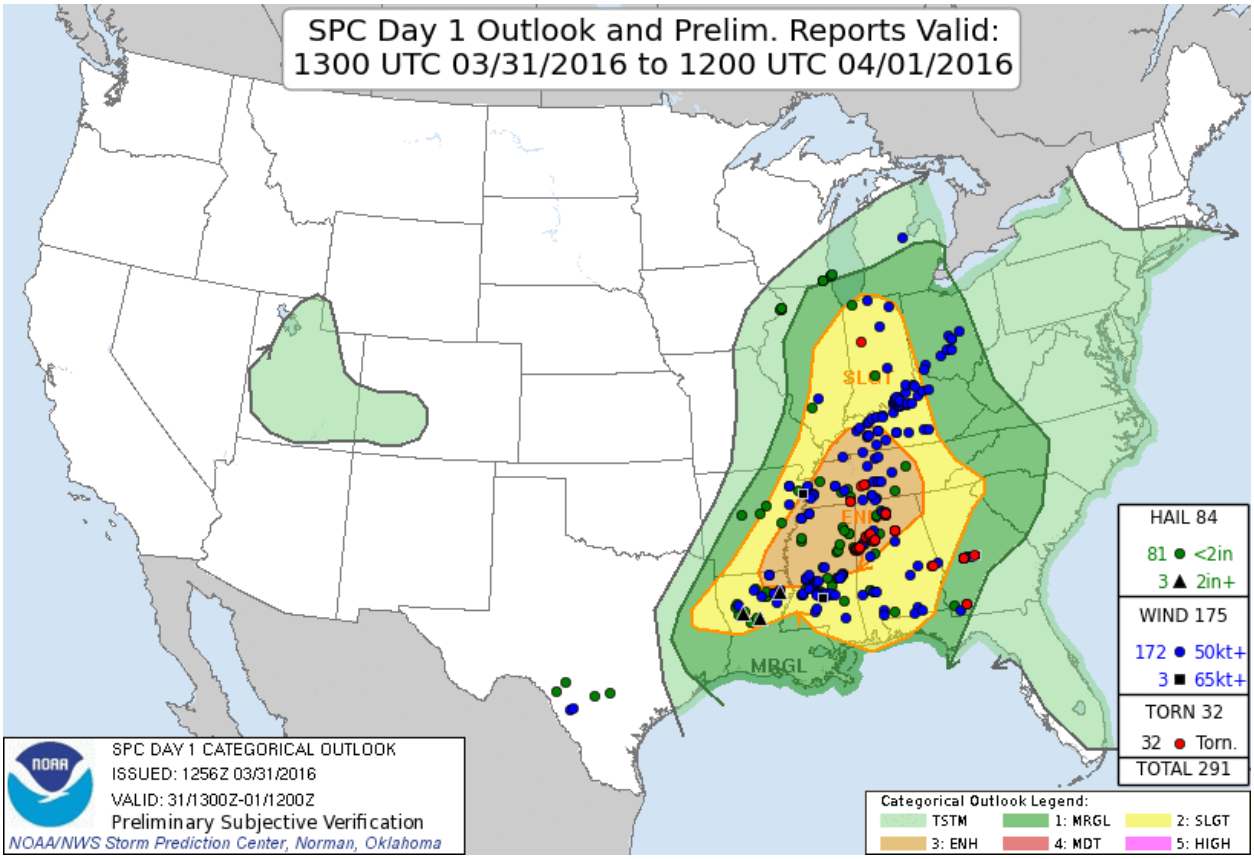

Fig. 32. As in Fig. 19 for 1300 UTC 31 March 2016 to 1200 UTC 1 April 2016.

4.3.4 30 April 2016: IOP4c (2016)

At 1200 UTC on 30 April 2016, a broad upper level trough covered much of the western CONUS, with southwesterly flow over the southern gulf states (Fig. 33). A shortwave was moving northeastward over Missouri around the periphery of the large scale upper level trough. The associated surface low was near Kansas City occluded and slowly moved north while its connected cold front advanced eastward (Fig. 34). Initial forecasts had large uncertainty due to widespread cloud coverage, which also covered the VORTEX-SE domain early on. SPC had a large area under a slight and marginal risk (Fig. 35), especially for areas that were able to destabilize after morning cloud cover. The situation was not particularly favorable for Alabama,

though local conditions allowed for an isolated supercell to develop in the afternoon. After cloud cover gave away, radiative heating and southerly low-level flow allowed CAPE to build up to 1000+J/kg (Fig. 36). Furthermore, 0—6 km bulk wind shear reached as high as 50 knots, with the highest values found in northwestern Alabama (Fig. 37). There was a small corridor in which instability and vertical wind shear were sufficient for a severe thunderstorm. A small cluster of storms developed in northwestern Alabama around 2000 UTC, and it propagated through northeastward into Tennessee (Fig. 38).

As mentioned above, there was significant uncertainty in the forecast initially. It was decided that the western domain gave the best chance to observe severe weather due to larger vertical wind shear and better timing of thunderstorms during daylight hours. For this reason, VORTEX-SE operated in the western domain for this IOP. UMass X-Pol deployed at the Courtland, Alabama Airport, which is located northwest of Decatur, Alabama and southeast of Florence, Alabama (Fig. 15). The deployment began about an hour prior to the first initiation of convection and lasted until approximately 0000 UTC on 1 April 2016. Additional details regarding UMass X-Pol's deployment for this IOP can be viewed on the VORTEX-SE 2016 Field Catalog page (Tanamachi and Waldinger 2018).

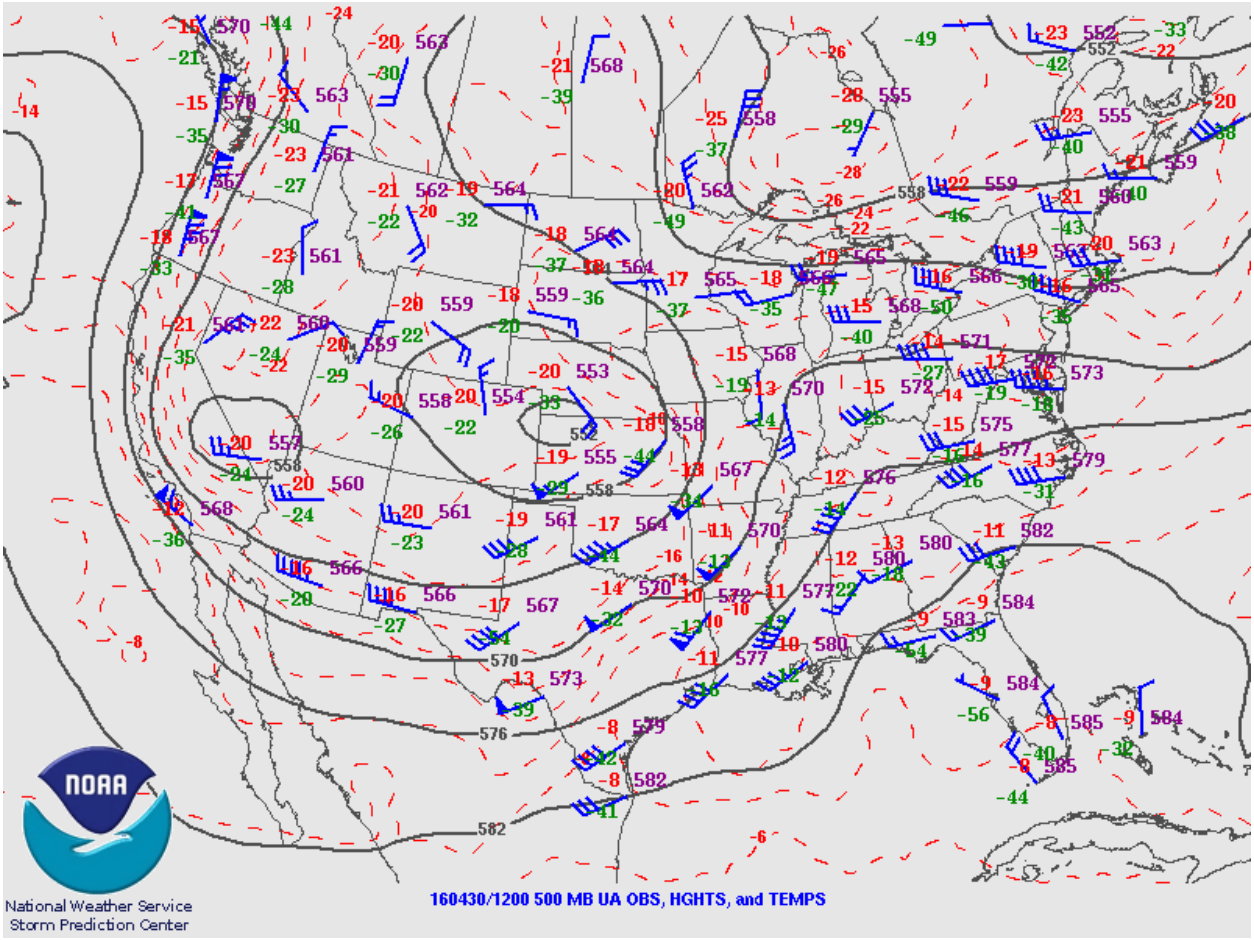

Fig. 33. As in Fig. 17 for 1200 UTC 30 April 2016.

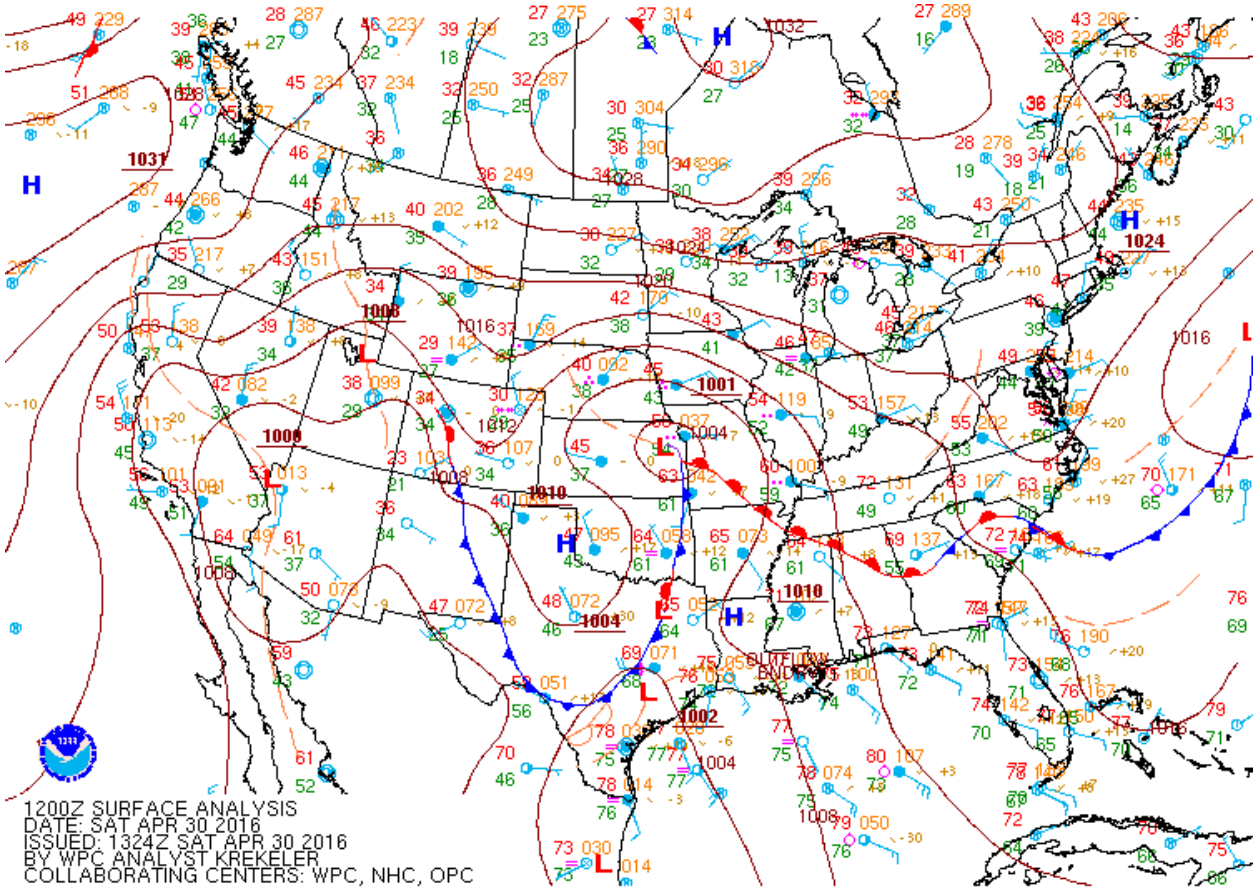

Fig. 34. As in Fig. 19 for 1200 UTC 30 April 2016.

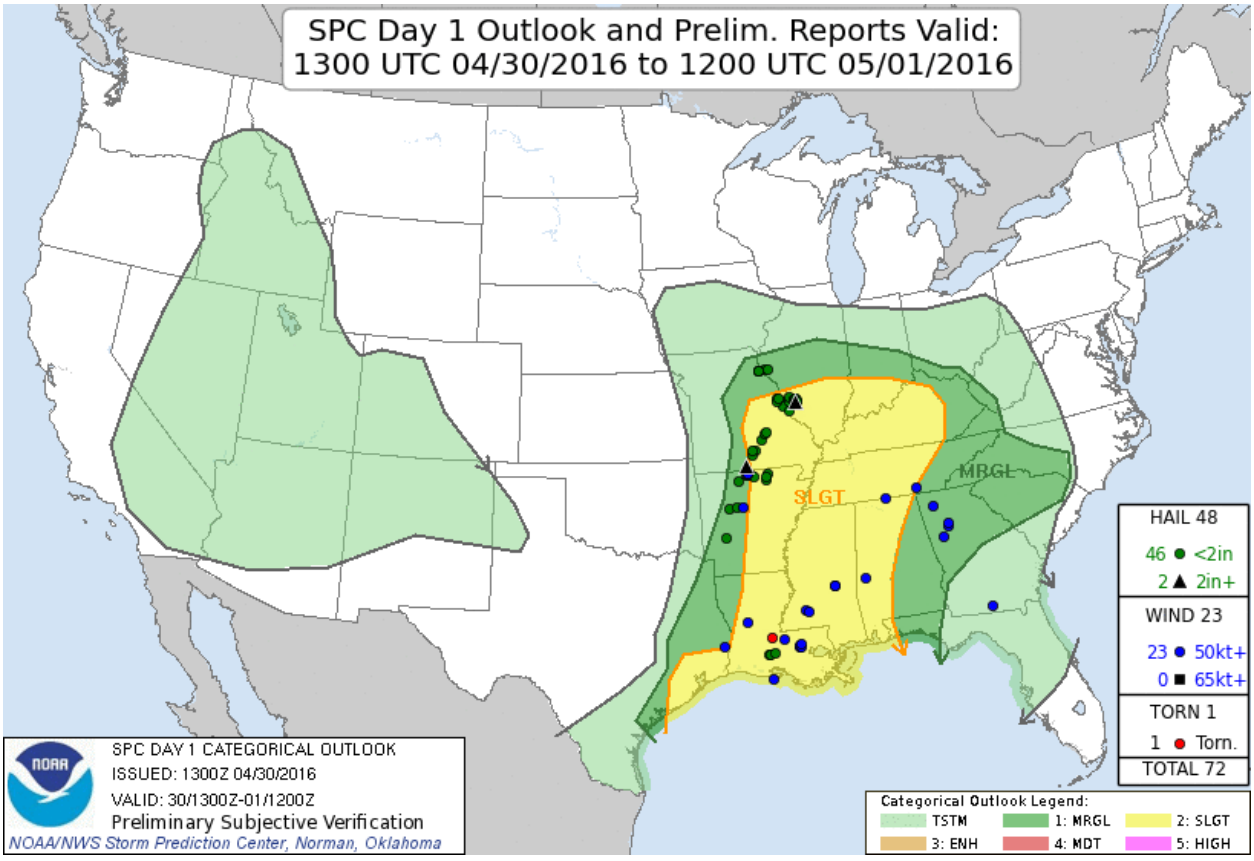

Fig. 35. As in Fig. 20 for 1300Z 30 April 2016 to 1200 UTC 1 May 2016.

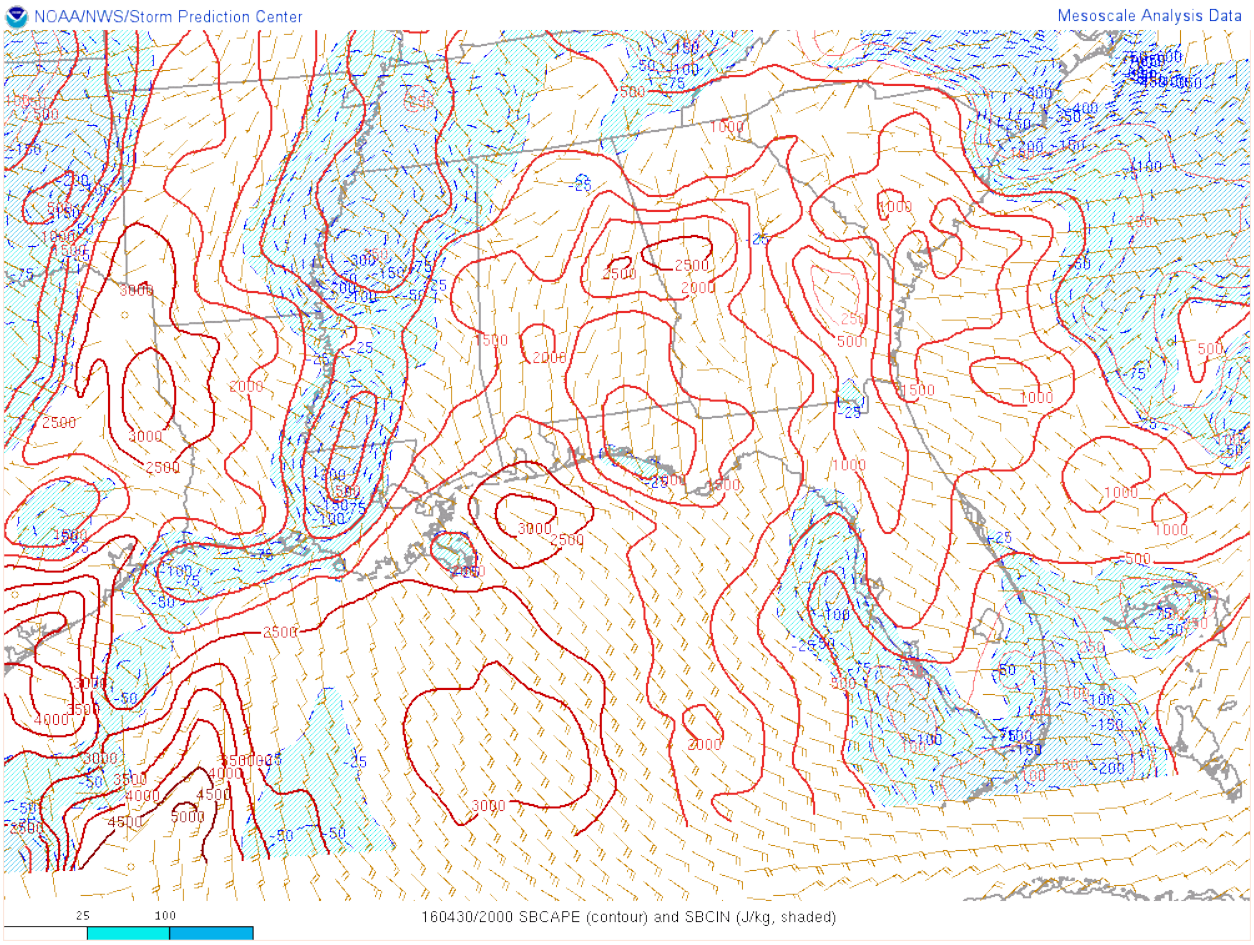

Fig. 36. As in Fig. 21 for 2000 UTC 30 April 2016.

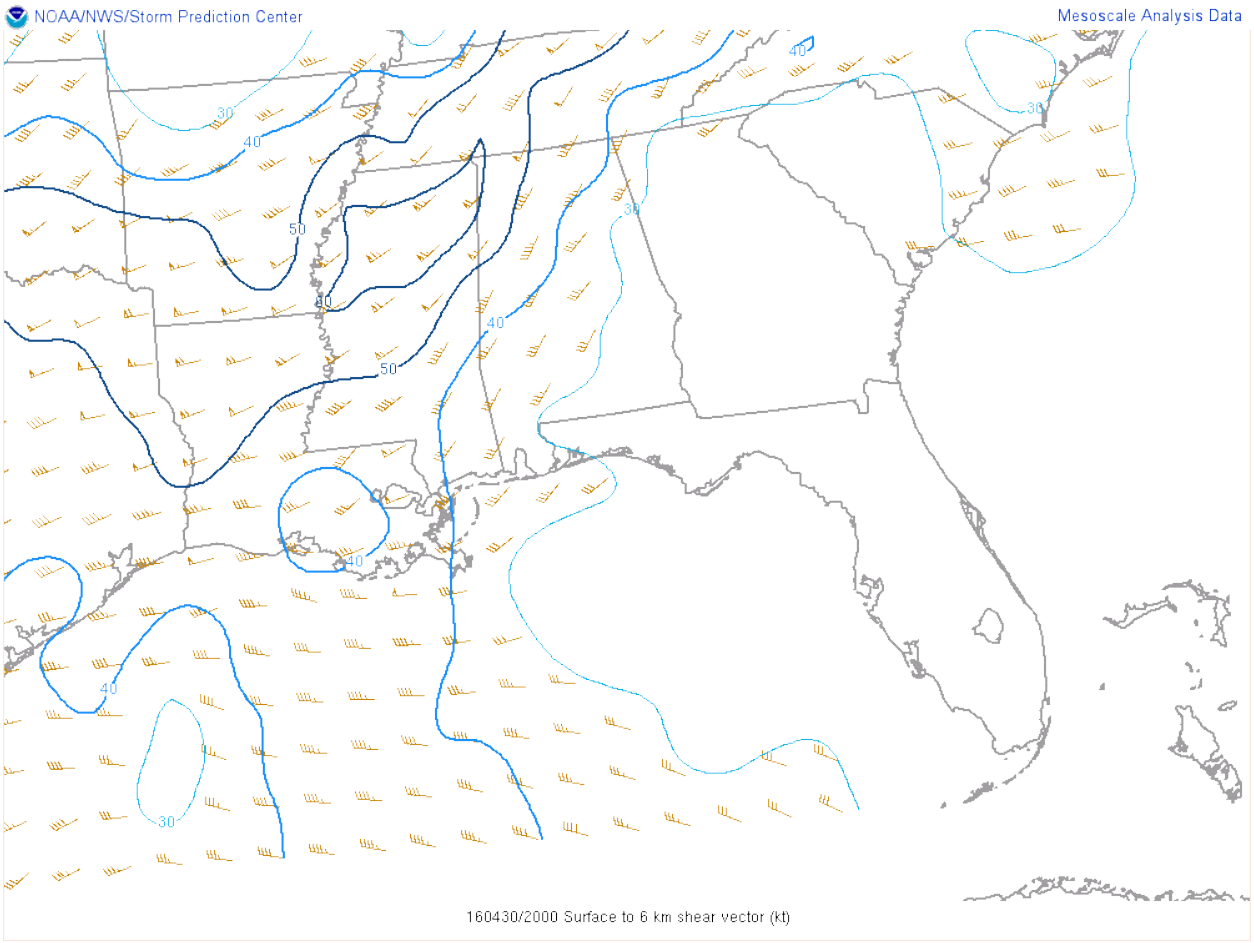

Fig. 37. Plotted are 0—6 km bulk wind shear barbs (in kt) and the magnitude of the 0—6 km wind shear (solid blue contours). Map is provided by SPC.

Fig. 38. As in Fig. 25, but for 2130 UTC 30 April 2016.

5. APPLICATIONS AND RESULTS

5.1 Determining the Parameters for the EWA and LSA

Now that IOPs were described, the application of the EWA and LSA to these cases will be discussed. There are several parameters in the EWA and the LSA that need to be determined, depending on the desired feature and data being used. For the EWA, there are several parameters that can be adjusted (*a*, *b*, δ, and saliency) as well as the smoothing technique and aggressiveness. Z_{DR} data can be noisy, especially when fewer pulses are uses to calculate Z_{DR}. 33 pulses are used to calculate the moments in radar data collected by UMass X-Pol, which is more than the WSR-88D radars product generator uses (8 or 16 pulses). Benefits of smoothing the data, which were discussed in section 3.1. Since the data are smoothed when mapped to a Cartesian grid and because UMass X-Pol uses a relatively high number of pulses per radial, we elected to use a weaker smoothing technique. δ can be adjusted to reduce the dynamic range in images, which is useful in reducing the number of spurious enhanced regions in data with poor spatial resolution (Lakshmanan et al. 2009). Z_{DR} column intensity typically ranges from 1 to 5 dB which is a very small dynamic range. Since high spatial resolution (Table 1) is being used and Z_{DR} has a small dynamic range, δ was left at a default value of 1 dB. As described in section 3.1, *b* is the upper bound used in the quantization step in the EWA. The decision-making for this variable is not discussed in Lakshmanan et al. (2009), but in the examples provided therein, this value is kept slightly below the expected maximum intensity, probably to increase the efficiency slightly by reducing the numbers of data structures that the EWA must iterate through. However, since we want to observe the maximum intensity in each Z_{DR} column, a value slightly above the

expected maximum is chosen: *b*=7 dB. This choice assures that we observe the maximum value in the Z_{DR} column.

The next variable, *a*, is a lower bound on Z_{DR} intensity. There are a few things to consider when determining which value of *a* is desirable. The objective definition of a Z_{DR} column has varied in previous research. While most literature refers to Z_{DR} columns as $Z_{DR} \geq 1$ dB, other values have been and can be used to identify them. Usually, Z_{DR} columns are bounded by a 1 dB contour (e.g. Kumjian et al. 2014, Snyder et al. 2015, Carlin et al. 2017), but they have also been identified using $Z_{DR} \geq 0.5$ dB (Van Den Broeke 2016) and $Z_{DR} \geq 1.5$ dB (Starzec et al. 2017) thresholds. Since there is no standardized definition of the lower bound of a Z_{DR} column, we must determine the lower bound that is best for our objectives, which are to produce high quality tracks of Z_{DR} columns, and to obtain useful information from those tracks. Additionally, changing *a* affects how the EWA identifies Z_{DR} column objects. Having a lower *a* allows smaller Z_{DR} column objects to combine into larger Z_{DR} column objects. An example of this is demonstrated in the circled area of Fig. 39a. Two smaller Z_{DR} columns are identified with *a*=2 dB in Fig. 39b while lowering *a* to 1 dB results in one larger Z_{DR} column object in Fig. 39c. The questions are, which is preferred, and which is closer to what would be perceived as a Z_{DR} column by a human?

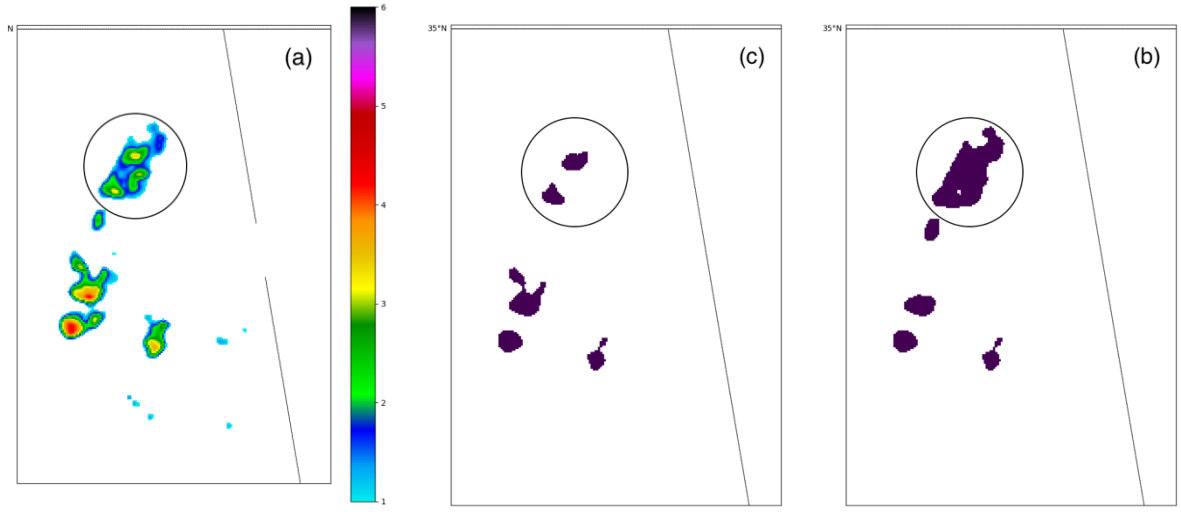

Fig. 39. This figure presents an example of how changing *a* can alter the way EWA identifies objects. Here, (a) is Z_{DR} (in dB), while (b) and (c) are Z_{DR} columns identified by the EWA where (b) has *a*=2 dB and (c) has *a*=1 dB.

The last parameter that needs to be determined is the saliency. Recall from section 3.1 that the saliency is a minimum areal extent threshold put on Z_{DR} column objects by the EWA. Van Den Broeke (2016) did a study on the polarimetric variability of classic supercell storms as a function of environment. Twelve supercells observed by WSR-88D were used in the analysis. While the focus of the study was on the variability of several polarimetric signatures in different environments, histograms of identified polarimetric signatures and select characteristics were produced. One histogram exhibited the areal extent of Z_{DR} columns identified 500 m above the 0 °C level (Fig. 40). Most of these Z_{DR} columns have areal extent between 20—80 km^2, though there are still a considerable number that are smaller. However, there are a few things to keep in mind. First, Van Den Broeke (2016) uses a 0.5 dB threshold to define the Z_{DR} column. This value is relatively low and would likely increase the number of gates associated with each identified Z_{DR} column and thus increase the average areal extent of the identified Z_{DR} columns. Also, Van Den Broeke only analyzed supercells, which typically have very strong updrafts and

as a result, have a higher likelihood of exhibiting a Z_{DR} column with larger areal extent. However, this guidance gives a good starting point of 20 km^2 or less for subjective testing.

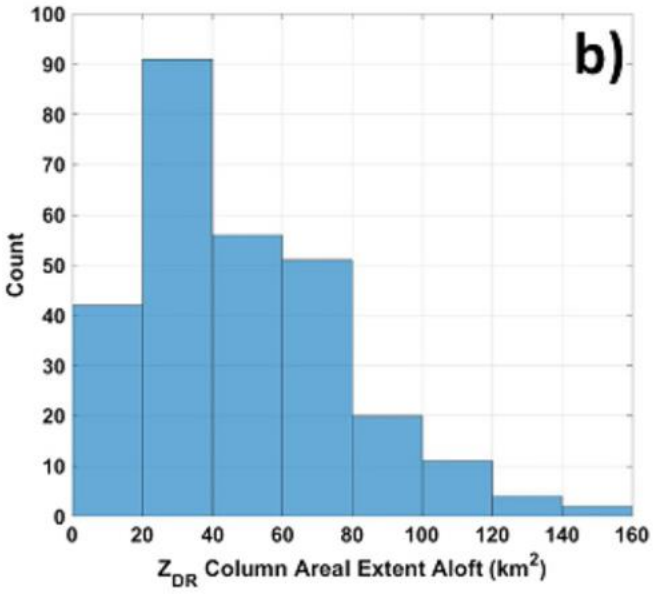

Fig. 40. This histogram from Van Den Broeke (2016) shows the variation of areal extent of Z_{DR} columns 500 m above the environmental 0 °C level observed in 12 supercell cases.

To determine the best *a* and saliency, some subjective testing needed to be done. The data for 5 April 2017 (IOP3b) was used to test for the best parameters, because it contained several convective modes. Testing was done by doing subjective identification of Z_{DR} columns and then manually drawing tracks between these Z_{DR} columns. These were compared to Z_{DR} column objects and tracks that were calculated by the EWA and LSA.

Four categories were created to categorize the Z_{DR} column objects identified by the EWA in comparison to the subjectively identified columns: hit, miss, false alarm, and "close". Hits are defined as Z_{DR} columns identified both subjectively and by the EWA (e.g. 3—11 in Fig. 41). Misses are Z_{DR} columns identified subjectively but not by the EWA. False alarms are Z_{DR} column objects identified by the EWA but not subjectively (e.g. circled columns in Fig. 41).

"Close" columns are defined as EWA columns that are substantially too small (e.g. 1 and 2 in Fig. 41) or too large, usually encompassing multiple subjectively identified columns. This method can used to characterize each combination of *a* and saliency.

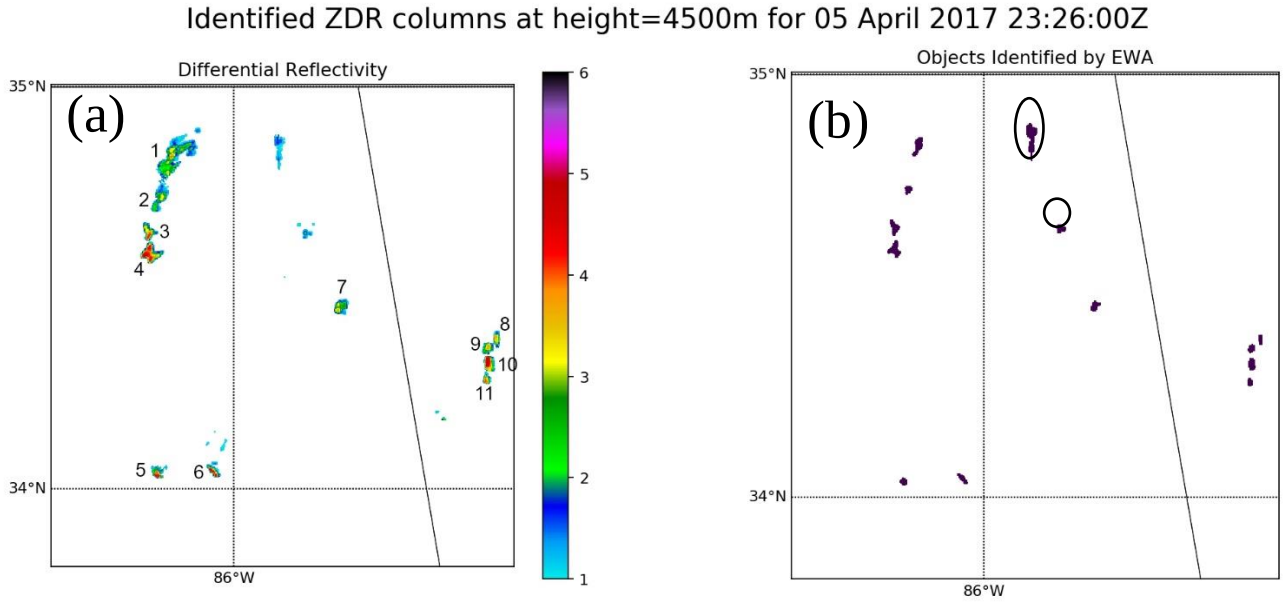

Fig. 41. (a) A constant altitude PPI (CAPPI) of Z_{DR} at 4500 m AGL with numbered annotations next to enhanced regions of Z_{DR} that was subjectively identified as a Z_{DR} column. (b) An example of Z_{DR} column objects produced by the EWA. 1 and 2 are considered "close", 3—11 are "hits", and the two circled Z_{DR} column objects are "false alarms".

Testing was done using various combinations of *a* and saliency. A few different saliency values were first surveyed between 1—20 km^2 to give the author a general idea of what range of saliencies to more closely analyze with the technique described above. That range was determined to be 2—5 km^2 for a=1 dB and a=2 dB with the results displayed in Table 3 and Table 4. When a=2 dB, false alarms are non-existent, which makes sense given the higher minimum threshold. However, there is a sizeable number of misses, especially with increasing saliency, and as expected, a lower number of hits with increasing saliency. The EWA does not identify a lot of the very small areas of enhanced Z_{DR} when the saliency is larger. "Close" columns decrease with increasing saliency, though not significantly between 3—5km^2. Z_{DR}

columns that are considered close are undesirable, more so than missed Z_{DR} columns. This is because they are misrepresentative of the data and often result in a larger number of errors in the tracks. The same can be said about false alarms, which are identified Z_{DR} columns that a human would not perceive to be there. Two other categories are introduced in these tables: POD and POFD. Probability of detection (POD) is used here to display the probability of the EWA identifying a good column and is defined as:

$$POD = \frac{Hits}{Total\ Possible\ \#\ of\ Columns} \tag{9}$$

where the denominator is defined by the number of columns that were subjectively analyzed. Probability of false detection (POFD) used in this thesis is slightly different than the conventional definition. Here, it is defined as:

$$POFD = \frac{Close + False\ Alarms}{Hits + Close + False\ Alarms} \tag{10}$$

POFD is the percentage of columns identified by the EWA that are undesirable and/or unrepresentative. To obtain the highest quality objectively identified Z_{DR} column objects and their tracks, we want to minimize POFD without reducing POD too much.

Table 3. Testing categories for EWA with *a*=2 dB.

Saliency (km^2)	**2**	**3**	**4**	**5**
False Alarms	1	0	0	0
Misses	115	134	168	181
Hits	178	161	146	132
Close	46	30	25	19
POD	0.511	0.463	0.420	0.379
POFD	0.209	0.157	0.146	0.126

Table 4. As in Table 3 for *a*=1 dB.

Saliency (km^2)	**2**	**3**	**4**	**5**
False Alarms	34	17	8	7
Misses	21	33	45	58
Hits	220	215	211	202
Close	82	63	67	56
POD	0.632	0.618	0.606	0.580
POFD	0.345	0.271	0.262	0.238

Z_{DR} column objects with *a*=2 dB had higher POD and lower POFD than Z_{DR} column objects with *a*=1 dB. For both *a*=1 dB and *a*=2 dB, POD and POFD decreased with increasing saliency. It is difficult to determine the best balance between POD and POFD by just looking at the numbers between columns that are subjectively identified, and columns identified by the EWA. In general, though, we considered it more important to reduce POFD than it is to increase POD.

Instead, it was best to analyze the tracks that were created using the same combination of *a* and saliency. Since the performance of the LSA is dependent on the identification technique and thus the parameters of the EWA, it is essential to evaluate how changing these parameters affects the quality of the Z_{DR} column tracks. Recall from section 3.2 that one of the criteria used to evaluate tracks is their duration (Lakshmanan and Smith 2010). A higher average duration is associated with fewer dropped associations of Z_{DR} column objects across time. The average duration for tracks in 5 April 2017 was generally lower for *a*=1 dB than *a*=2 dB (Table 5, Table 6), which shows that there are typically less dropped associations when *a*=2 dB instead *a*=1 dB. Another way to evaluate the number of dropped associations is by looking at the average numbers of columns per track. This is a way to normalize the analysis since the time between scans was not constant throughout the IOP. Either way, using *a*=2 dB reduces the number of

dropped associations, especially for saliencies of 3—5 km^2. For saliencies between 3—5 km^2, the average duration is approximately 100—150 seconds better and about 1 column per track better.

Table 5. Testing categories for the LSA with *a*=1 dB.

Saliency (km^2)	**2**	**3**	**4**	**5**
Z_{DR} columns	381	328	304	276
Tracks	74	63	60	53
Average # of Z_{DR} Columns per Track	5.14	5.21	5.07	5.21
Average Duration (s)	885	942	888	939
Average Duration (min)	14.75	15.70	14.80	15.65

Table 6. As in Table 5 for *a*=2 dB.

Saliency (km^2)	**2**	**3**	**4**	**5**
Z_{DR} Columns	263	221	181	159
Tracks	46	36	30	25
Average # of Z_{DR} Columns per Track	5.72	6.14	6.03	6.36
Average Duration (s)	921	1034	1041	1046
Average Duration (min)	15.35	17.23	17.35	17.43

Additionally, tracks produced by the LSA were compared to manually drawn tracks. For both *a*=1 dB and *a*=2 dB, differences between saliencies were visually compared on a track-by-track basis (e.g. Fig. 42). Visual inspection showed that tracks with *a*=2 dB were better than across the board than tracks with *a*=1 dB (e.g. Fig. 42), which is also supported by the data in Table 5 and Table 6. Having a lower bound of 2 dB is higher than what has been used to identify Z_{DR} columns in previous research (e.g. Kumjian et al. 2014; Snyder et al. 2015; Starzec et al. 2017; Carmin et al. 2017). It can result in Z_{DR} columns with lower Z_{DR} values not being identified by the EWA. However, using *a*=2 dB increases the trackability of the identified Z_{DR} column objects and improves the quality of the tracks that are produced (e.g. Fig. 42). Primarily

for this reason, a=2 dB is used in the EWA for the IOPs analyzed in this research. For saliency, using 2 km^2 was notably degraded track quality, but little difference was observed for tracks with a saliency of 3—5 km^2. This observation was also supported by average track duration for each saliency (Table 6). Since there were not any significant differences between 3—5 km^2, 3 km^2 was chosen to increase the number of Z_{DR} column objects and tracks identified without decreasing the quality of the tracks.

Lakshmanan and Smith (2010) also quantified two other parameters that can used to evaluate the tracks being produced by a tracking algorithm. The standard deviation (σ) of a specific characteristic (e.g. areal extent of Z_{DR} column) can be used to track the variability of the Z_{DR} column over time (i.e. along a track). In our case, σ can be used to evaluate Z_{DR} column characteristics like areal extent, height about the 0 °C level, and peak Z_{DR} intensity. The idea is that σ will be lower when there are less mismatches (as in Fig. 12c). Also, the root-mean-square error (RMSE) of the centroid positions from their optimal line fit can be used to evaluate the linearity of the track. RMSE will be lower for tracks with fewer jumps (as in Fig. 12d). Neither of these parameters are used to evaluate tracks in this study but are recommended for future relatable studies.

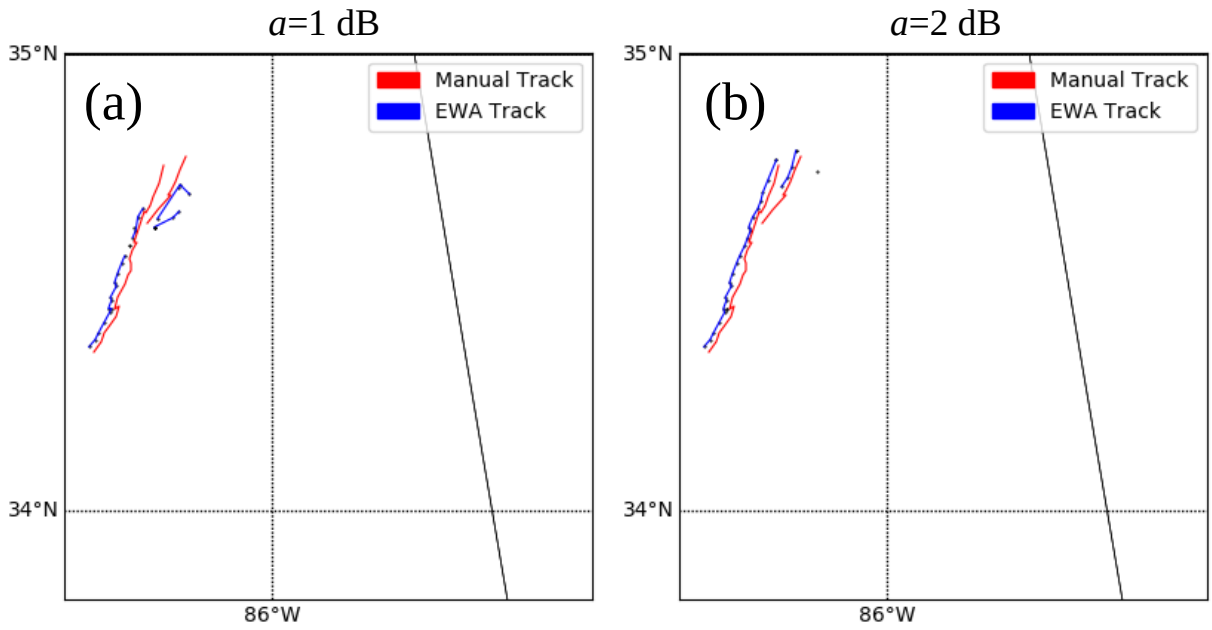

Fig. 42. Both images show an example of tracks being compared between manually drawn tracks (red) and EWA/NEW-produced tracks (blue). Both are using saliencies of 4 km^2 and search radii multiplied by two with (a) a=1 dB and (b) a=2 dB. The tracks produced when a=2 dB are clearly a better match to the manually identified tracks.

Another parameter than can be adjusted in the LSA is the search radius after Z_{DR} column objects are projected forward. Since the search radius is dependent on the size and motion of the object relative to the volume update time, the search radius can be very small when tracking Z_{DR} columns. We found that increasing the search radius by a multiple of two improved the tracks.

5.2 5 April 2017: IOP3b (2017)

The first case study to which we applied the EWA and LSA is that of 5 April 2017, or IOP3b in the 2017 VORTEX-SE field project. IOP3b is the IOP used to determine the EWA and LSA parameters as described in section 5.1, so many of the characteristics of the tracks have already been discussed (Table 6). A few examples of Z_{DR} column tracks are shown in Fig. 43. When data collection began at 2044 UTC, storms were isolated, which allowed the radar

operator to focus small sector scans on the isolated storms, greatly increasing the temporal resolution to as high as 1-minute volume updates. Increasing the temporal resolution of radar observations increases the chance of producing longer and higher quality tracks. It allows the entire storm evolution to be observed, making it easier for the LSA to match Z_{DR} column objects across time. Increase of storm coverage began around 2230 UTC, which is about when the radar operator switched to a full volume coverage pattern, degrading the temporal resolution to 4—6 minutes, closer to that of the WSR-88D. One of the objectives for the 2017 VORTEX-SE project was to obtain multi-Doppler observations of storms, and UMass X-Pol was not tailored to automatically sync with other radars' volume coverage timing. Because of this, much of the data obtained during IOP3b has lower temporal resolution than what is desired (~1—2 minutes or less). Additionally, an unknown error caused the UMass X-Pol to occasionally repeat elevation scans, resulting in increased volume update times during full 360° PPI scans. Though the tracks were still mostly reasonable (Fig. 43c and Fig. 43d), there were more dropped associations in tracks with the increased volume update times.

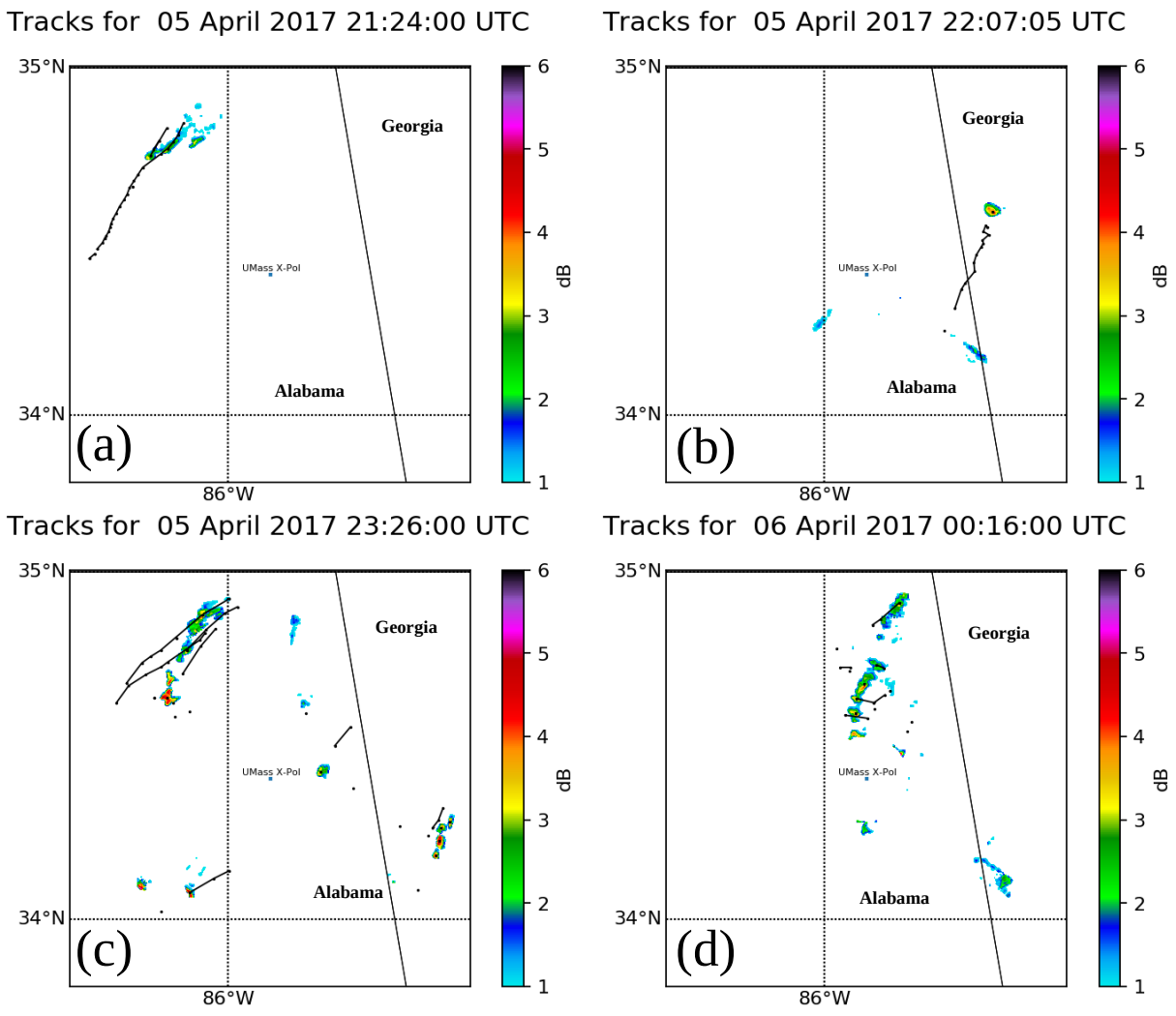

Fig. 43.Tracks produced by the LSA (solid black lines), centers of columns identified by EWA (black dots), and Z_{DR} (in dB) at (a) 2124 UTC, (b) 2207 UTC, (c) 2326 UTC, and (d) 0016 UTC.

Time series analyses of areal extent, height above the 0 °C level, and peak Z_{DR} value of each Z_{DR} column across time are shown in Fig. 44. Notably, values observed here are consistent with what has been seen in past literature. Van Den Broeke (2016) showed that Z_{DR} column extent can be as large as 140—160 km^2 and maximum altitude of Z_{DR} column can extent as high as 8.5 km AGL. The case presented in Snyder et al (2015) had a Z_{DR} column extending as high as 5 km above the 0 °C level. Of interest is how these characteristics evolve with time, and it is

clear that a lot of variation can occur on a small timescale, which is shown in all three plots in Fig. 44. For example, there were two isolated storms that were observed early on in the IOP between 2030—2210 UTC. Both of the Z_{DR} columns in these storms exhibited rapid changes in each of the observed characteristics. Though not the focus of this study, the characteristics of each of the Z_{DR} columns could be studied to determine what are the underlying processes causing these changes and how they are related to the evolution of the updraft itself.

A shift in the convective mode is clearly discerned around 2300 UTC with the increase in number of tracks. As mentioned, the earlier parts of the IOP are described by isolated cells before transitioning into widespread convection in the latter part of the IOP.

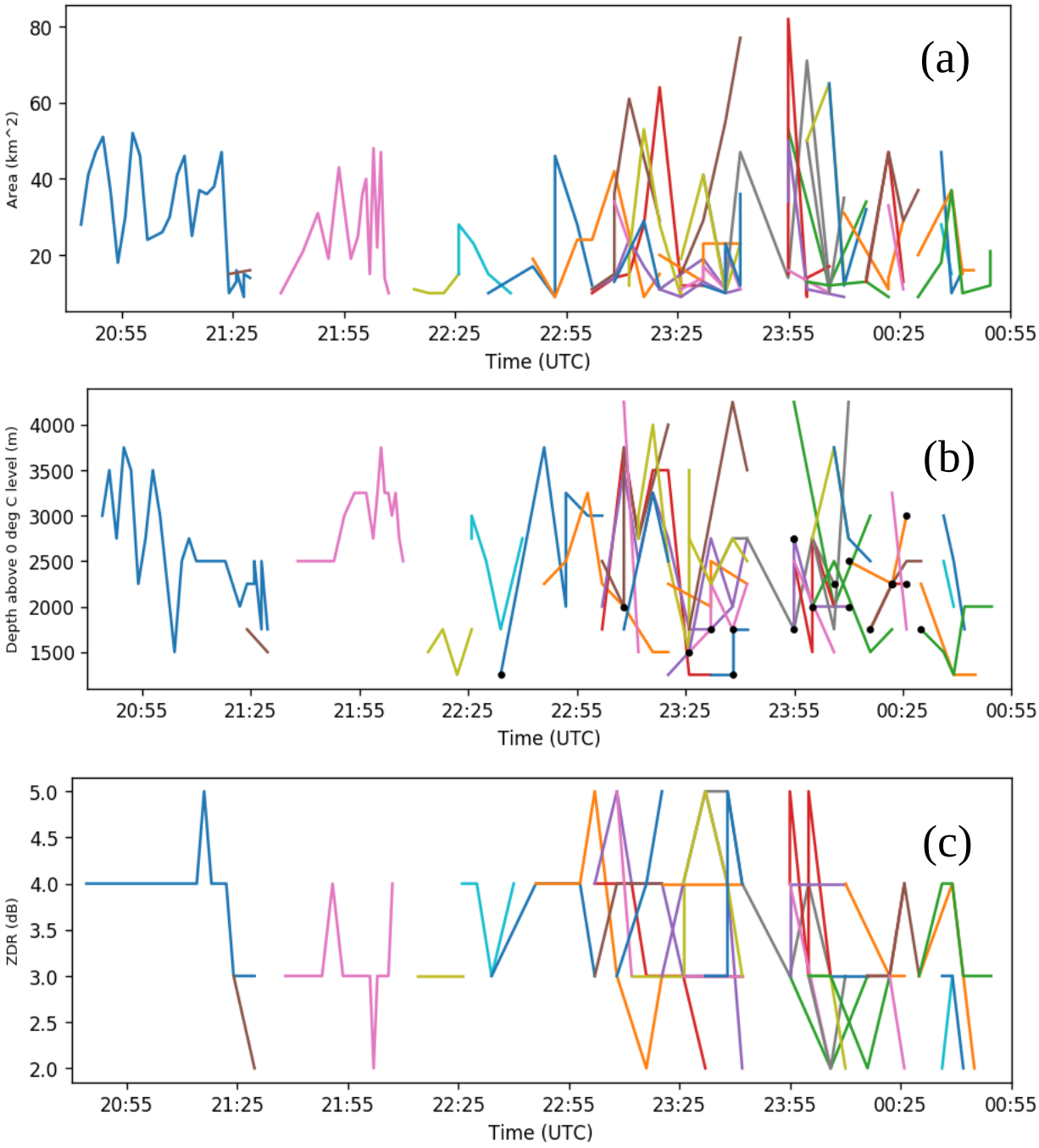

Fig. 44. (a) Areal extent, (b) height above the 0 °C level, and (c) maximum Z_{DR} value for tracked Z_{DR} columns (each a different color) observed during IOP3b (2017). Black dots represent centroids of Z_{DR} columns within 25 km^2 of the radar location and possibly capped by the cone of silence.

5.3 27 March 2017: IOP1b (2017)

IOP1b from 2017 VORTEX-SE is the largest dataset that the EWA and LSA are applied to (Table 7) with over 200 volumes containing convective storms and largest number of Z_{DR} column objects and tracks. The average number of columns per track are similar to IOP3b from 2017, though the average duration of each track is significantly diminished in comparison to IOP3b from 2017 (Table 7).

Table 7. As in Table 5 for 27 March 2017 without the variation in saliency.

Z_{DR} columns	862
Tracks	143
Average Number of Z_{DR} Columns per Track	6.03
Average Duration (s)	647
Average Duration (min)	10.78

A few example tracks are provided in Fig. 45. Fairly widespread coverage of Z_{DR} columns persists throughout the IOP, with a variety of convective modes present. This IOP is characterized by two rounds of storms. The first round of storms, occurring between 1900—2200 UTC consisted of scattered convection with a few embedded supercells propagating northeastward through the domain. After a two-hour break in storm coverage, a QLCS propagated from Tennessee southeastward into Alabama (0000—0400 UTC on 28 March 2017), though it can be seen that individual Z_{DR} columns were mostly moving eastward, as indicated by the tracks in (Fig. 45c, d).

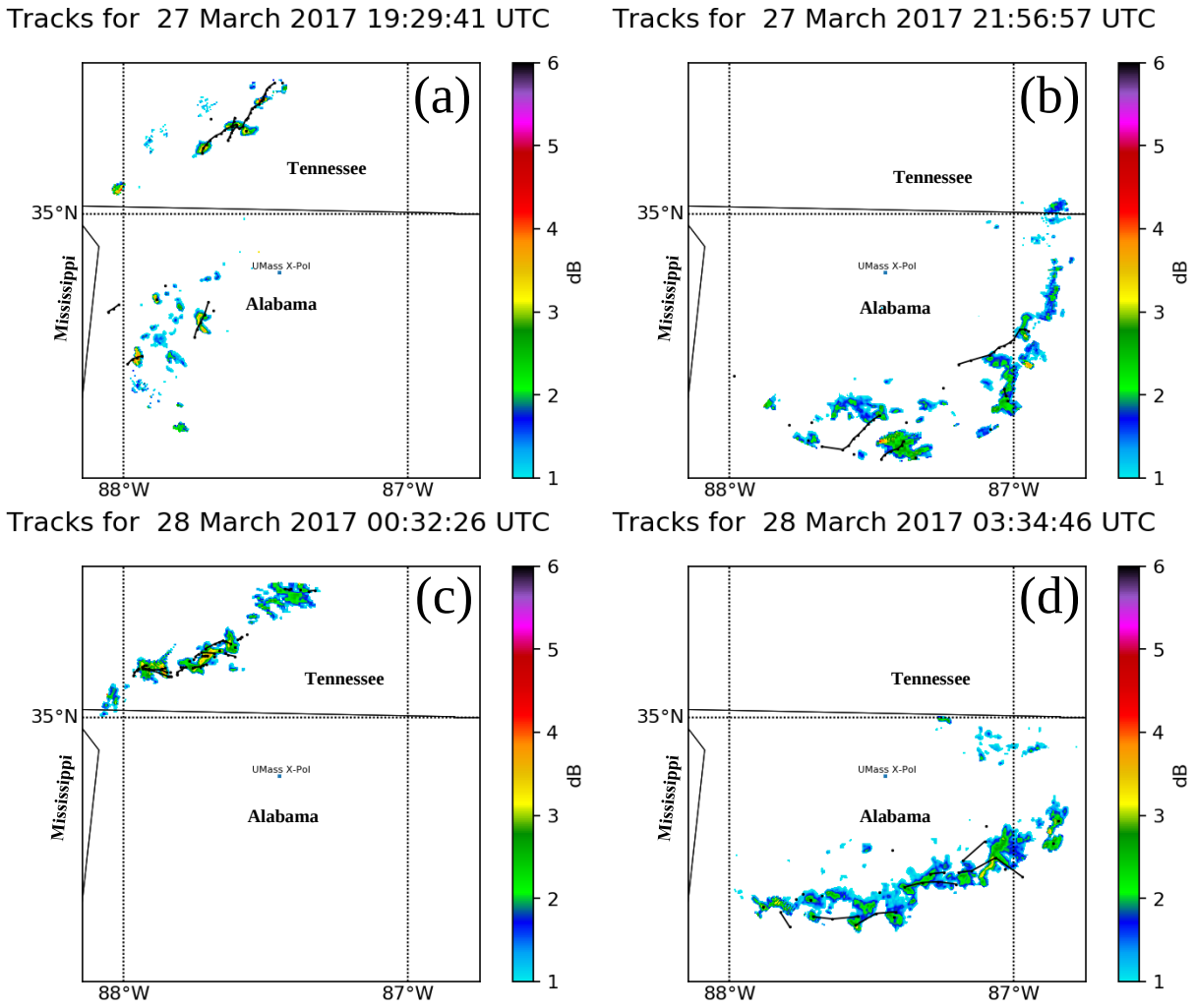

Fig. 45. As in Fig. 43 for (a) 1929 UTC, (b) 2157 UTC, 27 March 2017 and (c) 0032 UTC, (d) 0335 UTC, 28 March 2017.

As with IOP3b, time series of Z_{DR} column characteristics were created (Fig. 46). In addition to a gap between 2200—0000 UTC mentioned before, there are two other gaps: one at 2010—2030 UTC due to a generator failure and the second at 0200—0245 UTC due to significant precipitation over the radar causing substantial differential attenuation (Fig. 46).

Though there were a wide variety of areal extents observed with the identified columns, the majority stayed under 50 km^2. A few Z_{DR} columns reached maximum areal extents of almost 200 km^2. One Z_{DR} column reached an areal extent of 400 km^2 (Fig. 46a), likely a result of

multiple Z_{DR} columns being combined into one. The convective mode of scattered storms in the first round appear to have lower areal extents and less variability in general, especially between 1910—2000 UTC. The height of Z_{DR} columns was more variable, but generally stayed between 1500—3500 m above the 0 °C level. Maximum Z_{DR} values were low compared to IOP3b. Only one Z_{DR} column had a max Z_{DR} of 5 dB briefly, and most Z_{DR} columns had a max value of 2—3 dB, which was not the case for IOP3b; most Z_{DR} columns in IOP3b had max Z_{DR} values of 3—4 dB. In the second round of storms, max Z_{DR} are noticeably lower after the storms passed over the radar. This observation is consistent with the general weakening trend of the QLCS as it progressed southeastward into the state.

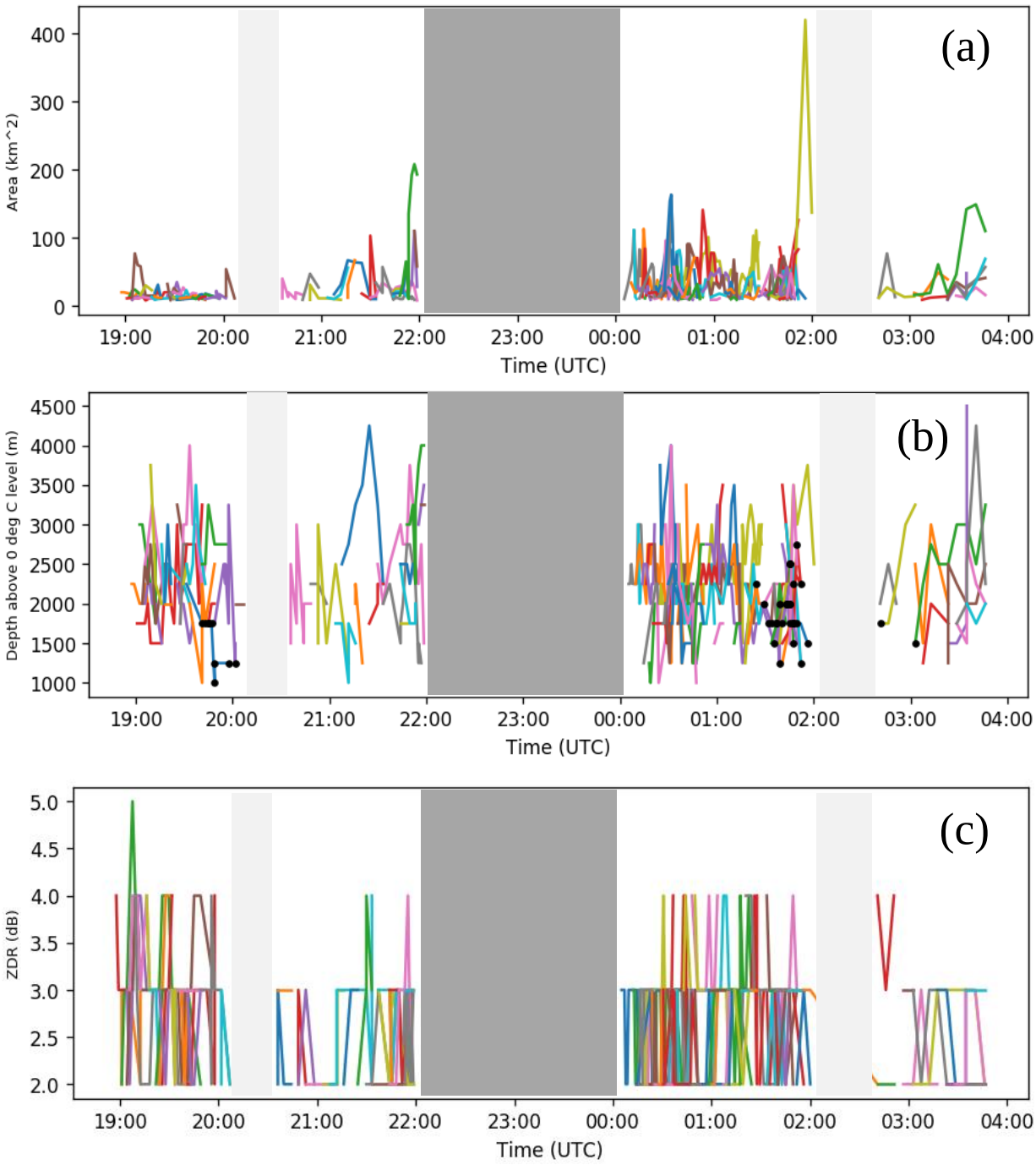

Fig. 46. As in Fig. 44 for the entirety of IOP1b (2017). The light grey areas are dropouts in data. The dark grey area represents a period in which there were no storms.

5.4 31 March 2016: IOP3 (2016)

The dataset available to us for IOP3 in 2016 has a much smaller overall duration of about an hour. There are a sizable number of Z_{DR} column objects (Table 8) but the average number of Z_{DR} columns per track is noticeably less than the previous two IOPs discussed, which is not the case for the average duration. The average number of Z_{DR} columns per track is likely lower because the volume coverage pattern was only full 360° PPI scans instead of smaller sectors that were sometimes employed in the previous two IOPs.

Table 8. As in Table 7 for 31 March 2016.

Z_{DR} Columns	257
Tracks	48
Average Number of Z_{DR} Columns per Track	5.04
Average Duration (s)	843
Average Duration (min)	14.05

Since the time frame for this IOP is much lower, only one figure is provided to display a few example tracks (Fig. 47). Scattered storms with a few weak supercells propagated northeasterly through the domain, exemplified by the tracks.

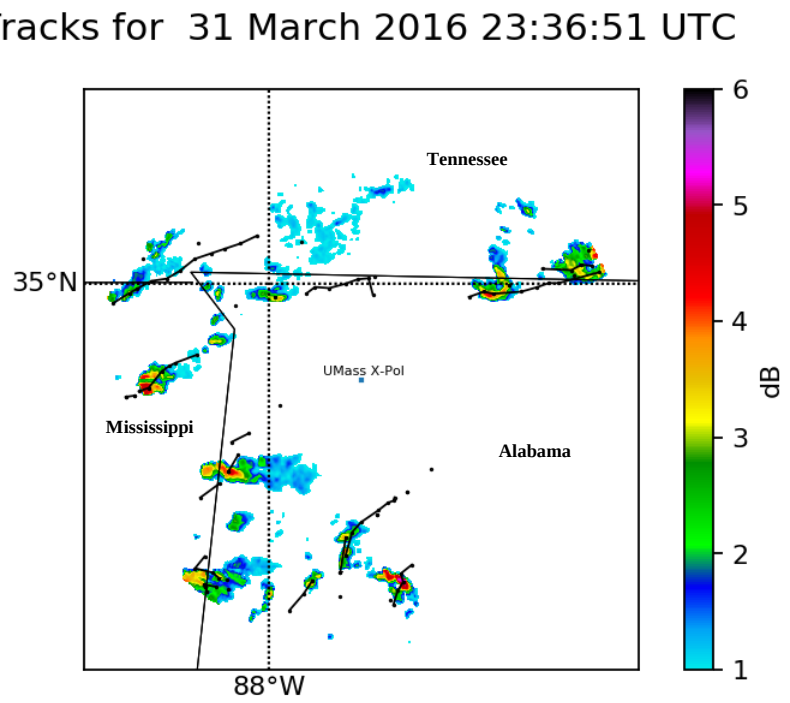

Fig. 47. As in Fig. 43, but for 2337 UTC on 31 March 2016.

Time series plots of Z_{DR} column areal extent and intensity are also provided in Fig. 48. Z_{DR} column depth is not provided owing to suspicious results. Many columns were topping out the gridded radar data at 5000 m above 0 °C level. As in IOP1b from 2017, one Z_{DR} column has very large areal extent (> 400 km^2), while the rest cover 200 km^2 or less (Fig. 48a). Maximum Z_{DR} values vary greatly over the IOP period, ranging between 2 and 4 dB, with a few exceeding 4 dB (Fig. 48b).

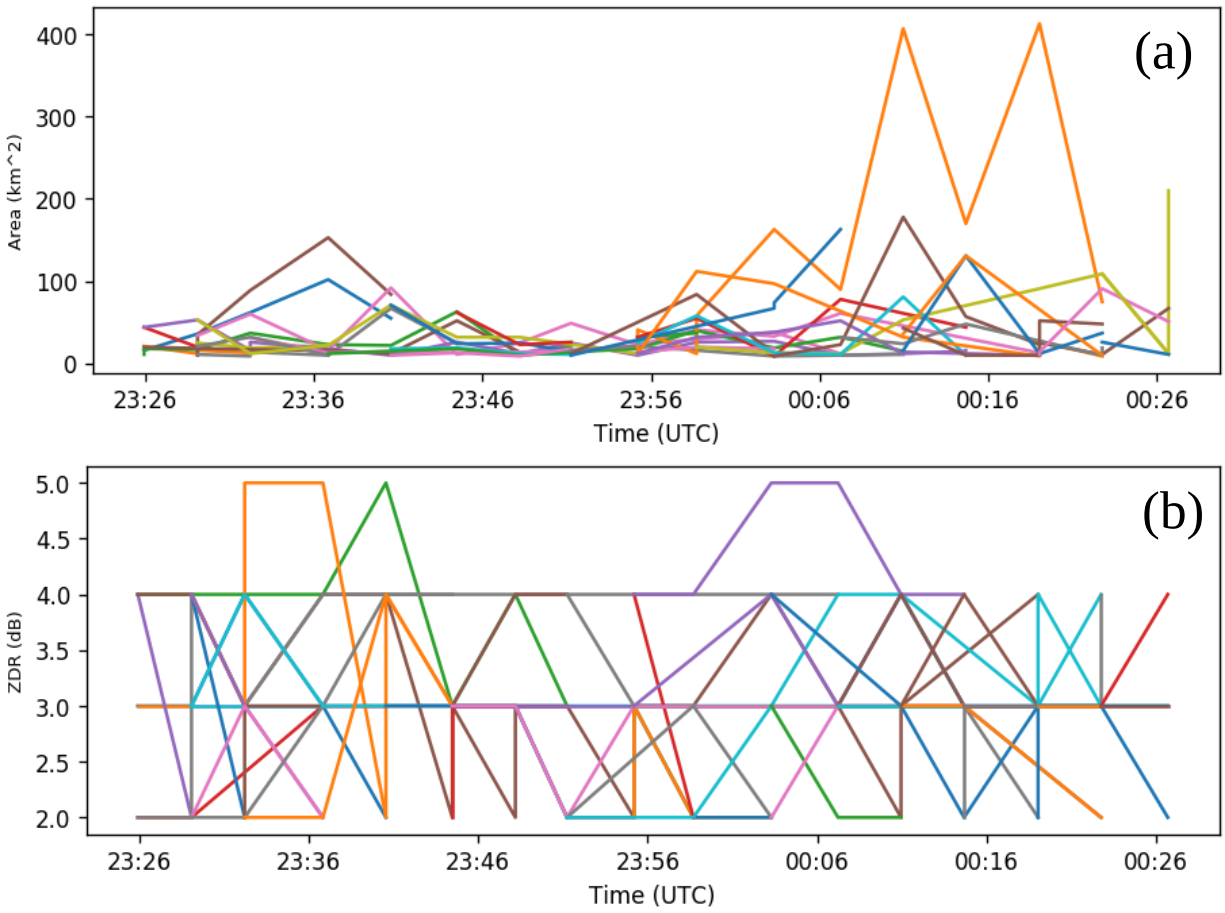

Fig. 48. As in Fig. 44 for 2325—0030 UTC.

5.5 30 April 2016: IOP4c (2016)

IOP4c from 2016 is the last analyzed case study, with by far the least number of Z_{DR} columns and tracks. The average number of columns per track and average duration are similar to IOP3 from 2016, during which UMass X-Pol used a similar volume coverage pattern (Table 9). This IOP was relatively short (~1900 — 2300 UTC, or about 4 hrs) compared to IOP3b and IOP1b from 2017, therefore, only one figure is provided for example tracks identified during this IOP (Fig. 49). Time series analyses are also provided in Fig.50. The storms comprising the event were significantly weaker overall than those in the other three IOPs. This trend is reflected in the

Z_{DR} column characteristics and the small number of Z_{DR} columns (Table 9). On this day, severe weather parameters were not as conducive for severe weather as the other case studies. For example. While analyzed SBCAPE exceeded 2000 J kg^{-1} in some areas, these values diminished to less than 1000 J kg^{-1} near the Alabama-Tennessee border (Fig. 36). Additionally, 0—6 km bulk shear generally ranged between 40—60 kts, with the highest values near towards northwestern Alabama (Fig. 37). The areas of peak SBCAPE and 0—6 km bulk shear were not collocated. The SPC's convective thunderstorm outlook for this day only had a slight risk (Fig. 35), and there weren't many severe weather reports (72 nationwide, 2 in Alabama). Because of this, it makes sense that the observed Z_{DR} columns had lower intensities.

Table 9. As in Table 7 for 30 April 2016.

Z_{DR} Columns	92
Tracks	18
Average Number of Z_{DR} Columns per Track	5.1
Average Duration (s)	711
Average Duration (min)	11.85

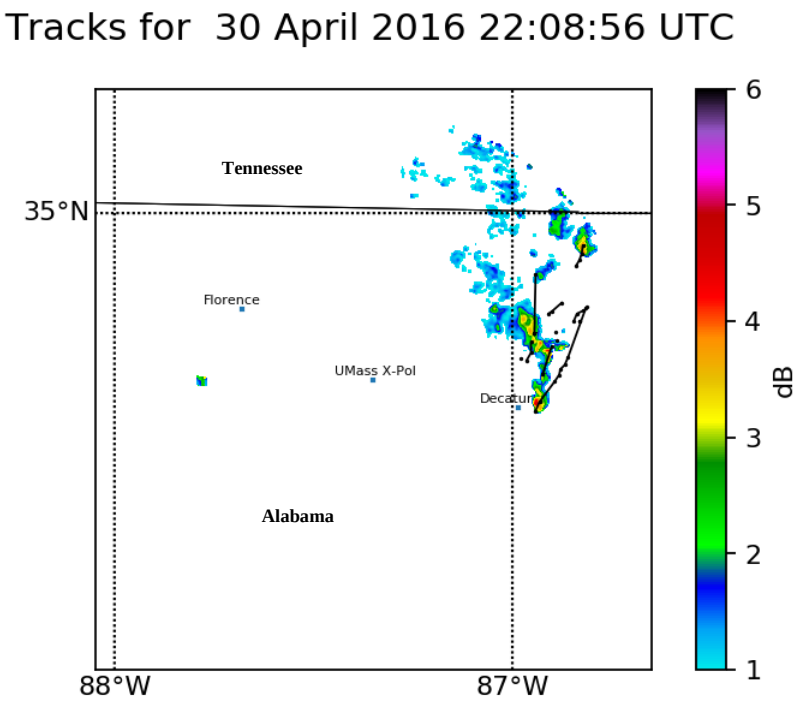

Fig. 49. As in Fig. 43, but for 2209 UTC on 30 April 2016.

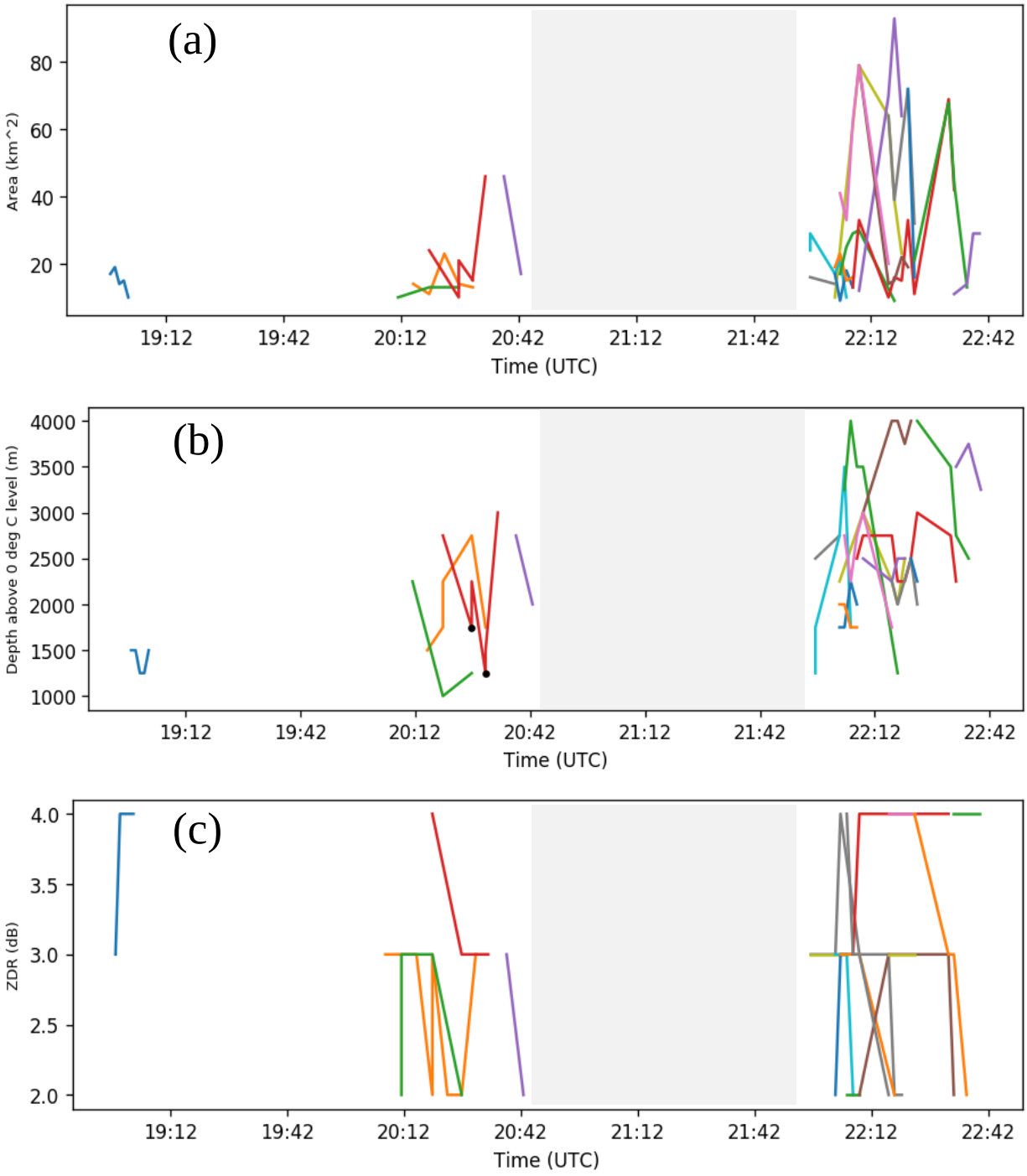

Fig. 50. As in Fig. 44, but for 1900—2240 UTC. The light grey area is a dropout in data due to precipitation over the radar causing significant differential attenuation.

5.6 Comparisons with the KHTX WSR-88D

It was desirable to make comparisons of UMass X-Pol CAPPIs of Z_{DR} columns with similar plots from a WSR-88D to illustrate the advantage of analyzing Z_{DR} columns in radar data with higher spatial and temporal resolution (Fig. 51). 10 volumes were observed by UMass X-Pol between 2157—2207 UTC on 05 April 2017 (Fig. 51a). During approximately the same period, KHTX only had three volumes (Fig. 51b). The KHTX Z_{DR} observations are noisier because fewer pulses (8 or 16) were used to calculate Z_{DR} than are used by UMass X-Pol (33). In addition, the WSR-88D resolution is coarser both spatially and temporally (Table 10).

The EWA was also applied to KHTX data for a small portion of IOP3b from 2017 (Fig. 52). Since WSR-88D only uses 8 pulses to calculate the moments (in comparison to 33 for UMass X-Pol) we used a Gaussian filter of σ=3 instead of σ=1. This helps to smooth the noisier Z_{DR} data. For the particular Z_{DR} column observed in Fig. 52, the lower bound had to be lowered to a=1 dB from a=2 dB that is used for UMass X-Pol. With a=2 dB, the Z_{DR} column is clearly identified in the two timeframes but is not visible in the third frame. This may be due to the enhanced Z_{DR} being smoothed out, which is not ideal but is possible when a more aggressive smoothing technique is used. The LSA was also applied to the KHTX observations with the exact domain observed by the UMass X-Pol and a similar timeframe (approximately 2000—0100 UTC), with statistics of those tracks provided in Table 11. Surprisingly, the average duration and number of Z_{DR} columns per track are comparable to the algorithms applied to UMass X-Pol data.

Admittedly, significantly less effort was put into determining the parameters for the WSR-88D data due to time constraints. Because of this, the results in this section (5.6) are extremely preliminary and future efforts need to be made to further evaluate these algorithms

being applied to WSR-88D data. For future work involving these algorithms on WSR-88D data, the same process from chapter 5.1 in determining the parameters should be applied. It is apparent that even for the same variable (i.e. Z_{DR}), parameters of the EWA and LSA need to be optimized for the dataset that is being used.

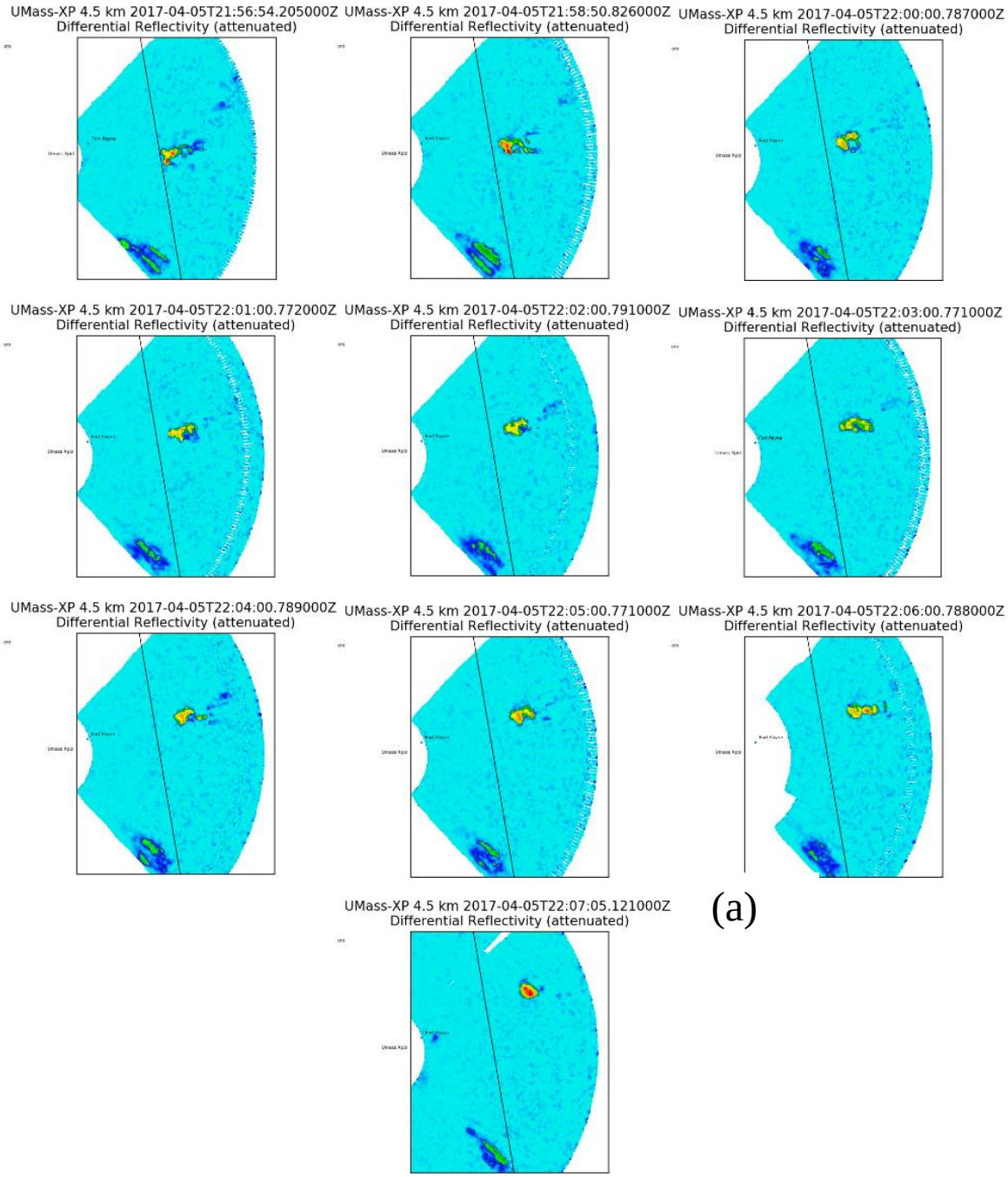

(a)

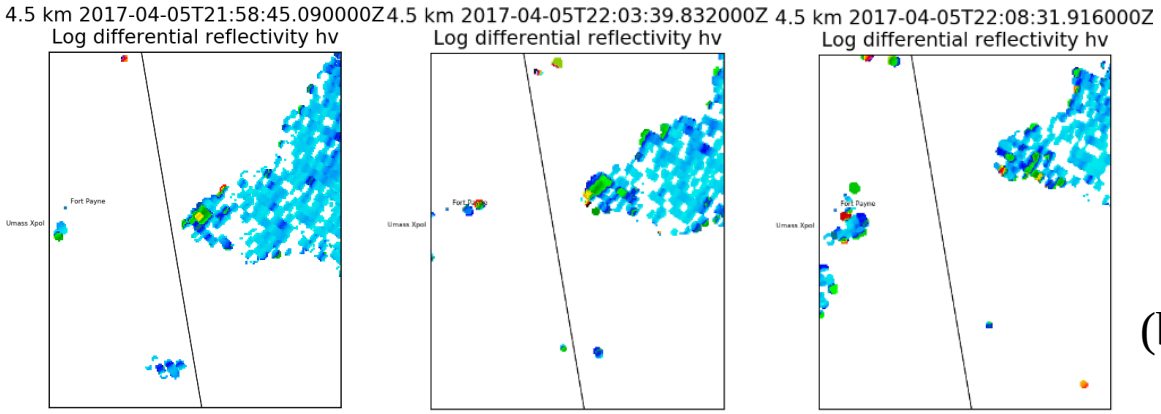

(b)

Fig. 51. CAPPIs of Z_{DR} at 4.5 km AGL from (a) UMass X-Pol from 2157 to 2207 UTC on 05 April 2017 and from (b) KHTX from 2159 to 2208 UTC on 05 April 2017. Each image uses an identical domain.

Table 10. Comparison of select attributes between UMass X-Pol and WSR-88D.

Attribute	**UMass X-Pol**	**WSR-88D**
Half-power beam width	1.2°	1.0°
Range resolution	60 m	1 km
Wavelength	3 cm	10 cm
Max unambiguous range	60 km	231 km
Max azimuthal scan rate	24° s^{-1}	30° s^{-1}

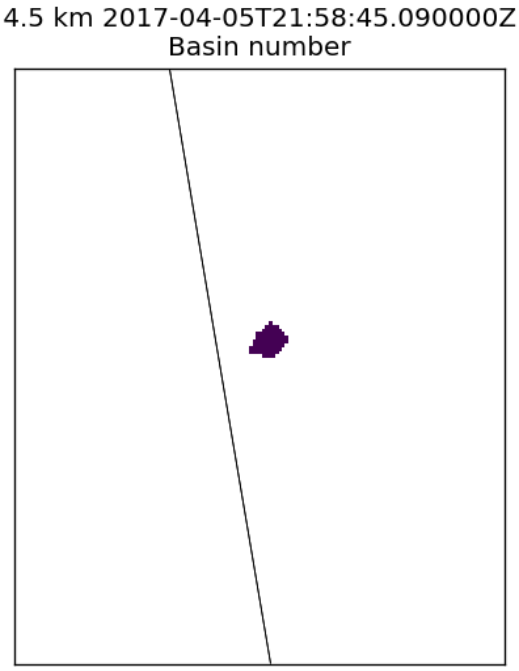
4.5 km 2017-04-05T21:58:45.090000Z
Basin number

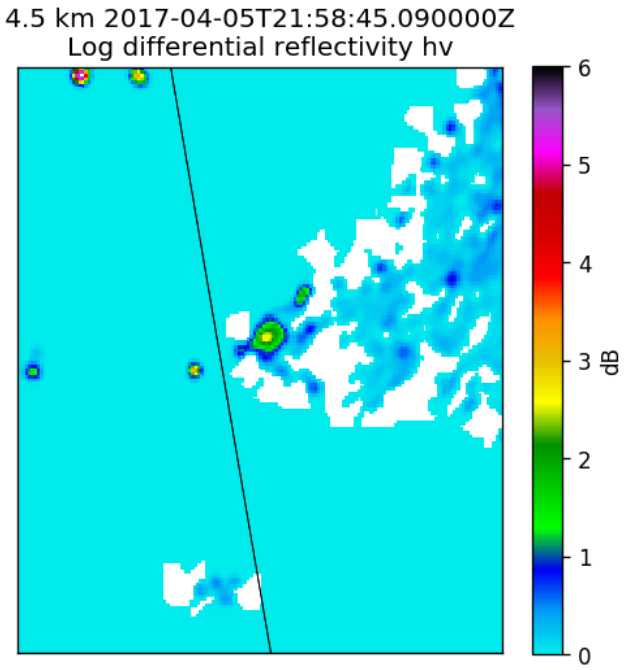
4.5 km 2017-04-05T21:58:45.090000Z
Log differential reflectivity hv
6
5
4
3
2
1
0
dB

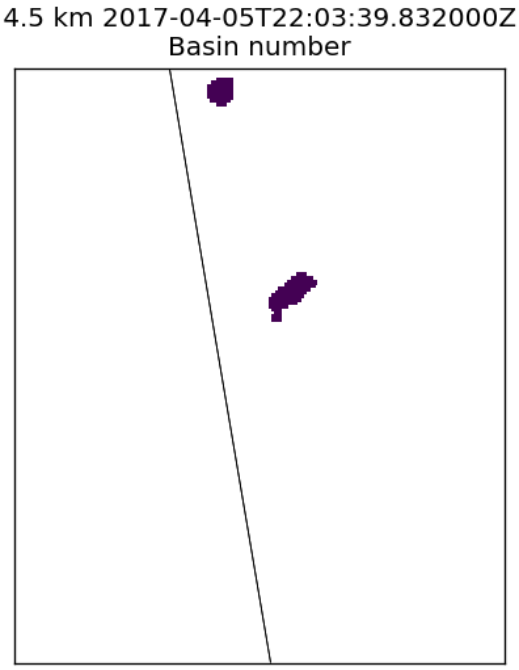
4.5 km 2017-04-05T22:03:39.832000Z
Basin number

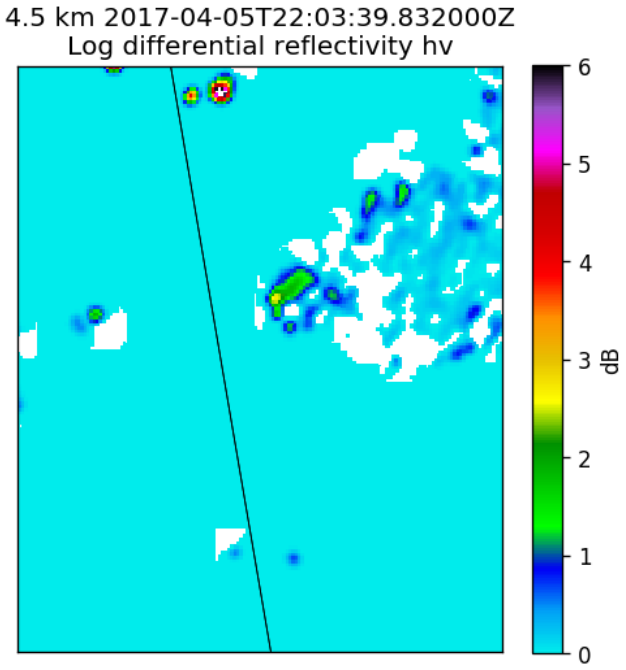
4.5 km 2017-04-05T22:03:39.832000Z
Log differential reflectivity hv
6
5
4
3
2
1
0
dB

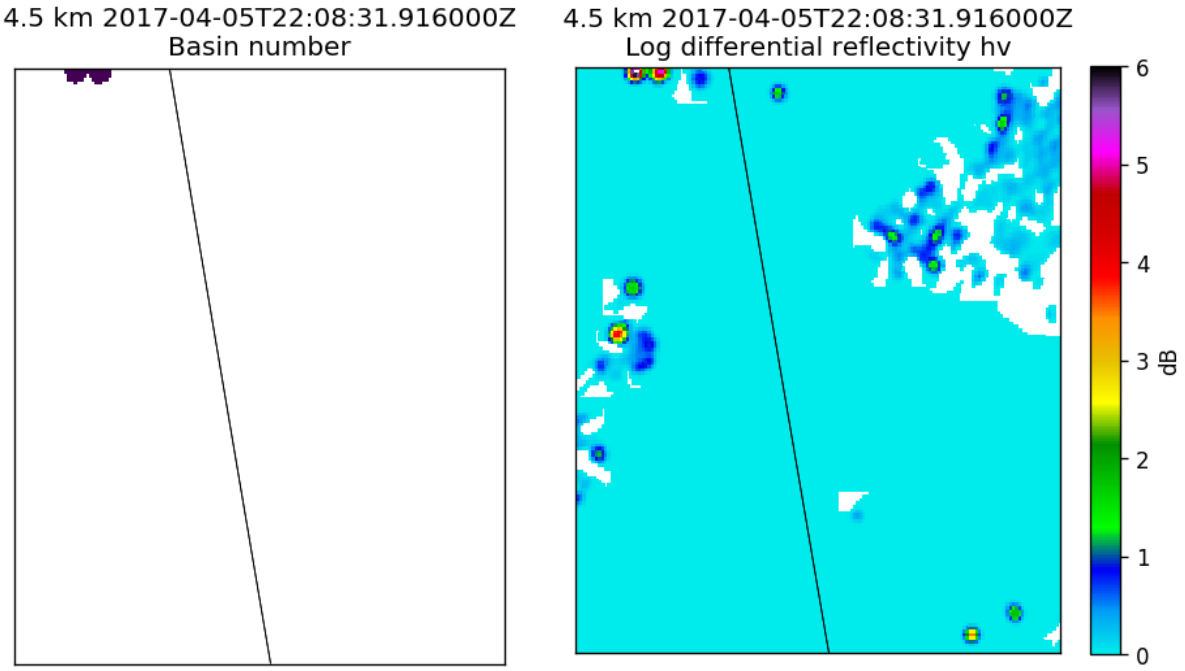

Fig. 52. Displayed here are CAPPIs from KHTX between 2159—2208 UTC 05 April 2017 of the Z_{DR} column objects identified by the EWA in the first column of images and smoothed Z_{DR} in the second column. The Z_{DR} column objects have the same parameters as IOP3b except a=1 dB.

Table 11. As in table 7 for KHTX observations on 05 April 2017.

Z_{DR} Columns	489
Tracks	89
Average Number of Z_{DR} Columns per Track	5.5
Average Duration (s)	1128
Average Duration (min)	18.8

6. CONCLUSIONS AND FUTURE DIRECTIONS

In this study, we applied the EWA and LSA to high spatiotemporal resolution UMass X-Pol Z_{DR} observations. The main goal of this research was to show the ZDR columns can be objectively identified and tracked while also gaining valuable information from these tracks. We also demonstrated how parameters for the algorithm could be judiciously chosen within a forecast verification framework. The key takeaway points are:

1. Z_{DR} columns can be objectively identified with the EWA in a manner consistent with human identification.
2. Z_{DR} columns can be tracked in time with the LSA, allowing time series of Z_{DR} column characteristics, including height above 0 °C level, areal extent, and peak Z_{DR} value, to be generated
3. Z_{DR} columns exhibit great variability in the above characteristics, with some trends corresponding to changes in storm mode.
4. Judicious choices of he algorithm parameters in the EWA (a, b, δ, and saliency) and the LSA (search radius), lead to robust, human-like identification and tracking of Z_{DR} column objects.
5. Stronger storms are generally associated with longer-lived Z_{DR} columns, while weaker ones are associated with shorter-lived Z_{DR} columns.
6. High spatiotemporal resolution polarimetric radar observations of Z_{DR} columns, such as those provided by UMass X-Pol, allows for improved identification and tracking of Z_{DR} columns relative to those contemporaneous observations from a WSR-88D.

It is important to obtain higher resolution data of Z_{DR} columns to not only provide the best opportunity at obtaining high quality Z_{DR} column tracks but to observe the high temporal evolution of Z_{DR} column. Due to their association with updrafts in convective storms, it's likely that there are small temporal evolutions that are not being observed by WSR-88Ds.

The applications of the EWA and the LSA provided in this study only touch on what can be done to evaluate Z_{DR} columns. Only a general overview of the tracks from each IOP are given in this research but a more in-depth analysis could be done, especially on individual Z_{DR} column tracks to show specific trends or correlations between Z_{DR} column characteristics. There were many other radars out in the field during VORTEX-SE. These other radars can be used to subsidize this study and mitigate limitations such as the cone of silence. Observations were also obtained by other mobile polarimetric radars during VORTEX-SE, so multi-Doppler analysis could be done to retrieve vertical velocity and be used to evaluate the correlation between retrieved updraft speed and characteristics of the associated Z_{DR} column.

Additionally, more high-quality observations of Z_{DR} columns should be obtained, specifically rapid observations on the order of one minute or less, with a focus on the midlevels (3—8 km), where Z_{DR} columns typically exist. Observations of Z_{DR} columns by UMass X-Pol show that the Z_{DR} columns can evolve on time scales much shorter than the currently used WSR-88D volume coverage patterns resolve. When studying the evolution of Z_{DR} columns, volume coverage patterns should include dense elevation scans in the midlevels to observe Z_{DR} columns at a high vertical and temporal resolution.

REFERENCES

Air Weather Service, AWS/TR-79/006, *The Use of the Skew T, Log P Diagram in Analysis and Forecasting*, Dec. 1979, revised March 1990, 159 pp, www.dtic.mil/cgi-bin/GetTRDoc?AD=ADA221842&Location=U2&doc=GetTRDoc.pdf.

Ashley, W. S., 2007: Spatial and temporal analysis of tornado fatalities in the united states: 1880-2005. *Wea. Forecasting*, **22**, 1214-1228, doi:10.1175/2007WAF2007004.1.

Auer, Jr. A. H. and W. Sand, 1966: Updraft measurements beneath the base of cumulus and cumulonimbus clouds. *J. Appl. Meteor.*, **5**, 461-466, doi:10.1175/1520-0450(1966)005<0461:UMBTBO>2.0.CO;2.

Aydin, K., and T. A. Seliga, and V. Bulaji, 1986: Remote Sensing of hail with a dual linear polarized radar. *J. Climate Appl. Meteor.*, **25**, 1475-1484, doi:10.1175/1520-0450(1986)025<1475:RSOHWA>2.0.CO;2.

— —, — —, and Y. Zhao, 1990: A differential reflectivity radar hail measurement technique: Observations during the Denver hailstorm of 13 June 1984. *J. Atmos. Oceanic Technol.*, **7**, 104-113, doi:10.1175/1520-0426(1990)007<0104:ADRRHM>2.0.CO;2.

Balakrishnan, N. and D. S. Zrnić, 1990: Use of polarization to characterize precipitation and discriminate large hail. *J. Atmos. Sci.*, **47**, 1525-1540, doi:10.1175/1520-0469(1990)047<1525:UOPTCP>2.0.CO;2.

Battan, L. J. and J. B. Theiss, 1966: Observations of vertical motions and particle sizes in a thunderstorm. *J. Atmos. Sci.*, **23**, 78-87, doi:10.1175/1520-0469(1966)023<0078:OOVMAP>2.0.CO;2.

Bechini, R., L. Baldini, R. Cremonini, and E. Gorgucci, 2008: Differential reflectivity calibration for operational radars. *J. Atmos. Oceanic Technol.*, **25**, 1542-1555, doi:10.1175/2008JTECHA1037.1.

Bluestein, H. B., M. M. French, R. L. Tanamachi, S. Frasier, K. Hardwick, F. Junyent, and A. Pazmany, 2007: Close-range observations of tornadoes in supercells made with dual-polarization, x-band, mobile doppler radar. *Mon. Wea. Rev.*, **135**, 1522-1543, doi:10.1175/MWR3349.1.

Bigg, E. K., 1953: The formation of atmospheric ice crystals by the freezing of droplets. *Q. J. R. Meteor. Soc.*, **79**, 510-519, doi:10.1002/qj.49707934207.

Brandes, E. A., 1976: Flow in severe thunderstorms observed by dual-doppler radar. *Mon. Wea. Rev.*, **105**, 113-120, doi: 10.1175/1520-0493(1977)105<0113:FISTOB>2.0.CO;2.

— —, J. Vivekanandan, J. D. Tuttle, and C. J. Kessinger, 1995: A study of thunderstorm microphysics with multiparameter radar and aircraft observations. *Mon. Wea. Rev.*, **123**, 3129-3143, doi:10.1175/1520-0493(1995)123<3129:ASOTMW>2.0.CO;2.

Bringi, B. N. and V. Chandrasekar, 2001: *Polarimetric Doppler Weather Radar*. Cambridge University Press, 672 pp.

— —, — —, L. Liu, P. C. Kennedy, V. Chandrasekar, and S. A. Rutledge, 1996: Dual multiparameter radar observations of intense convective storms: The 24 June 1992 case study. *Meteor. Atmos. Phys.*, **59**, 3-31.

— —, J. Vivekanandan, and J. D. Tuttle, 1986: Multiparameter radar measurements in Colorado convective storms. Part II: Hail detection studies. *J. Atmos. Sci.*, **43**, 2564-2577, doi:10.1175/1520-0469(1986)043<2564:MRMICC>2.0.CO;2.

— —, D. Burrow, and S. Menon, 1991: Multiparameter radar and aircraft study of raindrop spectral evolution in warm-based clouds. *J. Appl. Meteor*., **30**, 853-880, doi:10.1175/1520-0450(1991)030<0853:MRAASO>2.0.CO;2.

— —, K. Knupp, A. Detwiler, L. Liu, I. J. Caylor, and R. A. Black, 1997: Evolution of Florida thunderstorm during the convection and precipitation/electrification experiment: The case of 9 August 1991. *Mon. Wea. Rev.*, **125**, 2131-2160, doi:10.1175/1520-0493(1997)125<2131:EOAFTD>2.0.CO;2.

Brown, J. M. and Coauthors, 2011: Improvement and testing of WRF physics options for applications to Rapid Refresh and High resolution Rapid Refresh. *Proc. 14th Conf. on Mesocale Process|15th Conf. on Aviation, Range, and Aerospace Meteorology*, Los Angelos, CA, Amer. Meteor. Soc., 5.5 [Available online at https://ams.confex.com/ams/14Meso15ARAM/webprogram/Paper191234.html.]

Browning, K. A. and R. J. Donaldson, 1963: Airflow and structure of a tornadic storm. *J. Atmos. Sci.*, **20**, 533-545, doi:10.1175/ 1520-0469(1963)020,0533:AASOAT.2.0.CO;2.

Bunkers, M. J., B. A. Klimowski, J. W. Zeitler, R. L. Thompson, and M. L. Weisman, 2000: Predicting supercell motion using a new hodograph technique. *Wea. Forecasting*, **15**, 61-70, doi:10.1175/1520-0434(2000)015<0061:PSMUAN>2.0.CO;2.

Carlin, J. T., J. Gao, J. Snyder, and A. Ryzhkov, 2017: Assimilation of ZDR Columns for improving the spin-up and forecast of convective storms in storm-scale models: Proof-of-concept experiments. *Mon. Wea. Rev.*, **145**, 5033-5057, doi:10.1175/MWR-D-17-0103.1.

Caylor, I. and A. Illingworth, 1987: Radar observations and modelling of warm rain initiation. *Quart. J. Roy. Meteor. Soc.*, **113**, 1171-1191, doi:10.1002/qj.49711347806.

Conway, J. W. and D. S. Zrnić, 1993: A study of embryo production and hail growth using dual-Doppler and multiparameter radars. *Mon. Wea. Rev.*, **121**, 2511-2528, doi:10.1175/1520-0493(1993)121<2511:ASOEPA>2.0.CO;2.

Chisholm, A. J., 1973: Radar case studies and airflow models. *Alberta Hailstorms*, Part 1, *Meteor. Monogr.* 36, AMS, Boston, pp. 1-36

Davies-Jones, R. P., 1974: Discussion of measurements inside high-speed thunderstorm updrafts. *J. Appl Meteor.*, **13**, 710-717, doi: 10.1175/1520-0450(1974)013<0710:DOMIHS>2.0.CO;2.

Dixon, M. and G. Wiener, 1993: TITAN: Thunderstorm identification, tracking, analysis, and nowcasting—A radar-based methodology. *J. Atmos. Ocean. Technol.*, **10**, 785-797, doi:10.1175/1520-0426(1993)010<0785:TTITAA>2.0.CO;2.

Donovan, M. F. and E. R. Williams, 2008: The identification and verification of hazardous convective cells over oceans using visible and infrared satellite observations. *J. Appl. Meteor. Climate*, **47**, 164-184, doi:10.1175/2007JAMC1471.1.

Doviak, R. J. and D. S. Zrnić, 2006: *Doppler Radar and Weather Observations*. Dover Publications, 562 pp.

Frasier, S., W. Heberling, J. Waldinger, R. L. Tanamachi, and D. T. Dawson 2017. UMass X-Pol Radar Data in DORADE format. Version 1.0. UCAR/NCAR - Earth Observing Laboratory. https://data.eol.ucar.edu/dataset/527.028. Accessed 19 Mar 2018.

— —, — —, — —, — —, and — —, 2018: UMass X-Pol Radar Data. Version 1.0. doi:10.5065/d65b017g. Accessed 19 Mar 2018.

Fukao, S. and K. Hamazu, 2014: *Radar for Meteorological and Atmospheric Observations*. Springer, 537 pp.

Gorgucci, E., G. Scarchilli, and V. Chandrasekar, 1999: A Procedure to calibrate multiparameter weather radar using properties of the rain medium. *IEEE Trans. Geosci. Remote Sensing*, **37**, 269–276.

Hall, M. J., S. M. Cherry, J. W. F. Goddard, and G. R. Kennedy, 1980: Rain drop sizes and rainfall rate measured by dual-polarization radar. *Nat.*, **285**, 195-198, doi:10.1038/285195a0.

— —, and G. S. Cherry, 1984: Identification of hydrometeors and other targets by dual-polarization radar. *Radio Sci.*, **19**, 132-140, doi:10.1029/RS019i001p00132.

Hans, L., S. Fu, L. Zhao, Y. Zheng, H. Wang, and Y. Lin, 2009: 3D convective storm identification, tracking, and forecasting—An enhanced TITAN algorithm. *J. Atmos. Ocean. Technol.*, **26**, 719-732, doi:10.1175/2008JTECHA1084.1.

Helmus J. J. and S. M. Collis, 2016: The python ARM radar toolkit (Py-ART), a library for working with weather radar data in the python programming language. *J. Open Research Software*, **4**, e25, doi:10.5334/jors.119.

Herzegh, P. H. and R. A. Jameson, 1992: Observing precipitation through dual polarization radar measurements. *Bull. Amer. Meteor. Soc.*, **73**, 1365-1374, doi:10.1175/1520-0477(1992)073<1365:OPTDPR>2.0.CO;2.

Höller, H., M. Hagen, P. F. Meischner, V. N. Bringi, and J. Hubbert, 1994: Life cycle and precipitation formation in a hybrid-type hailstorm revealed by polarimetric and Doppler radar measurements. *J. Atmos. Sci.*, **51**, 2500-2522.

Homeyer, C. R. and M. R. Kumjian, 2015: Microphysical characteristics of overshooting convection from polarimetric radar observations. *J. Atmos. Sci.*, **72**, 870-891, doi:10.1175/JAS-D-13-0388.1.

Houser, J. L., H. B. Bluestein, and J. C. Snyder, 2015: Rapid-scan, polarimetric, doppler-radar observations of tornadogenesis and tornado dissipation in a tornadic supercell: the "El Reno, Oklahoma" storm of 24 May 2011. *Mon. Wea. Rev.*, **143**, 2685-2710, doi:10.1175/MWR-D-14-00253.1.

Hubbert, J., V. N. Bringi, L. D. Carey, and S. Bolen, 1998: CSU-CHILL polarimetric radar measurements from a severe hail storm in eastern Colorado. *J. App. Meteor.*, **37**, 749-775, doi:10.1175/1520-0450(1998)037<0749:CCPRMF>2.0.CO;2.

— — and — —, 2000: The effects of three-body scattering on differential reflectivity signatures. *J. Atmos. Ocean. Technol.*, **17**, 51-61, doi:10.1175/1520-0426(2000)017<0051:TEOTBS>2.0.CO;2.

Illingworth, A., J. Goddard, and S. Cherry, 1987: Polarization radar studies of precipitation development in convective storms. *Quart. J. Roy. Meteor. Soc.*, ***113***, 469-489, doi:10.1002/qj.49711347604.

Jameson, A. R. and E. A. Mueller, 1985: Estimation of propagation-differential phase shift from sequential orthogonal linear polarization radar measurements. *J. Atmos. Sci.*, **2**, 133-137, doi:10.1175/1520-0426(1985)002<0133:EOPDPS>2.0.CO;2.

— —, M. J. Murphy, and E. P. Krider, 1996: Multi-parameter radar observations of isolated Florida thunderstorms during the onset of electrification. *J. Appl. Meteor.*, **35**, 343-354, doi:10.1175/1520-0450(1996)035<0343:MPROOI>2.0.CO;2.

Johnson, D. A. and J. Hallett, 1968: Freezing and shattering of supercooled water drops. *Q. J. R. Meteor. Soc.*, **94**, 468-482, doi:10.1002/qj.49709440204.

Johnson, J. T., P. L. MacKeen, A. Witt, E. D. Mitchell, G. J. Stumpf, M. D. Eilts, and K. W. Thomas, 1998: The storm cell identification and tracking algorithm: An enhanced WSR-88D algorithm, *Wea. Forecasting*, **13**, 263-276, doi:10.1175/1520-0434(1998)013<0263:TSCIAT>2.0.CO;2.

Junyent, F., 2003: The design, development and initial field deployment of an X-band polarimetric Doppler weather radar. M.S. thesis, Electrical and Computer Engineering Dept., University of Massachusetts—Amherst, 120 pp.

Kabeche, F., J. Figueras i Ventura, B. Fradon, R. Hogan, A. A. Boumahmoud, A. Illingworth, and P. Tabary, 2010: Towards x-band polarimetric quantitative precipitation estimation in mountainous regions: The RHYTMME project. *Proc. Sixth Eur. Conf. Radar Meteor. Hydrol.*, Sibiu, Romania, ERAD, 6 pp.

Kennedy, P. C., S. A. Rutledge, W. A. Petersen, and V. N. Bringi, 2001: Polarimetric radar observations of hail formation. *J. Appl. Meteor.*, **40**, 1347-1366, doi:10.1175/1520-0450(2001)040<1347:PROOHF>2.0.CO;2.

Kosiba, K. and J. Wurman, 2013: Genesis of the Goshen County, Wyoming, tornado on 5 June 2009 during VORTEX2. *Mon. Wea. Rev.*, **141**, 1157-1181, doi:10.1175/MWR-D-12-00056.1.

Kumjian, M. R., 2013a: Principles and applications of dual-polarization weather radar. Part I: Description of the polarimetric radar variables. *J. Appl. Meteor.*, **1**, 226-242, doi:10.15191/nwajom.2013.0119.

— —, 2013b: Principles and applications of dual-polarization weather radar. Part II: Warm and cold season applications. *J. Appl. Meteor.*, **1**, 243-264, doi:10.15191/nwajom.2013.0119.

— —, 2013c: Principles and applications of dual-polarization weather radar. Part III: Artifacts. *J. Appl. Meteor.*, **1**, 265-274, doi:10.15191/nwajom.2013.0120.

— — and A. V. Ryzhkov, 2008: Polarimetric signatures in supercell thunderstorms, *J. Appl. Meteor. Climatol.*, **47**, 1940-1961, doi:10.1175/2007JAMC1874.1.

— —, — —, V. M. Melnikov, and T. J. Schuur, 2010: Rapid-scan super-resolution observations of a cyclic supercell with dual-polarization WSR-88D. *Mon. Wea. Rev.*, **138**, 3762-3786, doi:10.1175/2010MWR3322.1.

— —, — —, and S. M. Ganson, 2012: Freezing of raindrops in deep convective updrafts: A microphysical and polarimetric model. *J. Atmos. Sci.*, **69**, 3471-3490, doi:10.1175/jas-d-12-067.1.

— —, — —, A. P. Khain, N. Benmoshe, E. Ilotoviz, and V. T. J. Phillips, 2014: The anatomy and physics of ZDR columns: Investigating a polarimetric radar signature with a spectral bin microphysical model. *J. App. Meteor. Climatol.*, **53**, 1820-1843, doi:10.1175/JAMC-D-13-0354.1.

Lafleur A. and P. Saunders, cited 2018: Radar log. [Available online at http://catalog.eol.ucar.edu/vortex-se_2017/report/67/1220/187497/54504544]

Lakshmanan, V., 2000: Using a genetic algorithm to tune a bounded weak echo region detection algorithm. *J. Appl. Meteor.*, **39,** 222-230, doi:10.1175/1520-0450(2000)039<0222:uagatt>2.0.co;2.

— —, 2012: Identifying objects. *Automating the Analysis of Spatial Grids: A Practical Guide to Data Mining Geospatial Images for Human & Environmental Applications,* V. Lakshmanan, Ed., Geotechnologies and the Environment Series, Vol. 6, Springer, 173-221.

— — and T. Smith, 2009: Data mining storm attributes from spatial grids. *J. Atmos. Ocean. Technol.*, **26**, 2353-2365, doi:10.1175/2009JTECHA1257.1.

— — and — —, 2010: An objective method of evaluating and devising storm-tracking algorithms. *Wea. Forecasting*, **25**, 701-709, doi:10.1175/2009WAF2222330.1.

— —, K. Hondl, and R. Rabin, 2009: An efficient, general-purpose technique for identifying storm cells in geospatial images. *J. Atmos. Ocean. Technol.*, **26**, 523-537, doi:10.1175/2008JTECHA1153.1.

Laws, K., R. Morss, Y. Richardson, and E. Rasmussen, 2018: VORTEX-SE Science Plan, 68 pp.

Lemone, M. A. and E. J. Zipser, 1980: Cumulonimbus vertical velocity events in GATE. Part I: Diameter, intensity and mass flux. *J. Atmos. Sci.*, **37**, 2444-2456, doi:10.1175/1520-0469(1980)037<2444:CVVEIG>2.0.CO;2.

Loney, M. L., D. S. Zrnić, J. M. Straka, and A. V. Ryzhkov, 2002: Enhanced polarimetric radar signatures above the melting level in a supercell storm. *J. Appl. Meteor.*, **1**, 1179-1195.

Lyza, A. W. and K. R. Knupp, 2016: A detailed analysis of tornado events across northeastern Alabama's southern Cumberland system. *28th Conf. Severe Storms*. Portland, OR, Amer. Meteor. Soc., 7A.1, https://ams.confex.com/ams/28SLS/webprogram/Paper301625.html

Marshall, T. C., W. D. Rust, and M. Stolzenburg, 1995: Electrical structure and updraft speeds in thunderstorms over the southern Great Plains. *J. Geophys. Res.: Atmos*, **100**, 1001-1015, doi:10.1029/94JD02607.

Meischner, P. F., V. N. Bringi, D. Heimann, and H. Höller, 1991: A squall line in southern Germany: Kinematics and precipitation formation as deduced by advanced polarimetric and doppler radar measurements, *Mon. Wea. Rev.*, **119**, 678-701, doi:10.1175/1520-0493(1991)119<0678:ASLISG>2.0.CO;2.

Melnikov, V. M., D. S. Zrnić, R. M. Rabin, and P. Zhang, 2008: Radar polarimetric signatures of fire plumes in Oklahoma. *J. Geophys. Res. Lett.*, **35**, 1-5, doi:10.1029/2008GL034311.

McCormick, G. C. and A. Hendry, 1985: Optimal polarizations for partially polarized backscatter. *IEEE Trans. Antennas Propag.*, **AP-3**, 33-40, doi:10.1109/TAP.1985.1143463.

Payne, C. D., T. J. Schuur, D. R. MacGorman, M. I. Biggerstaff, K. M. Kuhlman, and W. D. Rust, 2010: Polarimetric and electrical characteristics of a lightning ring in a supercell storm. *Mon. Wea. Rev.*, **138**, 2405-2425, doi:10.1175/2009MWR3210.1.

Picca, J. C., A. V. Ryzhkov, and M. R. Kumjian, 2010: ZDR columns as a predictive tool for hail growth and storm evolution. *25th Conf. on Severe Local Storms*, Denver, CO, Amer. Meteor. Soc., 11.3 [Available online at https://ams.confex.com/ams/25SLS/webprogram/Paper175750.html]

— — and — —, 2012: A dual-wavelength polarimetric analysis of the 16 May 2010 Oklahoma City extreme hailstorm. *Mon. Wea. Rev.*, **140**, 1385-1403, doi:10.1175/MWR-D-11-00112.1.

Pruppacher, H. R. and K. V. Beard, 1970: A wind tunnel investigation of the internal circulation and shape of water drops falling at terminal velocity in air. *Q. J. R. Meteor. Soc.*, **96**, 247-256, doi:10.1002/qj.49709640807.

Rasmussen, R. M., V. Lev, V. Levizzani, and H. R. Pruppacher, 1984: A wind tunnel and theoretical study on the melting behavior of atmospheric ice particles: III. Experiment and theory for spherical ice particles of raidus > 500 μm. *J. Atmos. Sci.*, **41**, 381-388, doi:10.1175/1520-0469(1984)041<0381:AWTATS>2.0.CO;2.

— — and A. J. Heymsfield, 1987: Melting and shedding of graupel and hail. Part I: Model physics. *J. Atmos. Sci*., **44**, 2754–2763.

Rasmussen, E. N., J. M. Straka, R. Davies-Jones, C. A. Doswell III, F. H. Carr, M. D. Eilts, D. R. MacGorman, 1994: Verification of the origins of rotation in tornadoes experiment: VORTEX. *Bull. Amer. Meteor. Soc.*, **75**, 995-1006, doi:10.1175/1520-0477(1994)075<0995:Votoor>2.0.Co;2.

— — and Coauthors, 2015: VORTEX-Southeast Program Overview, 36 pp, [Available online at https://www.nssl.noaa.gov/temp/vortexsefunding/ProjectOverview.pdf]

Rinehart, R. E., 2001: *Radar for Meteorologists*. Rinehart Publications, 428 pp.

Romine, G. S., D. W. Burgess, and R. B. Wilhelmson, 2008: A dual-polarization-radar-based assessment of the 8 May 2003 Oklahoma City area tornadic supercell. *Mon. Wea. Rev.*, **136**, 2849-2870, doi:10.1175/2008MWR2330.1.

Rosenfield, D., W. L. Woodley, A. Lerner, G. Kelman, and D. T. Lindsey, 2008: Satellite detection of severe convective storms by their retrieved vertical profiles of cloud particle effective radius and thermodynamic phase. *J. Geophys. Res.*, **113**, D04208, doi:10.1029/2007JD008600.

Rowe, A. K., S. A. Rutledge, and T. J. Lang, 2012: Investigation of microphysical processes occurring in organized convection during NAME. *Mon. Wea. Rev.*, **140**, 2168-2187, doi:10.1175/MWR-D-11-00124.1.

Ryzhkov, A. V., V. B. Zhuravlyov, and N. A. Rybakova, 1994: Preliminary results of x-band polarization studies of clouds and precipitation. *J. Atmos. Oceanic Technol.*, **11**, 132-139, doi:10.1175/1520-0426(1994)011<0132:PROXBP>2.0.CO;2.

— —, D. S. Zrnić, T. J. Schuur, and D. W. Burgess, 2005: Polarimetric tornado detection, *J. Appl. Meteor.*, **44**, 557-570, doi:10.1175/JAM2235.1.

— — and — —, 2007: Depolarization in ice crystals and its effect on radar polarimetric measurements. *J. Atmos. Ocean. Technol.*, **24**, 1256-1267, doi:10.1175/JTECH2034.1.

Sachidananda, M. and D. S. Zrnić, 1985: ZDR measurement considerations for a fast scan capability radar. *Radio Sci.*, **20**, 907–922, doi:10.1029/RS020i004p00907.

Saunders, P. and A. Lafleur, cited 2018: Radar log. [Available online at http://catalog.eol.ucar.edu/vortex-se_2017/report/67/1220/187497/54184070.]

Seedorf, M. and W. Heberling, cited 2018: Radar log. [Available online at http://catalog.eol.ucar.edu/vortex-se_2016/report/67/1220/183830/51473432.]

Scharfenberg, K. A. and Coauthors, 2005a: The joint polarization experiment: Polarimetric radar in forecasting and warning decision making. *Wea. Forecasting*, **20**, 775-788, doi:10.1175/WAF881.1.

— —, K. L. Elmore, E. Forren, V. Melnikov, and D. S. Zrnić, 2005b: Estimating the impact of a 3-dB sensitivity loss on WSR-88D data. *11th Conf. Mesoscale Processes 32nd Conf. Radar Meteor.*

Seliga, T. and V. Bringi, 1976: Potential use of radar differential reflectivity measurements at orthogonal polarizations for measuring precipitation. *J. Appl. Meteor.*, **15**, 69-76, doi:10.1175/1520-0450(1976)015<0069:PUORDR>2.0.CO;2.

Smith, P. L., D. J. Musil, A. G. Detwiler, and R. Ramachandran, 1999: Observations of mixed-phase precipitation within a CAPE thunderstorm. *J. Appl. Meteor.*, **38**, 145-155, doi:10.1175/1520-0450(1999)038<0145:OOMPPW>2.0.CO;2.

Smith, A. B. and R. W. Katz, 2013: US billion-dollar weather and climate disasters: Data sources, trends, accuracy and biases. *Natural Hazards*, **67**, 387-410, doi:10.1007/s11069-013-0566-5.

Snyder, J. C., H. B. Bluestein, S. J. Frasier, and G. Zhang, 2010: Attenuation correction and hydrometeor classification of high-resolution, X-band, dual-polarized mobile radar measurements in severe convective storms. *J. Atmos. Ocean. Technol.*, **27**, 1979-2001, doi:10.1175/2010JTECHA1356.1.

— —, — —, — —, and V. Venkatesh, 2013: Observations of polarimetric signatures in supercells by an x-band mobile doppler radar. *Mon. Wea. Rev.*, **141**, 3-29, doi:10.1175/MWR-D-12-00068.1.

— —, — —, D. T. Dawson II, and Y. Jung, 2017: Simulations of polarimetric, x-band radar signatures in supercells. Part II: ZDR columns and rings and KDP columns. *J. Appl. Meteor. Climatol.*, **56**, 2001-2026, doi:10.1175/JAMC-D-16-0139.1.

— —, A. V. Ryzhkov, M. R. Kumjian, A. P. Khain, and J. C. Picca, 2015: A ZDR column detection algorithm to examine convective storm updrafts. *Wea. Forecasting*, **30**, 1819-1844, doi:10.1175/WAF-D-15-0068.1.

Starzec, M., C. Homeyer, and G. Mullendore, 2017: Storm labeling in three dimensions (SL3D): A volumetric radar echo and dual-polarization updraft classification algorithm. *Mon. Wea. Rev.*, **145**, 1127-1145, doi:10.1175/MWR-D-16-0089.1.

Stith, J. L., J. E. Dye, A. Bansemer, A. J. Heymsfield, C. A. Grainger, W. A. Petersen, R. Cifelli, 2001: Microphysical observations of tropical clouds. *J. Appl. Meteor.*, **41**, 97-117, doi: 10.1175/1520-0450(2002)041<0097:MOOTC>2.0.CO;2.

Storm Prediction Center, 2018: Severe weather climatology (1982-2011). Accessed 11 April 2018, http://www.spc.noaa.gov/new/SVRclimo/climo.php?parm=anySvr.

Tanamachi, R. L., H. B. Bluestein, J. B. Houser, S. J. Frasier, and K. M. Hardwick, 2012: Mobile, x-band, polarimetric Doppler radar observations of the 4 May 2007 Greensburg, Kansas, tornadic supercell. *Mon. Wea. Rev.*, **140**, 2103-2125, doi:10.1175/MWR-D-11-00142.1.

— — and P. L. Heinselman, 2016: Rapid-scan, polarimetric observations of central Oklahoma severe storms on 31 May 2013. *Wea. Forecasting*, **31**, 19-42, doi:10.1175/WAF-D-15-0111.1.

— — and J. Waldinger, cited 2018: Radar log. [Available online at http://catalog.eol.ucar.edu/vortex-se_2016/report/67/1220/183830/51473435]

Tuttle, J., V. Bringi, H. Orville, and F. Kopp, 1989: Multiparameter radar study of a microburst: Comparison with model results. *J. Atmos. Sci.*, **46**, 601-620, doi:10.1175/1520-0469(1989)046<0601:MRSOAM>2.0.CO;2.

University of Wyoming College of Engineering, 2018: Sounding station parameters and indices, Accessed 17 April 2018, http://weather.uwyo.edu/upperair/indices.html.

Van Den Broeke, M. S., 2016: Polarimetric variability of classic supercell storms as a function of environment, *J. Appl. Meteor. Climatol.*, **55**, 1907-1925, doi:10.1175/JAMC-D-15-0346.1.

— —, 2017: Polarimetric radar metrics related to tornado life cycles and intensity in supercell storms. *Mon. Wea. Rev.*, **145**, 3671-3686, doi:10.1175/MWR-D-16-0453.1.

— — and C. A. Van Den Broeke, 2015: Polarimetric radar observations from a waterspout-producing thunderstorm, *Wea. Forecasting*, **30**, 329-348, doi:10.1175/WAF-D-14-00114.1.

Wakimoto, R. M., and V. N. Bringi, 1988: Dual-polarization observations of microbursts associated with intense convection: The 20 July storm during the MIST project. *Mon. Wea. Rev.*, **116**, 1521-1539.

Whiton, R. C., P. L. Smith, S. G. Bigler, K. E. Wilk, and A. C. Harbuck, 1998: History of operational use of weather radar by U.S. weather services. Part I: The pre-NEXRAD era. *Wea. Forecasting*, **13**, 219-243, doi:10.1175/1520-0434(1998)013<0219:HOOUOW>2.0.CO;2.

Wurman, J., D. Dowell, Y. Richardson, P. Markowski, E. Rasmussen, D. Burgess, L. Wicker, H. B. Bluestein, 2012: The second verification of the origins of rotation in tornadoes experiment VORTEX2. *Bull. Amer. Meteor. Soc.*, **93**, 1147-1170, doi:10.1175/BAMS-D-11-00010.1.

Zrnić, D. S., 1987: Three-body scattering produces precipitating signature of special diagnostic value, *Radio Sci*., **22**, 76-86. doi:10.1029/RS022i001p00076.

— — and A. V. Ryzhkov, 1998: Observations of insects and birds with a polarimetric radar. *IEEE Trans. Geosci. Electron.*, **36**, 661-668, doi:10.1109/36.662746.

— — and — —, 2004: Polarimetric properties of chaff. *J. Atmos. Oceanic Technol.*, **21**, 1017-1024, doi:10.1175/1520-0426(2004)021<1017:PPOC>2.0.CO;2.